Max-Planck-Institut für Polymerforschung

Max Planck Institute for Polymer Research

Self-Assembled Nanocarriers Based on Amphiphilic Ruthenium Complexes for Anticancer Phototherapy

Dissertation

Zur Erlangung des Grades

„Doktor der Naturwissenschaften“

im Promotionsfach Chemie

Eingereicht am

Fachbereich Chemie, Pharmazie und Geowissenschaften

der Johannes Gutenberg-Universität Mainz

Von

Xiaolong Zeng

Mainz, 2021

Die vorliegende Arbeit wurde im Zeitraum von März 2017 bis Juli 2021 am Max-Planck-Institut für Polymerforschung in Mainz im Arbeitskreis von Prof. Dr. Hans-Jürgen Butt und Prof. Dr. Si Wu angefertigt.

Dekan:

Prodekan:

Gutachter 1:

Gutachter 2:

Date of oral examination:

Table of Contents

Abstract 1

Zusammenfassung 3

Motivation 5

Chapter 1: Introduction 6

1.1 Nanocarriers to overcome drug resistance in anticancer therapy 6

1.1.1 Mechanisms of drug resistance in cancer treatment 6

1.1.2 Strategies for reversing drug resistance 8

1.1.3 Nanocarriers to overcome drug resistance 9

1.2 Nanocarriers with favorable properties to enhance delivery efficiency 10

1.2.1 Five-step delivery cascade of nanocarriers 10

1.2.2 Physicochemical properties of nanocarriers 13

1.3 Nanocarriers based on ruthenium complexes for anticancer treatment 14

1.3.1 Ru complexes in cancer therapy 14

1.3.2 Nanocarriers based on Ru complexes for cancer therapy 23

1.3.3 Challenges of nanocarriers based on Ru complexes in cancer therapy 28

1.4 References 29

Chapter 2: Red-light-induced simultaneous dePEGylation, morphology transition, and zeta potential increase using amphiphilic metallodrug assemblies: improved tumor penetration and cellular internalization for efficient anticancer phototherapy 38

2.1 Statement of contribution 39

2.2 Introduction 40

2.3 Results and discussion 43
2.3.1 Synthesis of Ru-PEG 43
2.3.2 Self-assembly of Ru-PEG 44
2.3.3 Light-cleavable Ru-PEG and transformable properties 44
2.3.4 Cellular uptake and in vitro cytotoxicity assessment 47
2.3.5 Tumor penetration ability of Ru-PEG 50
2.3.6 In vivo anticancer assessment 51
2.4 Conclusions 53
2.5 References 54
2.6 Supporting information 57
Chapter 3: Fighting against drug-resistant tumors using a dual-responsive Pt(IV)/Ru(II) bimetallic polymer 88
3.1 Statement of contribution 89
3.2 Introduction 90
3.3 Result and discussion 93
3.3.1 Synthesis of PolyPt/Ru 93
3.3.2 Self-assembly of PolyPt/Ru 94
3.3.3 Dual-responsiveness of PolyPt/Ru 94
3.3.4 In vitro cytotoxicity against drug resistant cancer cells 98
3.3.5 Cellular uptake and in vitro cytotoxicity assessment 100
3.3.6 In vivo anticancer assessment 102
3.4 Conclusions 106

3.5 References 107

3.6 Supporting Information 110

Chapter 4: Summary and Outlook 148

4.1 Summary 148

4.2 Outlook 149

Publications 150

Acknowledgment 151

Abstract

Photoresponsive ruthenium (Ru) complexes have promising anticancer properties. Self-assembled nanocarriers have been used to deliver Ru complexes for anticancer phototherapy. Comparing with small molecule, nanocarriers based on Ru complexes exhibit improved bioavailability and extended blood circulation. However, conventional self-assembled nanocarriers suffer low delivery efficiency and lack of combined therapy. The inefficient nanocarriers limit their anticancer efficacy due to the low Ru concentration at target sites. Single therapy suffer limitations to combat tumor complexity. A major goal in this field is to develop nanocarriers with high delivery efficiency, and further overcome the complexity of tumor, such as drug resistance. In this thesis, we reported novel nanocarriers based on photoresponsive Ru complexes to address these issues.

In Chapter 2, we designed a light-cleavable Ru nanocarriers (Ru-PEG) with tunable properties to enhance the delivery efficiency. Ru-PEG consist a hydrophobic Ru moiety and a hydrophilic PEG moiety. Ru-PEG assembled into vesicles. Light irradiation of Ru-PEG induces the morphological transformation, changing from vesicles to large compound micelles (LCMs). Light irradiation also caused the release of PEG, leading to the increment of surface charge of Ru nanocarriers. The formed LCMs had a smaller diameter, which improved the penetration depth at tumor sites. The increased positive charged Ru nanocarriers enabled efficient internalization. Both of them improved the delivery efficiency of Ru complexes.

In chapter 3, we reported a dual-responsive Ru-containing nanocarriers (PolyPt/Ru) to reverse drug resistance. PolyPt/Ru is a triblock polymer with two hydrophilic PEG moieties and one hydrophobic Pt/Ru bimetallic moiety. PolyPt/Ru self-assembled into

nanoparticles. Irradiation of PolyPt/Ru with red light generated $^1O_2$, induced nanocarrier degradation, and triggered the release of Ru(II) anticancer agents. The anticancer drug, cisplatin, was released in the intracellular environment via the reduction of Pt(IV) moieties. The released Ru(II) anticancer agent, cisplatin, and the generated $^1O_2$ have different anticancer mechanisms. Their synergistic effects inhibited the growth of resistant tumors.

Zusammenfassung

Photoresponsive Ruthenium (Ru)-Komplexe haben vielversprechende anticancerogene Eigenschaften. Selbstorganisierte Nanoträger wurden verwendet, um Ru-Komplexe für die Phototherapie gegen Krebs herzustellen. Im Vergleich zu kleinen Molekülen weisen Nanoträger auf Basis von Ru-Komplexen eine verbesserte Bioverfügbarkeit und Zirkulation im Blutkreislauf auf. Herkömmliche selbstorganisierte Nanoträger leiden jedoch unter einer geringen Abgabeeffizienz und einem Mangel an kombinierter Therapie. Die ineffizienten Nanoträger haben eine begrenzte anticancerogene Wirkung aufgrund der geringen Ru-Konzentration am Wirkort. Die Einzeltherapie leidet unter Einschränkungen bei der Bekämpfung der Tumorkomplexität. Ein Hauptziel auf diesem Gebiet ist die Entwicklung von Nanoträgern mit hoher Abgabeeffizienz und die weitere Überwindung der Komplexität von Tumoren, wie z. B. der Arzneimittelresistenz. In dieser Arbeit berichteten wir über neuartige Nanoträger, die auf photoresponsiven Ru-Komplexen basieren, um diese Probleme anzugehen.

In Kapitel 2 haben wir einen lichtspaltbaren Ru-Nanoträger (Ru-PEG) mit einstellbaren Eigenschaften entwickelt, um die Abgabeeffizienz zu verbessern. Ru-PEG besteht aus einer hydrophoben Ru-Einheit und einer hydrophilen PEG-Einheit. Ru-PEG organisiert sich selbst zu Vesikeln. Die Bestrahlung von Ru-PEG mit Licht induziert die morphologische Transformation von Vesikeln zu großen zusammengesetzten Mizellen (LCMs). Gleichzeitig wird PEG freigesetzt, was zu einer Erhöhung der Oberflächenladung der Ru-Nanoträger führt. Die gebildeten LCMs hatten einen kleineren Durchmesser, was zu einer erhöhten Eindringtiefe in die Tumore führte. Die stärker positiv geladenen Ru-Nanoträger ermöglichten eine effiziente Internalisierung. Beides führte zu einer verbesserten Abgabeeffizienz von Ru-Komplexen.

In Kapitel 3 berichteten wir über einen doppelt ansprechenden Ru-haltigen Nanoträger (PolyPt/Ru), der Arzneimittelresistenzen umgeht. PolyPt/Ru ist ein Triblockpolymer mit zwei hydrophilen PEG-Einheiten und einer hydrophoben Pt/Ru-Bimetalleinheit und organisiert sich selbst zu Nanopartikeln. Die Bestrahlung von PolyPt / Ru mit rotem Licht erzeugte $^1O_2$, induzierte den Abbau von Nanoträgern und löste die Freisetzung von Ru(II) –Zytostatika aus. Das Zytostatikum Cisplatin wurde in der intrazellulären Umgebung über die Reduktion von Pt(IV)-Einheiten freigesetzt. Das freigesetzte Ru(II) - Zytostatikum Cisplatin und das erzeugte $^1O_2$ weisen unterschiedliche anticancerogene Mechanismen auf. Ihre synergistischen Wirkungen hemmten das Wachstum resistenter Tumoren.

Motivation

Self-assembled nanocarriers have been applied to deliver Ru complexes towards cancer cells in cancer therapy. To date, several strategies have been developed to optimize the delivery efficiency. For example, PEGylated nanocarriers are used to prolong blood circulation. Charged nanocarriers enable efficient internalization by cancer cells. However, these strategies suffer antagonistic effects. In general, PEGylation is negatively related to cellular internalization. Positive charged nanocarriers absorb proteins during circulation, which lead to be cleared by macrophage. Nanocarriers with tunable properties may address these problems.

However, such smart nanocarriers based on Ru complexes do not exist. To achieve this goal, I made use of a light-cleavable Ru complex to construct nanocarriers with tunable properties. I expect the PEGylated Ru-containing nanocarriers can reduce specific protein absorption during circulation. After accumulating at tumor sites and reaching cancer cells, I expect that light-induced the release of PEG can improve cellular internalization. I wish the adjustable nanocarriers based on light-cleavable Ru complexes can achieve high delivery efficiency.

Another issue for nanocarriers based on Ru complexes is to reverse the drug resistance of tumor. Most chemotherapeutic drugs become insensitive to cancer cells after using for several times. Using anticancer drugs with different mechanisms of action may solve this problem. To achieve this goal, I developed a dual-responsive bimetallic polymer, which contained Ru anticancer agents and cisplatin anticancer drugs. The photoresponsive Ru complexes and cisplatin had different anticancer mechanisms. I expect the combination of Ru complexes and cisplatin can reverse drug resistance.

Chapter 1: Introduction

1.1 Nanocarriers to overcome drug resistance in anticancer therapy

1.1.1 Mechanisms of drug resistance in cancer treatment

Cancer is a major burden of death over the world. Cancer is responsible for nearly 10 million deaths every year.[1] About one in six deaths accounts for cancer globally.[2] Typically, cancer treatment involves surgery, radiotherapy and chemotherapy.[3] Chemotherapy has been most widely applied for cancer treatment.[4] However, cancer patients may be resistant to anticancer drugs after receiving chemotherapy several times.[4] Drug resistance results in therapeutic failure and eventually cause patients death.

The mechanism of drug resistance falls into several categories (Figure 1).[5] Firstly, the decrement of cellular uptake causes drug resistance.[6, 7] The cellular uptake of anticancer drugs influences the therapeutic performance of chemotherapy.[6] Cancer cells take up drugs either via receptors/transporter, endocytosis or diffusion across the plasma membrane.[8] However, the alteration or mutation of receptors/transporter in resistant cancer cells reduces the cellular uptake efficiency, thus decreasing the intracellular drug concentrations.[9] This results in cancer cells insensitivity to drugs. The reduced uptake of toxic drugs is the most major causes of drug resistance.

Secondly, the active drug efflux causes drug resistance.[10, 11] The efflux pump, such as P-gp protein, which is overexpressed on the membrane of resistant cancer cells.[10, 12] They can not only inhibit the drug uptake but also pump drugs out of cells.[12] Drug efflux decreases intracellular drug concentration. The up-regulated overexpression of P-gp proteins results in a significant resistance to chemotherapy.

Thirdly, the enhanced DNA repair capacity causes drug resistance.[13, 14] Many anticancer drugs cause damage to DNA.[15] This is responsible for the cytotoxicity of

these drugs. Resistant cancer cells repair DNA when it becomes damaged. When the magnitude of damage is reduced, DNA repair confers resistance to anticancer drugs.

The other mechanism of drug resistance is due to the inactivation of drugs.[16] Some intracellular biomolecules strongly bind and sequester the specific drugs.[17] For example, glutathione (GSH) has been implicated in resistance to several drugs, including platinum-containing compounds,[16] and alkylating agents such as melphalan.[18] Similarly, cytochrome P450 enzymes causes the inactivation of anticancer drug, irinotecan.[19] These biomolecules are prior binding to drugs, decrease their toxicities to cancer cells, and cause drug resistance. Moreover, when administered intravenously, various proteins in blood may also bind to anticancer drugs, leading to the inactivation.[9]

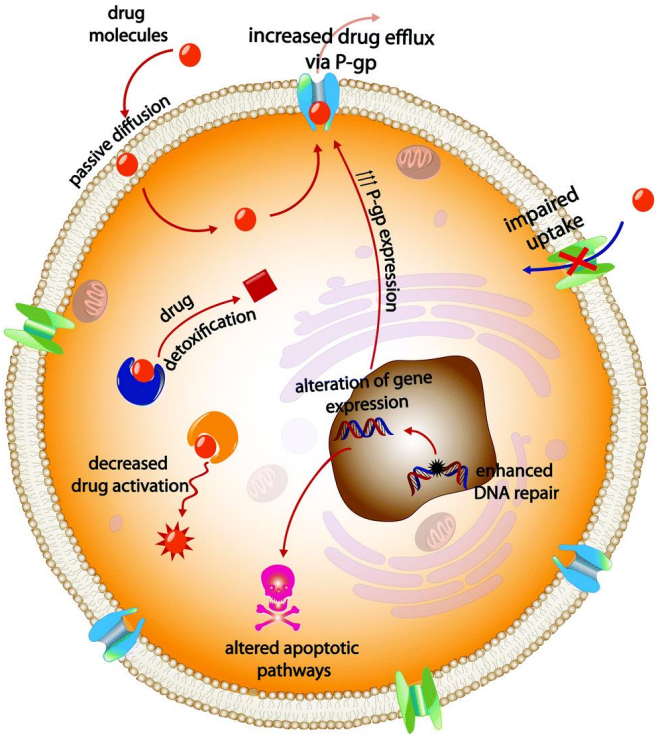

Figure 1. Schematic illustration of nanocarriers to overcome drug resistance. Adapted with permission from ref 5. Copyright 2016 Royal Society of Chemistry.

1.1.2 Strategies for reversing drug resistance

Several strategies have been proposed to combat drug resistance in cancer treatment.[4, 20, 21] Modification of targeting molecules can overcome drug resistance that is caused by reduced cellular uptake.[22] Therefore, anticancer drugs are conjugated with specific molecules such as antibody or targeting peptides.[23] These molecules can specifically target the receptors which are overexpressed on the cell membrane. The biochemical reaction between targeting molecules and receptors activates specific signals, which further promote the internalization of drugs into cancer cells.[24] The enhanced internalization reverses drug resistance.

Synchronous administration of anticancer drugs along with protein inhibitors, such as P-gp protein inhibitors or DNA repair protein inhibitors, may reverse drug resistance.[25, 26] P-gp inhibitors possess greater affinity against P-gp proteins with high specificity.[27] This subsequently decreases the activity of P-gp proteins, leading to the inhibition of drug efflux, and thus achieving the reversal of drug resistance.

Depletion of intracellular GSH may modulate drug resistance caused by the inactivation of drugs.[28, 29] Some small molecules, such as buthionine sulfoximine (BSO), are applied to deplete GSH levels.[30] BSO can inhibit the gamma-glutamylcysteine synthetase, which involves the first step of GSH bio-synthesis, thus decreasing the intracellular GSH levels.[30] BSO can also increase the sensitivity of anticancer drugs to cancer cells,[31] as a result, drug resistance is reversed.

Although the above-mentioned strategies have been developed, it is challenging to overcome multiple resistant pathways. The current strategies still suffer limitations in clinic. For example, antibody may be rapidly degraded by enzyme or cleared from the bloodstream.[32] Administration of anticancer drugs and protein inhibitors is limited to their different circulation times. The different components may not reach the target sites

simultaneously, leading to non-ideal effect.[33] BSO always suffer from poor solubility in aqueous solution and poor selectivity towards tumor. Thus, reversing drug resistance still poses a challenge.

1.1.3 Nanocarriers to overcome drug resistance

Recently, nanotechnology has been developed to provide a promising alternative, compared to the conventional small-molecule chemotherapeutics. Nanotechnology circumvents drug resistance by encapsulating, attaching, and conjugating therapeutic biological agents to nanocarriers. Nanocarriers hold several advantages for reversing drug resistance in cancer treatment (Figure 2).[34]

Firstly, nanocarriers can deliver multiple therapeutic payloads in one system, such as P-gp inhibitors and anticancer drugs, acting as "all-in-one" strategy.[25] Different therapeutic agents that are encapsulated/conjugated into nanocarriers have the same pharmacokinetic profiles. Their similar bio-distribution exhibit the synergistics effect at the target sites.

Secondly, nanocarriers can be easily achieved surface modification.[35] Various functional molecules can be simultaneously attached onto the surface of nanocarriers. Modification by antibodies provides active targeting ability towards cancer cells.[36] Modification by poly (ethylene glycol) (PEG) achieves stealthy effect during circulation,[37] which prevent the inactivation of loaded cargoes from blood clearance and enzyme degradation.

Furthermore, the internalization category of nanocarriers is different with free drugs. Most free drugs enter into cancer cells by diffusion across membranes,[38] which is easily recognized by P-gp proteins that pumping drugs out from cancer cells. However, nanocarriers, such as gold nanoparticles or silica nanoparticles, effectively enter into

cancer cells through endocytosis, with bypass of drug efflux pumps.[39, 40] These advantages endow nanocarriers with the capacity to address complicated and combined mechanisms of drug resistance.

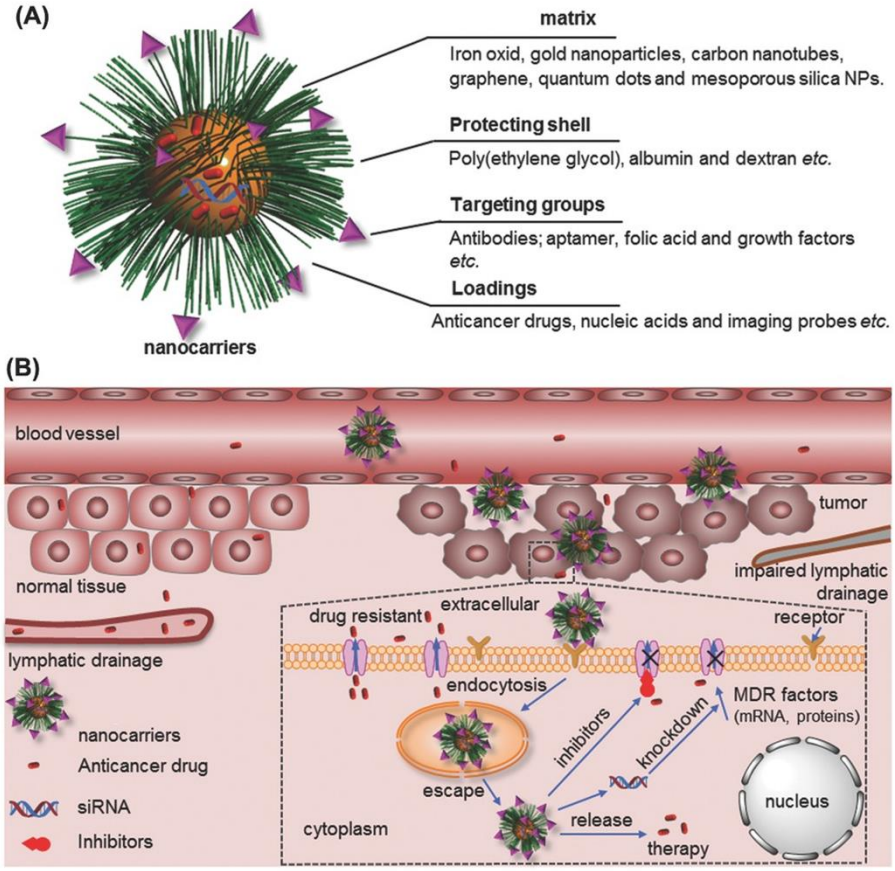

Figure 2. Schematic illustration of nanocarriers to overcome drug resistance. Adapted with permission from ref 34. Copyright 2016 WI LEY-VCH Verlag GmbH & Co. KGaA.

1.2 Nanocarriers with favorable properties to enhance delivery efficiency

1.2.1 Five-step delivery cascade of nanocarriers

The ultimate goal of nanocarriers is to deliver drugs into cancer cells as free molecules, to exert their pharmaceutical effects. Typically, intravenously administered nanocarriers go through a cascade of five steps: 1) circulation in blood; 2) accumulation at tumor sites; 3) penetration into deep tumor tissues; 4) internalization into cancer cells; and 5) intracellular drug release (Figure 3).[41] The anticancer efficacy of loaded drugs is

determined by the entire delivery efficiency of nanocarriers.[41] The cascade involves the above-mentioned five steps. Thus, optimizing each step is crucial for achieving high total efficiency. It is more important to ensure that none of efficiency of each step approaches zero. Otherwise, this will be the Achilles heel of the entire delivery cascade.

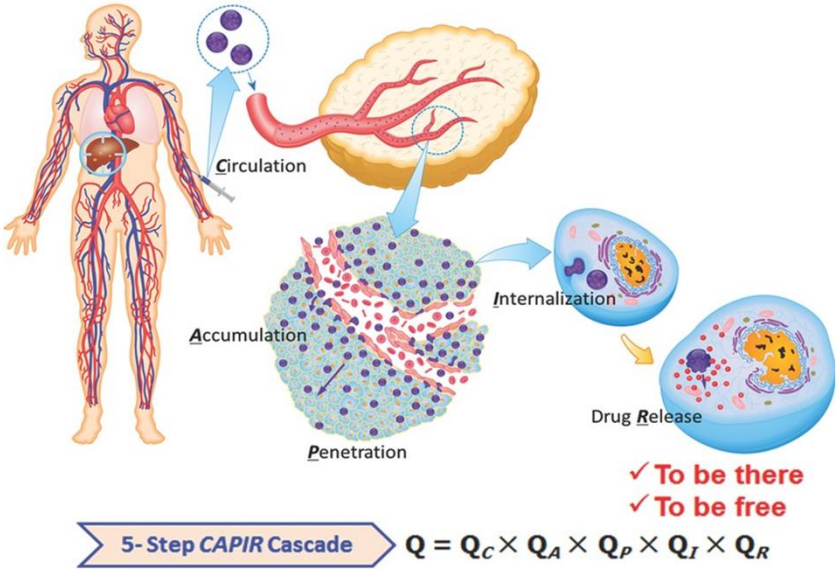

Figure 3. Five-step cascade of nanocarriers. Adapted with permission from ref 41. Copyright 2017 WI LEY-VCH Verlag GmbH & Co. KGaA.

Circulation in blood. Proteins are easily absorbed onto nanocarriers in blood.[42] The complement system and opsonizing proteins tag nanocarriers as foreign substance.[42] Subsequently the tagged nanocarriers are cleared by macrophage and thus have short circulation time. Introducing of poly(ethylene glycol) (PEG) or its alternatives, such as polysaccharides,[42] poly(2-oxazoline)s,[43] and polyphosphoesters,[44] can prolong circulation time. This is due to the surface modification of PEG, forming a hydrated barrier, thus hindering the interaction between nanocarriers and specific proteins. The formed barrier reduce protein adsorption and prolong circulation.

Accumulation at tumor sites. There are two basic strategies to enhance the accumulation of nanocarriers at tumor sites, either by passive accumulation (passive

targeting) or tumor-targeting vectors (active targeting). Passive targeting can be achieved through the enhanced permeability and retention (EPR) effect of nanocarriers.[45] Whereas, active targeting realize tumor accumulation through the conjugation of specific targeting ligands.[23]

Penetration into deep tumor tissues. The heterogeneity of tumor tissues have a number of biological obstacles, such as cancer-associated fibroblasts and high interstitial pressure.[46] These obstacles hinder the deep penetration of nanocarriers, thus obstructing the therapeutic efficacy of drug-loaded nanocarriers. Researchers have developed recombinant human hyaluronidase (PH20), onto the surface of nanocarriers to enhance the drug penetration in tumors.[47] PH20 could degrade the tumor extracellular matrix to facilitate interstitial diffusion, thus enhancing the penetration depth of nanocarriers.[47]

Internalization into cancer cells. Internalization refers a cellular process that nanocarriers are taken up into cells. Surface modification of specific ligands provides high internalization of nanocarriers. The ligands bind to the receptors which are expressed on the surface of cancer cells. The specific ligand-receptor recognition could activate the intracellular signal and promote the cell internalization of nanocarriers.[23]

Intracellular drug release. Stimuli-responsive nanocarriers trigger the on-demand drug release. These stimuli could be endogenous owing to the difference between tumor and normal tissues, including pH, redox potential, reactive oxygen species level and enzyme.[48] Drug release can be also triggered via exogenous stimuli such as light, magnetic field, ultrasound and electric field.[48] In comparison to those non-responsive nanocarriers in which drugs are released by uncontrollable spontaneous diffusion, stimuli-responsive nanocarriers enable for high release behavior.

1.2.2 Physicochemical properties of nanocarriers

The delivery efficiency is influenced by the physicochemical properties of nanocarriers.[49] The size, surface charge and shape of nanocarriers are the major determination of actions in biological environments.

Size. Size directly determines the surface area of nanocarriers.[50] The surface area significantly influences the protein absorption during circulation. Smaller nanocarriers was found to absorb more lipoproteins, such as clusterin.[51] Whereas, larger nanocarriers attracted higher affinity towards complement related proteins, such as prothrombin and gelsolin.[51] The specific absorbed protein can be further recognized by macrophage, which then lead to eliminate nanocarriers. Different types of absorbed proteins result in varying internalization of macrophage.[52] As a result, the smaller nanocarriers similarly exhibited slower elimination rate, comparing with the much faster elimination of larger nanocarriers.

The size of nanocarriers is also crucial for accumulation and penetration at tumor sites.[50] Because most nanocarriers accumulate at tumor sites via EPR effect. Nanocarriers with smaller size are easy to permeate from blood vessel to tumors. Thus, decreasing the size affect their vascular permeation positively, increasing the accumulation of nanocarriers. Moreover, smaller nanocarriers are obviously beneficial for penetrating deeper through the tumor matrix, while larger nanocarriers only stayed near the vasculature.[40]

Surface charge. Surface charge affects the protein absorption during circulation.[50] Positively charged nanocarriers adsorb more proteins than those with negatively charged. Neutral charged nanocarriers exhibited significantly reduced protein absorption.[50] Abundant protein absorption results in higher recognition by macrophage,

which contribute to blood clearance. Therefore, nanocarriers with neutral or negative charge show lower clearance rate, achieving long circulation time.

In addition, cell internalization process is also influenced by surface charge of nanocarriers.[53] Biological cell membrane exhibits negative charge. Positively charged nanocarriers are generally efficiently taken up than negatively charged ones. Similarly, charged nanocarriers are taken up better than their uncharged counterparts.

Shape. Shape is another important physicochemical property that determines the blood circulation.[50] Various shapes of nanocarriers can be taken up by macrophages at different rates, resulting in varying circulation times. Specifically, non-spherical nanocarriers have deviating hydrodynamic behaviors compared to the spherical ones. Previous studies indicated that non-spherical shape like filomicelles, nanorods, nanowires, and nanodisks have extended circulation time compared to their spherical counterparts.[50]

The shape of nanocarriers also have impact on the accumulation at tumor sites. Non-spherical nanocarriers have distinct motions that include tumbling and rolling, resulting in distinct margination dynamics.[54] Elongated nanocarriers, on the other hand, typically have less drag and larger surface areas than spheres.[54] Therefore, defined non-spherical nanocarriers can strongly adhere to the endothelial walls due to enhanced multivalent bonding, showing lower accumulation rates.

1.3 Nanocarriers based on ruthenium complexes for anticancer treatment

1.3.1 Ru complexes in cancer therapy

Recently, metallodrugs have attracted interest for cancer treatment.[16, 55-57] Among them, ruthenium (Ru) complexes have drawn highly attention because of their unique properties.[58, 59] The nature and the numbers of ligands, that coordinated to Ru(II) centers,

can be varied to tune the physicochemical properties of these complexes. These characteristics makes them attractive in biomedical field, for example, as new classes of anticancer agents for chemotherapy, photosensitizers for photodynamic therapy (PDT) and photoactivatable prodrugs for photoactivated chemotherapy (PACT).[59]

1.3.1.1 Ru complexes as anticancer agents for chemotherapy

Various Ru complexes have been developed and found to exhibit anticancer activities. Till now, three of them have entered in clinical trial, including KP1019,[60] KP1339,[61] and NAMI-A (Figure 4).[62] Ru complexes hold efficient cellular uptake against cancer cells. After taken up by cancer cells, they can interact with DNA, blocking the synthesis of DNA or protein, thus achieving the cell death.[58] These results encourage researchers to design more Ru complexes with desirable activities for cancer treatment.

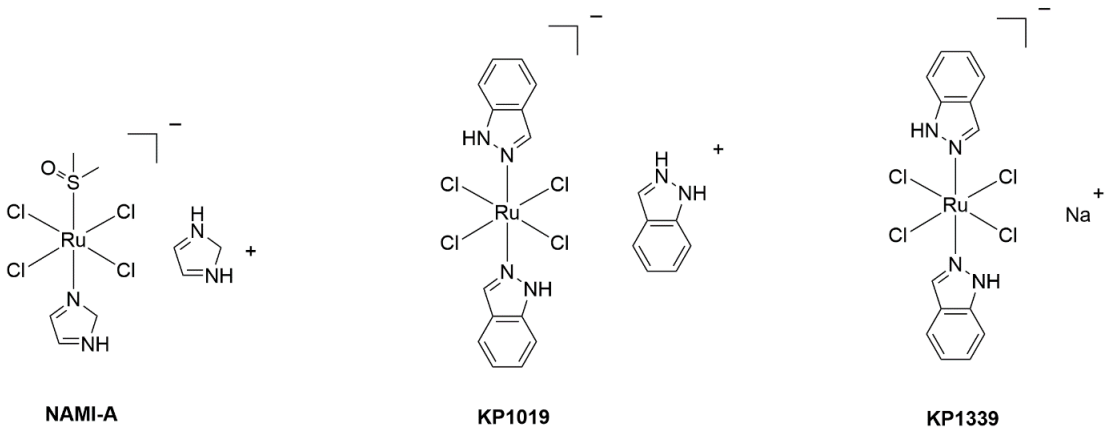

Figure 4. Chemical structure of anticancer agents, NAMI-A, KP1019 and KP1339.

Zeng and coworkers developed chiral structural Ru complexes **1a** and **1b**, which their toxicity depends on the cellular localization (Figure 5).[63] They found that these complexes inhibited the cell growth when they located in the cell nucleus. However, when they mainly enriched in the cytoplasm, the cytotoxicity dramatically decreased and showed negligible anticancer performance.

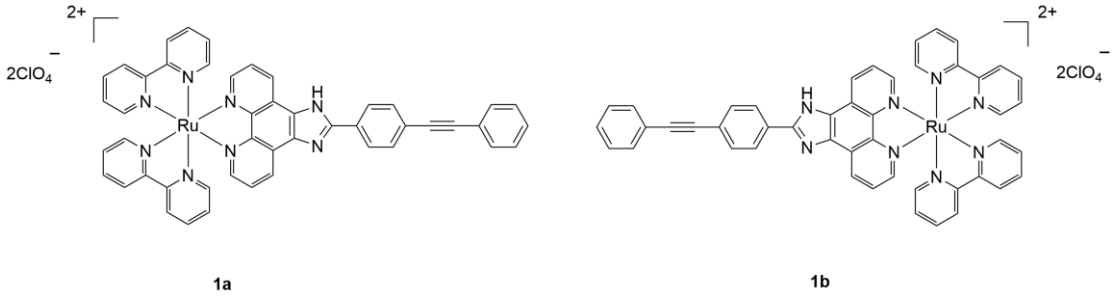

Figure 5. Chemical structure of Ru complex **1a-b**.[63]

Since the toxicity caused by Ru complexes strongly depends on their cellular localization. Afterwards, both Liu's and Chen's groups designed a series of Ru complexes **2a-2e**, which can target mitochondria (Figure 6).[64-69] Mitochondria acts as an important targeting organelle for anticancer drug in chemotherapy. They found all these Ru complexes caused cell apoptosis efficiently via a mitochondrial pathway.

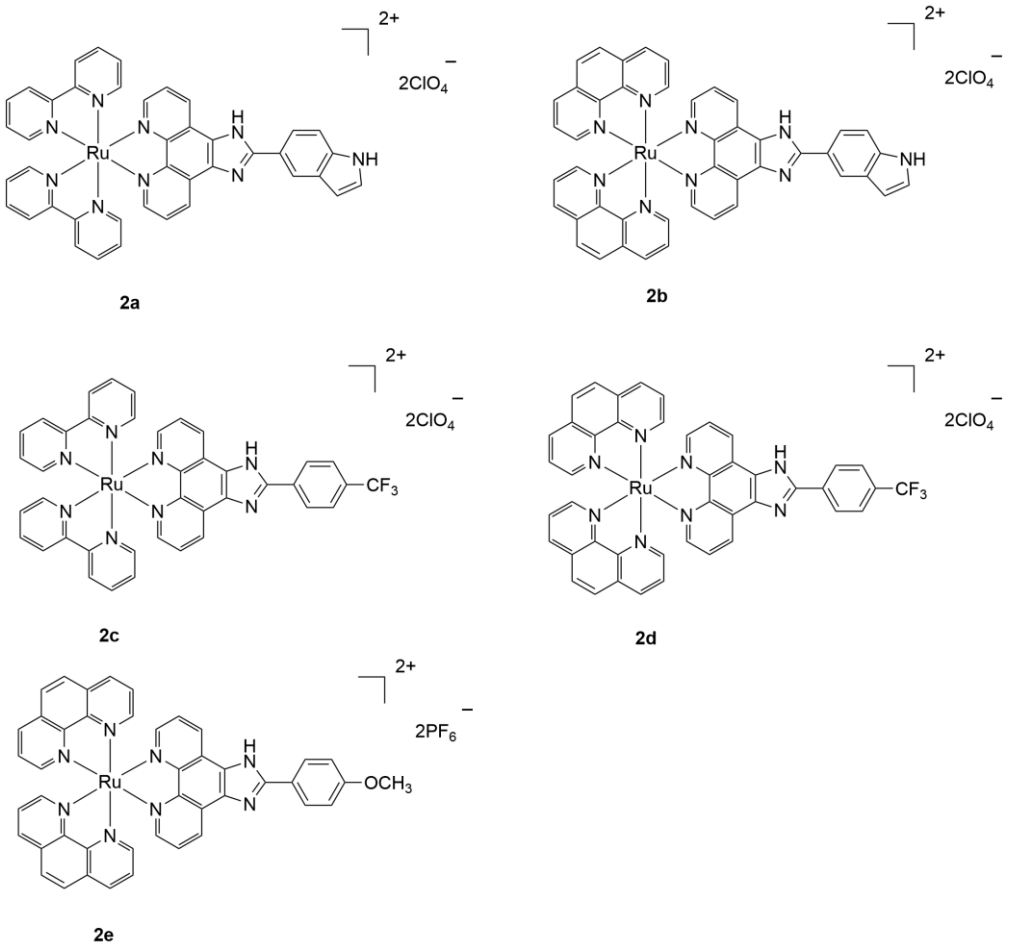

Figure 6. Chemical structure of Ru complexes **2a-e**.[64-69]

1.3.1.2 Ru complexes as photosensitizers for photodynamic therapy

Ru complexes using in PDT is relied on the generation of reactive oxygen species (ROS), to cause cell damage. Upon light irradiation, Ru complexes transform from their ground states (singlet state) into relatively long-lived excited states (triplet state).[70] The excited triplet state then enables the production of ROS by two pathways. First, it can directly react with a substrate, such as the cell membrane or a molecule, and transfers an electron to form radicals. These radicals interact with oxygen to generate oxygenated products (type I PDT pathway).[71, 72] Alternatively, the excited Ru complexes can transfer their energy to oxygen, to form singlet oxygen ($^1O_2$) (type II PDT pathway).[71, 72] $^1O_2$ is a toxic species, which further cause cell damage. The ROS species generated from two pathways can both kill cancer cells.

As a pioneer, McFarland and coworker designed a series of Ru complexes **3a-3d**, with variable lengths of polythiophene chains, using in PDT (Figure 7).[73] By introducing the polythiophene chain, these complexes hold low-lying intraligand (^{3}IL) excited states, exhibiting high $^1O_2$ production abilities. The $^1O_2$ quantum yields increased with the increment of polythiophene chain. The toxicities of these complexes were very low in the dark, whereas can be enhanced 200-fold upon light irradiation. Worth of note, **3c** in this family is currently undergoing human phase IB clinical trials, which is the well-known photosensitizers, TLD-1433.

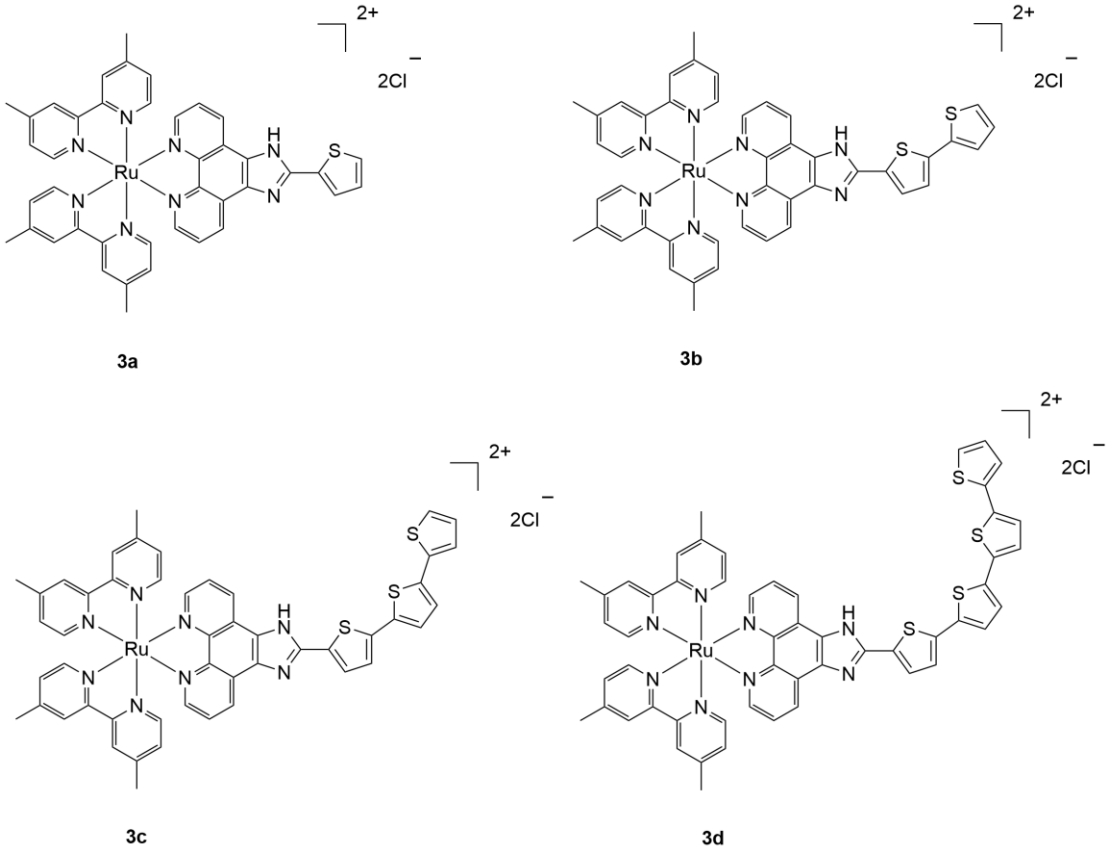

Figure 7. Chemical structure of Ru complexes **3a-d**.[73]

The same group later reported another Ru complexes **4**, which also possessed the properties of low-energy and long-lived ^{3}IL excited states (Figure 8).[74] **4** contains a π-expansive dppn ligand (dppn = benzo[i]dipyrido[3,2- a:2',3'-c]phenazine), which proved to be extremely sensitive to trace amounts of oxygen, leading to efficient PDT even under hypoxic conditions.

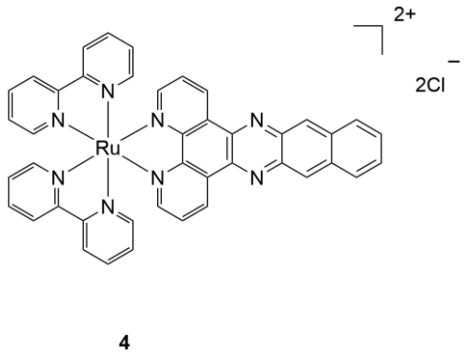

Figure 8. Chemical structure of Ru complexes **4**.[74]

Recently, a series of highly charged Ru complexes **5a-5c** was developed by Chao and coworkers.[75] In all these complexes, $[Ru(bpy)_3]^{2+}$ (bpy = 4,4'-bipyridine) was chosen as the architecture because of its excellent two-photon absorption (TPA) properties. Tertiary ammonium groups were modified on the surface, to increase the water solubility and the binding affinity towards cell membrane (Figure 9). Moreover, **5a-5c** were found to localize in lysosome, which is a favorable location for PDT. Lysosomes are associated with cell apoptosis and necrosis. As a result, upon irradiation, the generation of $^1O_2$ possessed significant anticancer performance.

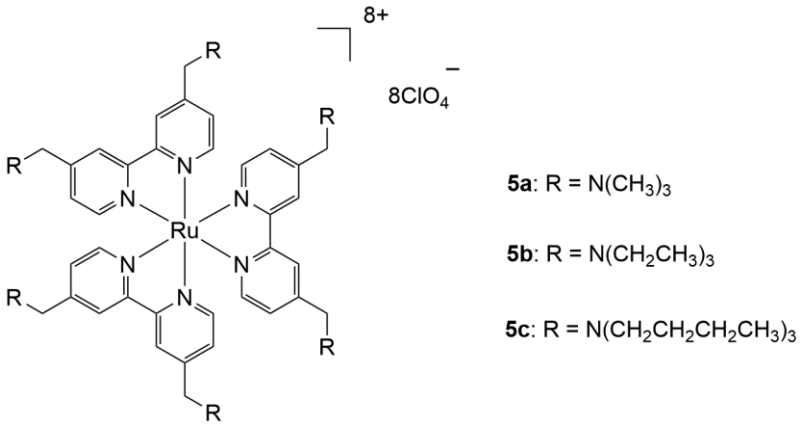

Figure 9. Chemical structure of Ru complexes **5a-5c**.[75]

1.3.1.3 Ru complexes as prodrugs for photoactivated chemotherapy

Similar to PDT, photoactivatable Ru complexes in PACT are also poorly toxic in darkness but become highly toxic after light irradiation.[76] However, the toxic species are the released components instead of the generated $^1O_2$.[77] Chemically speaking, photoactivatable Ru complexes possess an activity-inhibited therapeutic moiety and a photolytic bond.[76] The non-irradiated Ru complexes are inactive to biological environment. Upon light irradiation, the photolytic bond are cleaved and release the toxic moieties, which further interact with DNA, lipids or protein of cancer cells.

The mechanism of action of photolytic Ru complexes is based on their d^6-metal structure.[77] The photochemical behavior of these complexes have the nature with lowest lying triplet state. Upon light irradiation, the triplet excited states of metal-to-ligand character (^{3}MLCT) interconvert into low-lying triplet metal-centered (^{3}MC) states or d-d states (Figure 10).[78] This characteristic offer a strong dissociation ability, leading to a ligand substitution and resulting in the release of leaving groups such as the toxic moiety.

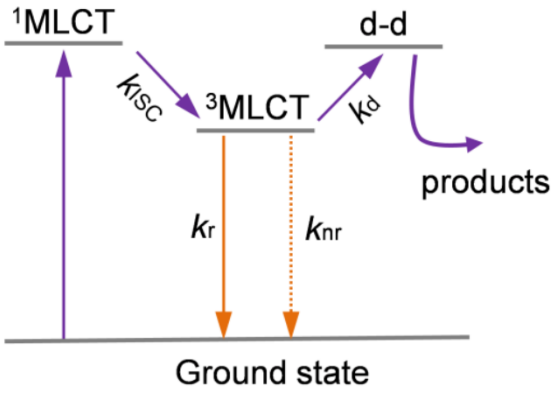

Figure 10. The mechanism of action of photolytic Ru complexes.

The toxic moiety can be anticancer drugs. Ru complexes act as caging moieties for the photo-induced release of anticancer drugs. In 2015, Renfrew and coworkers developed a Ru complex **6** which was used for releasing imidazole-based drug, econazole (Figure 11).[79] Econazole is used for oral and intravenous applications in cancer treatment.[80] When caged by Ru complex, it showed negligible toxicity against several kinds of cancer cells. However, upon green light irradiation, **6** caused the release of econazole drug, which then resulted in a 34-fold increment in cytotoxicity against cancer cells.

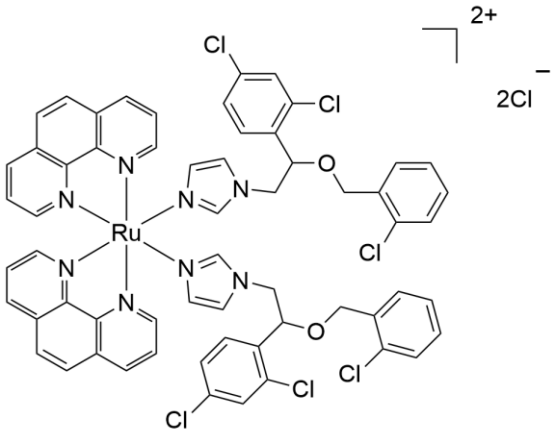

6

Figure 11. Chemical structure of Ru complexes **6**.[79]

Recently, Bonnet and coworkers designed two Ru complexes **7a-7b**, for the photo-induced releasing a toxic nicotinamide phosphoribosyltransferase (NAMPT) inhibitor STF-31 (Figure 12).[81] The inhibition of NAMPT can induce apoptosis of cancer cells. When STF-31 coordinated to Ru center, the toxicity was restricted via complexation. Upon light irradiation, both **7a** and **7b** uncaged the inhibitor STF-31, exhibiting enhanced toxicity against cancer cells under normoxia and even hypoxia conditions.

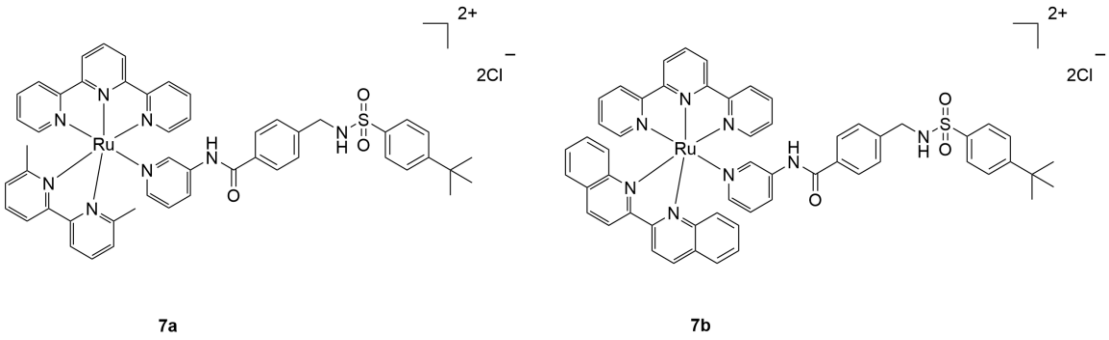

7a **7b**

Figure 12. Chemical structure of Ru complexes **7a-b**.[81]

The toxic moiety can also be the photolytic Ru complexes. Ru complexes were in parallel used as the photo-released drug candidates. Glazer and coworkers reported two photolytic Ru complexes **8a-8b** with sterically clashing ligands (Figure 13).[82] Light

irradiation of **8a** caused the release of dm-bpy (dm-bpy = 4,4' -dimethyl- 2,2' -dipyridyl) ligand, whereas **8b** released dm-dpq (dm-dpq = 2,9-dimethyl-dipyrido[3,2-f:2',3'-h]quinoxaline) ligand. Both of them formed toxic $[Ru(bpy)_2]^{2+}$ complex. The toxic Ru complexes bound cellular DNA and killed cancer cells. Moreover, the researchers also found that the photoreaction kinetics was 30-fold faster for **8a** than for **8b**, due to the rigidity of dm-dpq ligand. This further caused the photo-induced cytotoxicity of **8a** was higher than **8b**, thus killing cancer cells more efficiently.

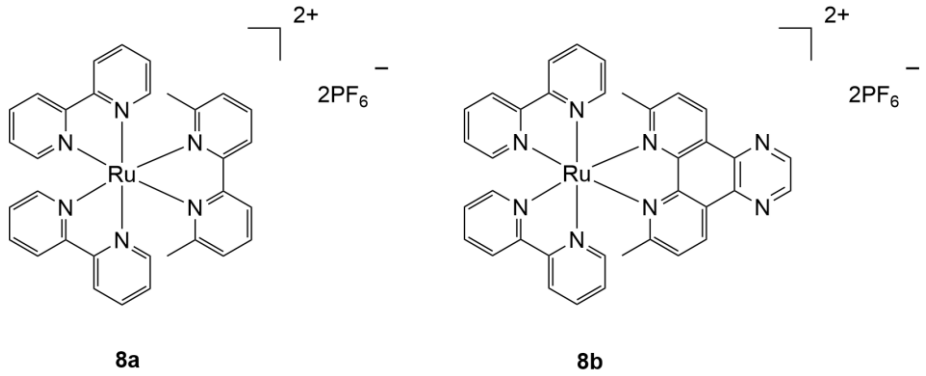

Figure 13. Chemical structure of Ru complexes **8a-b**.[82]

Recently, Turro and coworkers synthesized a novel cyclometalated Ru complexes **9**, for photo-induced ligand dissociation (Figure 14).[83] Such cyclometalated ligand resulted in geometric distortion of Ru complex and thus red-shifted the absorption wavelength. They found that **9** can be cleaved at 690 nm light irradiation, which was located in the therapeutic window for biomedical applications. After irradiation, the released toxic Ru complex further covalently bound to DNA, resulting in an enhancement of 14-fold toxicity compared with that in the dark.

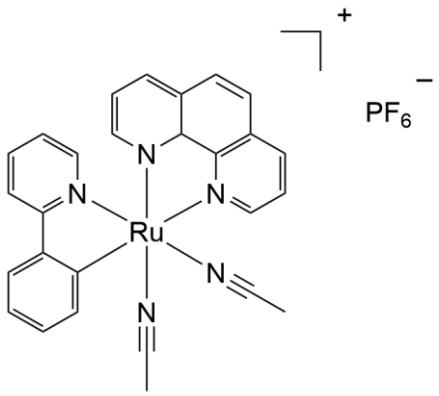

9

Figure 14. Chemical structure of Ru complexes **9**.[83]

1.3.2 Nanocarriers based on Ru complexes for cancer therapy

Although Ru complexes hold great potential for cancer therapy, they still suffer limitations due to the poor aqueous solubility. Moreover, most Ru complexes have short half-life and are easily eliminated during blood circulation. They also lack targeting ability, which limit the amount of complexes that reach the tumor tissues. Therefore, nanocarriers are highly required for delivering Ru complexes to address these issues.[84]

Nanocarriers-mediated Ru complexes for cancer treatment have several advantages. Typically, PEGylated nanocarriers prolong blood circulation. Besides, nanocarriers-mediated Ru complexes enable the accumulation at tumor sites via EPR effect. Light irradiation activates the Ru complexes only at the tumor sites, achieving selective tumor killing. There are two main strategies for nanocarriers-mediated Ru complexes: 1) physical encapsulation of Ru complexes within nanocarriers; 2) covalent conjugation of Ru complexes to nanocarriers.[84]

1.3.2.1 Physical encapsulation of Ru complexes within nanocarriers

Physical encapsulation relies on the non-covalent interaction between Ru complexes and nanocarriers matrix. Physical encapsulation restricts the exposure of Ru complexes to healthy tissues and shields them from clearance during circulation. Ru complexes are encapsulated into nanocarriers such as micelles, liposomes or nanoparticles.

Glazer and coworkers reported the encapsulation of three Ru complexes into nanoassembled micelles (Figure 15).[85] These Ru complexes were varied with different hydrophobicity. They found that the increased hydrophobicity decreased the total release amount, and slowed down release rate of Ru complexes. The release behaviors were also influenced by ionic strength of the solution, but variations in pH had negligible effect. The released complexes from nanoassembled micelles were further used for treating A549 cancer cells, which showed improved pharmacological properties.

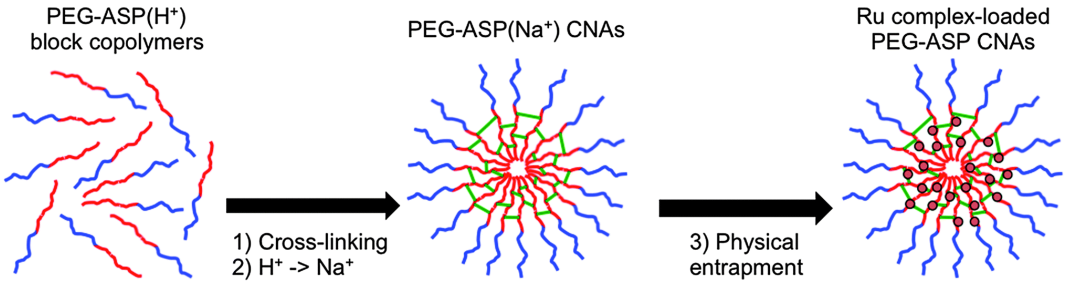

Figure 15. Ru complexes were encapsulated in nanoassembled micelles. Adapted with permission from ref 85. Copyright 2016 Royal Society of Chemistry.

Keppler and coworkers prepared a nanoparticle formulation for encapsulating Ru complex, KP1019.[86] Poly(lactic acid) (PLA) nanoparticles with two different surfactants (Pluronic F68 and Tween 80) were prepared using oil-in-water emulsion. Comparing with Pluronic F68, Tween 80 was able to prevent the precipitation of KP1019 and allow reproducible preparation of KP1019-containing nanoparticles. The

choice of surfactant directly influences the encapsulation efficiency and nanoparticle stability of Ru complexes.

1.3.2.2 Covalent conjugation of Ru complexes to nanocarriers

The main drawbacks of physical encapsulation are the uncontrollable release of Ru complexes, which is so-called "burst" release.[84, 87] Physical encapsulation also suffers limitation due to the limited encapsulation amount. Covalent conjugation strategy may address these issues. Covalent conjugation using stimuli-responsive bonds enables controlled release behavior of Ru complexes.[88] Covalent conjugation can achieve high Ru loading amount by a well-defined chemical structure. Moreover, our group found that conjugating photo-responsive Ru complexes into polymeric nanocarriers, were more stable than free Ru complexes under similar conditions.[89] Photo-responsive Ru complexes can be also covalently developed for switchable surfaces,[90] and polymer gels,[91] by proper structural design. Recently, Ru complexes can be covalently conjugated to polymeric nanocarriers, or onto protein nanocarriers.

Our group designed and synthesized three block copolymers nanocarriers with red light-responsive Ru complexes in their side chains (Figure 16).[92] Each polymer contained a hydrophilic PEG block and a hydrophobic Ru-containing block. By proper design of the different hydrophilic/hydrophobic block ratio, these copolymers self-assembled into micelles, vesicles, and large compound micelles. All of them can be taken up by cancer cells, whereas the micelles exhibited the highest cellular uptake efficiency. Red light irradiation induced the release of Ru complexes and the generation of $^1O_2$, both of them synergistically killed the cancer cells.

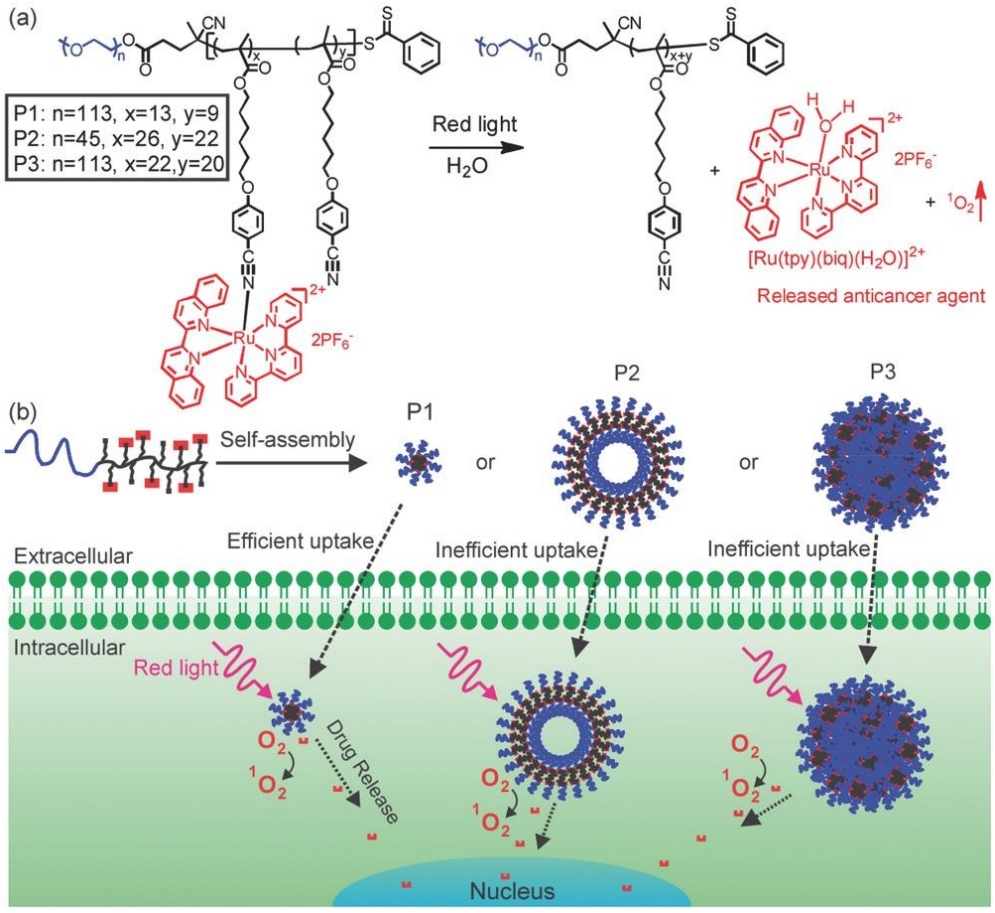

Figure 16. Ru complexes were covalently conjugated into polymer side chains. Adapted with permission from ref 92. Copyright 2016 WI LEY-VCH Verlag GmbH & Co. KGaA.

Our group later introduced Ru complexes into the main-chain of a polymeric nanocarriers (Figure 17).[93] The Ru-containing polymer possessed two hydrophilic PEG block and a hydrophobic Ru block, which further self-assembled into nanoparticles (PolyRu). PolyRu nanoparticles accumulated at tumor sites via EPR effect. Moreover, in this well-defined polymeric structure, Ru complexes achieved more than 50% drug loading efficiency. Ru complexes can be controllably released from PolyRu upon red light irradiation. The released toxic Ru complexes caused the inhibition of tumor growth, with the help of generated $^1O_2$.

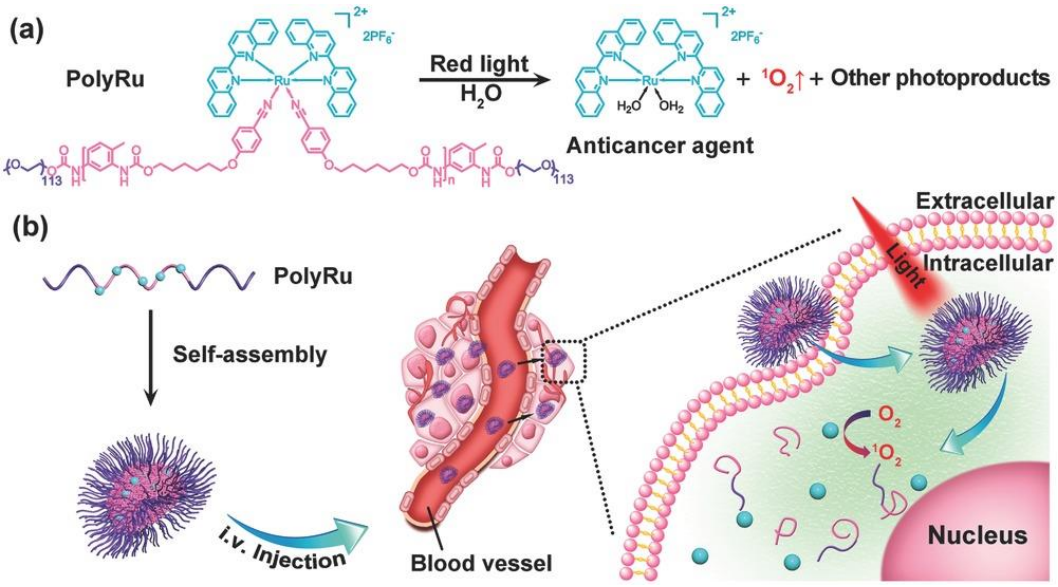

Figure 17. Ru complexes were covalently conjugated into polymer main chains. Adapted with permission from ref 93. Copyright 2017 WI LEY-VCH Verlag GmbH & Co. KGaA.

Ru complexes are also covalently conjugated onto natural protein naocarriers. Tanja and coworkers reported the use of blood plasma protein, serum albumin, for delivering Ru complexes (Figure 18).[94] They also introduced triphenylphosphine group on the protein surface, which offered the nanocarriers with mitochondria targeting ability. Irradiation of this nanocarriers can produce $^1O_2$ due to the photosensitized Ru complexes. Attaching multiple Ru complexes into one protein achieved extremely high toxicity under light irradiation, with an enhancement of 220-fold toxicity comparing with that in the dark.

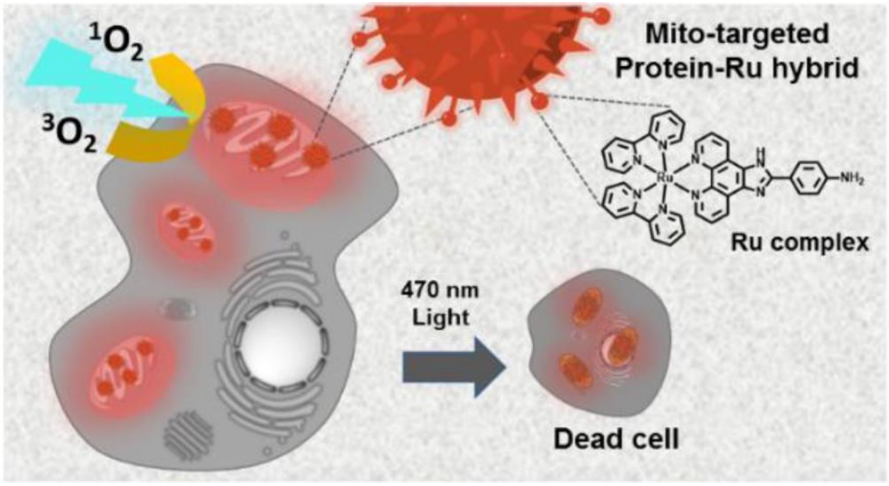

Figure 18. Ru complexes were covalently conjugated onto the surface of natural proteins. Adapted with permission from ref 94. Copyright 2017 American Chemical Society.

1.3.3 Challenges of nanocarriers based on Ru complexes in cancer therapy

A variety of nanocarriers for delivering Ru complexes have been developed in cancer therapy. However, they still suffer several limitations to reach their full potential. First, the current delivery efficiency of nanocarriers is still need to be improved. Desirable development of nanocarriers with high delivery efficiency is appreciated. Second, considering to the highly complexity of tumor, such as the resistance to anticancer drug, multifunctional nanocarriers based on Ru complexes for reversing drug resistance are emergently required. Thus, the major challenges of nanocarriers based on Ru complexes are: 1) how to enhance the delivery efficiency of these complexes, 2) and further overcome drug resistance in cancer treatment. In chapter 2, I will show the development of light-induced morphological change and positive charge increase, based on the light-cleavable Ru complexes, for improving the tumor penetration depth and cellular uptake efficiency in cancer treatment. To combat the complexity of tumor, in chapter 3, I am going to present my contribution to reverse drug resistance by

applying Ru complexes with combined chemotherapy, photodynamic therapy and photoactivated chemotherapy.

1.4 References

[1] Jha, P., Avoidable global cancer deaths and total deaths from smoking. *Nature Reviews Cancer* **2009,** *9* (9), 655-664.

[2] Bray, F.; Ferlay, J.; Soerjomataram, I.; Siegel, R. L.; Torre, L. A.; Jemal, A., Global cancer statistics 2018: GLOBOCAN estimates of incidence and mortality worldwide for 36 cancers in 185 countries. *CA: a cancer journal for clinicians* **2018,** *68* (6), 394-424.

[3] Herskovic, A.; Martz, K.; Al-Sarraf, M.; Leichman, L.; Brindle, J.; Vaitkevicius, V.; Cooper, J.; Byhardt, R.; Davis, L.; Emami, B., Combined chemotherapy and radiotherapy compared with radiotherapy alone in patients with cancer of the esophagus. *New England Journal of Medicine* **1992,** *326* (24), 1593-1598.

[4] Vasan, N.; Baselga, J.; Hyman, D. M., A view on drug resistance in cancer. *Nature* **2019,** *575* (7782), 299-309.

[5] Sobot, D.; Mura, S.; Couvreur, P., How can nanomedicines overcome cellular-based anticancer drug resistance? *Journal of Materials Chemistry B* **2016,** *4* (30), 5078-5100.

[6] Pisco, A. O.; Jackson, D. A.; Huang, S., Reduced intracellular drug accumulation in drug-resistant leukemia cells is not only solely due to MDR-mediated efflux but also to decreased uptake. *Frontiers in oncology* **2014,** *4*, 306.

[7] Muley, H.; Fadó, R.; Rodríguez-Rodríguez, R.; Casals, N., Drug uptake-based chemoresistance in breast cancer treatment. *Biochemical pharmacology* **2020**, 113959.

[8] Yang, N. J.; Hinner, M. J., Getting across the cell membrane: an overview for small molecules, peptides, and proteins. *Site-specific protein labeling* **2015**, 29-53.

[9] Mansoori, B.; Mohammadi, A.; Davudian, S.; Shirjang, S.; Baradaran, B., The different mechanisms of cancer drug resistance: a brief review. *Advanced pharmaceutical bulletin* **2017,** *7* (3), 339.

[10] Fletcher, J. I.; Haber, M.; Henderson, M. J.; Norris, M. D., ABC transporters in cancer: more than just drug efflux pumps. *Nature Reviews Cancer* **2010,** *10* (2), 147-156.

[11] Löscher, W.; Potschka, H., Drug resistance in brain diseases and the role of drug efflux transporters. *Nature Reviews Neuroscience* **2005,** *6* (8), 591-602.

[12] Smyth, M. J.; Krasovskis, E.; Sutton, V. R.; Johnstone, R. W., The drug efflux protein, P-glycoprotein, additionally protects drug-resistant tumor cells from multiple forms of caspase-dependent apoptosis. *Proceedings of the National Academy of Sciences* **1998,** *95* (12), 7024-7029.

[13] Helleday, T.; Petermann, E.; Lundin, C.; Hodgson, B.; Sharma, R. A., DNA repair pathways as targets for cancer therapy. *Nature Reviews Cancer* **2008,** *8* (3), 193-204.

[14] Zhang, S.; Zhong, X.; Yuan, H.; Guo, Y.; Song, D.; Qi, F.; Zhu, Z.; Wang, X.; Guo, Z., Interfering in apoptosis and DNA repair of cancer cells to conquer cisplatin resistance by platinum (IV) prodrugs. *Chemical Science* **2020,** *11* (15), 3829-3835.

[15] Hurley, L. H., DNA and its associated processes as targets for cancer therapy. *Nature Reviews Cancer* **2002,** *2* (3), 188-200.

[16] Johnstone, T. C.; Suntharalingam, K.; Lippard, S. J., The next generation of platinum drugs: targeted Pt (II) agents, nanoparticle delivery, and Pt (IV) prodrugs. *Chemical reviews* **2016,** *116* (5), 3436-3486.

[17] Genovese, I.; Fiorillo, A.; Ilari, A.; Masciarelli, S.; Fazi, F.; Colotti, G., Binding of doxorubicin to Sorcin impairs cell death and increases drug resistance in cancer cells. *Cell death & disease* **2017,** *8* (7), e2950-e2950.

[18] Damia, G.; D'Incalci, M., Mechanisms of resistance to alkylating agents. *Cytotechnology* **1998,** *27* (1), 165-173.

[19] Rodriguez-Antona, C.; Ingelman-Sundberg, M., Cytochrome P 450 pharmacogenetics and cancer. *Oncogene* **2006,** *25* (11), 1679-1691.

[20] Wang, X.; Zhang, H.; Chen, X., Drug resistance and combating drug resistance in cancer. *Cancer Drug Resistance* **2019,** *2* (2), 141-160.

[21] Saraswathy, M.; Gong, S., Different strategies to overcome multidrug resistance in cancer. *Biotechnology advances* **2013,** *31* (8), 1397-1407.

[22] Loganzo, F.; Sung, M.; Gerber, H.-P., Mechanisms of resistance to antibody–drug conjugates. *Molecular cancer therapeutics* **2016,** *15* (12), 2825-2834.

[23] Zolot, R. S.; Basu, S.; Million, R. P., Antibody–drug conjugates. *Nature Reviews Drug Discovery* **2013,** *12* (4), 259-260.

[24] Worm, D. J.; Els‐Heindl, S.; Beck‐Sickinger, A. G., Targeting of peptide‐binding receptors on cancer cells with peptide‐drug conjugates. *Peptide Science* **2020,** *112* (3), e24171.

[25] Tang, J.; Zhang, L.; Gao, H.; Liu, Y.; Zhang, Q.; Ran, R.; Zhang, Z.; He, Q., Co-delivery of doxorubicin and P-gp inhibitor by a reduction-sensitive liposome to overcome multidrug resistance, enhance anti-tumor efficiency and reduce toxicity. *Drug Delivery* **2016,** *23* (4), 1130-1143.

[26] Zhang, M.; Hagan IV, C. T.; Min, Y.; Foley, H.; Tian, X.; Yang, F.; Mi, Y.; Au, K. M.; Medik, Y.; Roche, K., Nanoparticle co-delivery of wortmannin and cisplatin synergistically enhances chemoradiotherapy and reverses platinum resistance in ovarian cancer models. *Biomaterials* **2018,** *169*, 1-10.

[27] Kim, R. B., Drugs as P-glycoprotein substrates, inhibitors, and inducers. *Drug metabolism reviews* **2002,** *34* (1-2), 47-54.

[28] Xiao, X.; Wang, K.; Zong, Q.; Tu, Y.; Dong, Y.; Yuan, Y., Polyprodrug with glutathione depletion and cascade drug activation for multi-drug resistance reversal. *Biomaterials* **2021,** *270*, 120649.

[29] Han, Y.; Yin, W.; Li, J.; Zhao, H.; Zha, Z.; Ke, W.; Wang, Y.; He, C.; Ge, Z., Intracellular glutathione-depleting polymeric micelles for cisplatin prodrug delivery to overcome cisplatin resistance of cancers. *Journal of Controlled Release* **2018,** *273*, 30-39.

[30] Drew, R.; Miners, J. O., The effects of buthionine sulphoximine (BSO) on glutathione depletion and xenobiotic biotransformation. *Biochemical pharmacology* **1984,** *33* (19), 2989-2994.

[31] Li, Q.; Yin, X.; Wang, W.; Zhan, M.; Zhao, B.; Hou, Z.; Wang, J., The effects of buthionine sulfoximine on the proliferation and apoptosis of biliary tract cancer cells induced by cisplatin and gemcitabine. *Oncology letters* **2016,** *11* (1), 474-480.

[32] Wang, N.; Cheng, X.; Li, N.; Wang, H.; Chen, H., Nanocarriers and their loading strategies. *Advanced healthcare materials* **2019,** *8* (6), 1801002.

[33] Karges, J.; Yempala, T.; Tharaud, M.; Gibson, D.; Gasser, G., A Multi‐action and Multi‐target RuII–PtIV Conjugate Combining Cancer‐Activated Chemotherapy and Photodynamic Therapy to Overcome Drug Resistant Cancers. *Angewandte Chemie International Edition* **2020,** *59* (18), 7069-7075.

[34] Lin, G.; Mi, P.; Chu, C.; Zhang, J.; Liu, G., Inorganic nanocarriers overcoming multidrug resistance for cancer theranostics. *Advanced science* **2016,** *3* (11), 1600134.

[35] Li, Z.; Shan, X.; Chen, Z.; Gao, N.; Zeng, W.; Zeng, X.; Mei, L., Applications of Surface Modification Technologies in Nanomedicine for Deep Tumor Penetration. *Advanced Science* **2021,** *8* (1), 2002589.

[36] Goddard, Z. R.; Marín, M. J.; Russell, D. A.; Searcey, M., Active targeting of gold nanoparticles as cancer therapeutics. *Chemical Society Reviews* **2020**.

[37] Schöttler, S.; Becker, G.; Winzen, S.; Steinbach, T.; Mohr, K.; Landfester, K.; Mailänder, V.; Wurm, F. R., Protein adsorption is required for stealth effect of poly (ethylene glycol)-and poly (phosphoester)-coated nanocarriers. *Nature nanotechnology* **2016,** *11* (4), 372-377.

[38] Dewhirst, M. W.; Secomb, T. W., Transport of drugs from blood vessels to tumour tissue. *Nat Rev Cancer* **2017,** *17* (12), 738-750.

[39] Torney, F.; Trewyn, B. G.; Lin, V. S.; Wang, K., Mesoporous silica nanoparticles deliver DNA and chemicals into plants. *Nat Nanotechnol* **2007,** *2* (5), 295-300.

[40] Shan, Y.; Ma, S.; Nie, L.; Shang, X.; Hao, X.; Tang, Z.; Wang, H., Size-dependent endocytosis of single gold nanoparticles. *Chem Commun (Camb)* **2011,** *47* (28), 8091-3.

[41] Sun, Q.; Zhou, Z.; Qiu, N.; Shen, Y., Rational design of cancer nanomedicine: nanoproperty integration and synchronization. *Advanced materials* **2017,** *29* (14), 1606628.

[42] Schöttler, S.; Landfester, K.; Mailänder, V., Controlling the stealth effect of nanocarriers through understanding the protein corona. *Angewandte Chemie International Edition* **2016,** *55* (31), 8806-8815.

[43] Sedlacek, O.; Monnery, B. D.; Filippov, S. K.; Hoogenboom, R.; Hruby, M., Poly (2‐Oxazoline) s–Are They More Advantageous for Biomedical Applications Than Other Polymers? *Macromolecular rapid communications* **2012,** *33* (19), 1648-1662.

[44] Simon, J.; Wolf, T.; Klein, K.; Landfester, K.; Wurm, F. R.; Mailänder, V., Hydrophilicity Regulates the Stealth Properties of Polyphosphoester‐Coated Nanocarriers. *Angewandte Chemie International Edition* **2018,** *57* (19), 5548-5553.

[45] Torchilin, V., Tumor delivery of macromolecular drugs based on the EPR effect. *Advanced drug delivery reviews* **2011,** *63* (3), 131-135.

[46] Liu, T.; Han, C.; Wang, S.; Fang, P.; Ma, Z.; Xu, L.; Yin, R., Cancer-associated fibroblasts: an emerging target of anti-cancer immunotherapy. *Journal of hematology & oncology* **2019,** *12* (1), 1-15.

[47] Hong, Y.; Nam, G. H.; Koh, E.; Jeon, S.; Kim, G. B.; Jeong, C.; Kim, D. H.; Yang, Y.; Kim, I. S., Exosome as a vehicle for delivery of membrane protein therapeutics, PH20, for enhanced tumor penetration and antitumor efficacy. *Advanced Functional Materials* **2018,** *28* (5), 1703074.

[48] Mura, S.; Nicolas, J.; Couvreur, P., Stimuli-responsive nanocarriers for drug delivery. *Nature materials* **2013,** *12* (11), 991-1003.

[49] Li, Z.; Xiao, C.; Yong, T.; Li, Z.; Gan, L.; Yang, X., Influence of nanomedicine mechanical properties on tumor targeting delivery. *Chemical Society Reviews* **2020,** *49* (8), 2273-2290.

[50] Jo, D. H.; Kim, J. H.; Lee, T. G.; Kim, J. H., Size, surface charge, and shape determine therapeutic effects of nanoparticles on brain and retinal diseases. *Nanomedicine: Nanotechnology, Biology and Medicine* **2015,** *11* (7), 1603-1611.

[51] Zhao, Z.; Ukidve, A.; Krishnan, V.; Mitragotri, S., Effect of physicochemical and surface properties on in vivo fate of drug nanocarriers. *Advanced drug delivery reviews* **2019,** *143*, 3-21.

[52] Behzadi, S.; Serpooshan, V.; Tao, W.; Hamaly, M. A.; Alkawareek, M. Y.; Dreaden, E. C.; Brown, D.; Alkilany, A. M.; Farokhzad, O. C.; Mahmoudi, M., Cellular uptake of nanoparticles: journey inside the cell. *Chemical Society Reviews* **2017,** *46* (14), 4218-4244.

[53] Calatayud, M. P.; Sanz, B.; Raffa, V.; Riggio, C.; Ibarra, M. R.; Goya, G. F., The effect of surface charge of functionalized Fe3O4 nanoparticles on protein adsorption and cell uptake. *Biomaterials* **2014,** *35* (24), 6389-6399.

[54] Ta, H. T.; Truong, N. P.; Whittaker, A. K.; Davis, T. P.; Peter, K., The effects of particle size, shape, density and flow characteristics on particle margination to vascular walls in cardiovascular diseases. *Expert opinion on drug delivery* **2018,** *15* (1), 33-45.

[55] Cisnetti, F.; Gautier, A., Metal/N‐Heterocyclic Carbene Complexes: Opportunities for the Development of Anticancer Metallodrugs. *Angewandte Chemie International Edition* **2013,** *52* (46), 11976-11978.

[56] Wang, X.; Wang, X.; Jin, S.; Muhammad, N.; Guo, Z., Stimuli-responsive therapeutic metallodrugs. *Chemical reviews* **2018,** *119* (2), 1138-1192.

[57] Mjos, K. D.; Orvig, C., Metallodrugs in medicinal inorganic chemistry. *Chemical reviews* **2014,** *114* (8), 4540-4563.

[58] Zeng, L.; Gupta, P.; Chen, Y.; Wang, E.; Ji, L.; Chao, H.; Chen, Z.-S., The development of anticancer ruthenium (II) complexes: from single molecule compounds to nanomaterials. *Chemical Society Reviews* **2017,** *46* (19), 5771-5804.

[59] Mari, C.; Pierroz, V.; Ferrari, S.; Gasser, G., Combination of Ru (II) complexes and light: new frontiers in cancer therapy. *Chemical science* **2015,** *6* (5), 2660-2686.

[60] Hartinger, C. G.; Jakupec, M. A.; Zorbas‐Seifried, S.; Groessl, M.; Egger, A.; Berger, W.; Zorbas, H.; Dyson, P. J.; Keppler, B. K., KP1019, a new redox‐active anticancer agent−Preclinical development and results of a clinical phase I study in tumor patients. *Chemistry & biodiversity* **2008,** *5* (10), 2140-2155.

[61] Heffeter, P.; Atil, B.; Kryeziu, K.; Groza, D.; Koellensperger, G.; Körner, W.; Jungwirth, U.; Mohr, T.; Keppler, B. K.; Berger, W., The ruthenium compound KP1339 potentiates the anticancer activity of sorafenib in vitro and in vivo. *European Journal of Cancer* **2013,** *49* (15), 3366-3375.

[62] Sava, G.; Zorzet, S.; Turrin, C.; Vita, F.; Soranzo, M.; Zabucchi, G.; Cocchietto, M.; Bergamo, A.; DiGiovine, S.; Pezzoni, G., Dual action of NAMI-A in inhibition of solid tumor metastasis: selective targeting of metastatic cells and binding to collagen. *Clinical Cancer Research* **2003,** *9* (5), 1898-1905.

[63] Zeng, Z.-P.; Wu, Q.; Sun, F.-Y.; Zheng, K.-D.; Mei, W.-J., Imaging Nuclei of MDA-MB-231 Breast Cancer Cells by Chiral Ruthenium (II) Complex Coordinated by 2-(4-Phenyacetylenephenyl)-1 H-imidazo [4, 5 f][1, 10] phenanthroline. *Inorganic chemistry* **2016,** *55* (11), 5710-5718.

[64] Yu, Q.; Liu, Y.; Xu, L.; Zheng, C.; Le, F.; Qin, X.; Liu, Y.; Liu, J., Ruthenium (II) polypyridyl complexes: Cellular uptake, cell image and apoptosis of HeLa cancer cells induced by double targets. *European journal of medicinal chemistry* **2014,** *82*, 82-95.

[65] Li, L.; Wong, Y.-S.; Chen, T.; Fan, C.; Zheng, W., Ruthenium complexes containing bis-benzimidazole derivatives as a new class of apoptosis inducers. *Dalton transactions* **2012,** *41* (4), 1138-1141.

[66] Chen, T.; Mei, W.-J.; Wong, Y.-S.; Liu, J.; Liu, Y.; Xie, H.-S.; Zheng, W.-J., Chiral ruthenium polypyridyl complexes as mitochondria-targeted apoptosis inducers. *MedChemComm* **2010,** *1* (1), 73-75.

[67] Zhao, Z.; Luo, Z.; Wu, Q.; Zheng, W.; Feng, Y.; Chen, T., Mixed-ligand ruthenium polypyridyl complexes as apoptosis inducers in cancer cells, the cellular translocation and the important role of ROS-mediated signaling. *Dalton Transactions* **2014,** *43* (45), 17017-17028.

[68] Du, Y.; Fu, X.; Li, H.; Chen, B.; Guo, Y.; Su, G.; Zhang, H.; Ning, F.; Lin, Y.; Mei, W., Mitochondrial fragmentation is an important cellular event induced by ruthenium (II) polypyridyl complexes in osteosarcoma cells. *ChemMedChem* **2014,** *9* (4), 714-718.

[69] Chen, T.; Liu, Y.; Zheng, W.-J.; Liu, J.; Wong, Y.-S., Ruthenium polypyridyl complexes that induce mitochondria-mediated apoptosis in cancer cells. *Inorganic chemistry* **2010,** *49* (14), 6366-6368.

[70] Heindl, M.; Hongyan, J.; Hua, S.-A.; Oelschlegel, M.; Meyer, F.; Schwarzer, D.; González, L., Excited-State Dynamics of [Ru (S–Sbpy)(bpy) 2] 2+ to Form Long-Lived Localized Triplet States. *Inorganic chemistry* **2021,** *60* (3), 1672-1682.

[71] Felsher, D. W., Cancer revoked: oncogenes as therapeutic targets. *Nature Reviews Cancer* **2003,** *3* (5), 375-379.

[72] Li, X.; Lovell, J. F.; Yoon, J.; Chen, X., Clinical development and potential of photothermal and photodynamic therapies for cancer. *Nature Reviews Clinical Oncology* **2020,** *17* (11), 657-674.

[73] Shi, G.; Monro, S.; Hennigar, R.; Colpitts, J.; Fong, J.; Kasimova, K.; Yin, H.; DeCoste, R.; Spencer, C.; Chamberlain, L., Ru (II) dyads derived from α-oligothiophenes: a new class of potent and versatile photosensitizers for PDT. *Coordination Chemistry Reviews* **2015,** *282*, 127-138.

[74] Yin, H.; Stephenson, M.; Gibson, J.; Sampson, E.; Shi, G.; Sainuddin, T.; Monro, S.; McFarland, S. A., In vitro multiwavelength PDT with 3IL states: Teaching old molecules new tricks. *Inorganic chemistry* **2014,** *53* (9), 4548-4559.

[75] Huang, H.; Yu, B.; Zhang, P.; Huang, J.; Chen, Y.; Gasser, G.; Ji, L.; Chao, H., Highly charged ruthenium (II) polypyridyl complexes as lysosome‐localized photosensitizers for two‐photon photodynamic therapy. *Angewandte Chemie International Edition* **2015,** *54* (47), 14049-14052.

[76] Bonnet, S., Why develop photoactivated chemotherapy? *Dalton Transactions* **2018,** *47* (31), 10330-10343.

[77] Farrer, N. J.; Salassa, L.; Sadler, P. J., Photoactivated chemotherapy (PACT): the potential of excited-state d-block metals in medicine. *Dalton Transactions* **2009,** (48), 10690-10701.

[78] Zayat, L.; Filevich, O.; Baraldo, L. M.; Etchenique, R., Ruthenium polypyridyl phototriggers: from beginnings to perspectives. *Philosophical Transactions of the Royal Society A: Mathematical, Physical and Engineering Sciences* **2013,** *371* (1995), 20120330.

[79] Karaoun, N.; Renfrew, A. K., A luminescent ruthenium (II) complex for light-triggered drug release and live cell imaging. *Chemical Communications* **2015,** *51* (74), 14038-14041.

[80] Choi, E. K.; Park, E. J.; Phan, T. T.; Kim, H. D.; Hoe, K.-L.; Kim, D.-U., Econazole Induces p53-Dependent Apoptosis and Decreases Metastasis Ability in Gastric Cancer Cells. *Biomolecules & therapeutics* **2020,** *28* (4), 370.

[81] Lameijer, L. N.; Ernst, D.; Hopkins, S. L.; Meijer, M. S.; Askes, S. H.; Le Dévédec, S. E.; Bonnet, S., A red‐light‐activated ruthenium‐caged NAMPT inhibitor remains phototoxic in hypoxic cancer cells. *Angewandte Chemie* **2017,** *129* (38), 11707-11711.

[82] Howerton, B. S.; Heidary, D. K.; Glazer, E. C., Strained ruthenium complexes are potent light-activated anticancer agents. *Journal of the American Chemical Society* **2012,** *134* (20), 8324-8327.

[83] Palmer, A. M.; Peña, B.; Sears, R. B.; Chen, O.; El Ojaimi, M.; Thummel, R. P.; Dunbar, K. R.; Turro, C., Cytotoxicity of cyclometallated ruthenium complexes: the role of ligand exchange on the activity. *Philosophical Transactions of the Royal Society A: Mathematical, Physical and Engineering Sciences* **2013,** *371* (1995), 20120135.

[84] Villemin, E.; Ong, Y. C.; Thomas, C. M.; Gasser, G., Polymer encapsulation of ruthenium complexes for biological and medicinal applications. *Nature Reviews Chemistry* **2019,** *3* (4), 261-282.

[85] Dickerson, M.; Howerton, B.; Bae, Y.; Glazer, E. C., Light-sensitive ruthenium complex-loaded cross-linked polymeric nanoassemblies for the treatment of cancer. *Journal of Materials Chemistry B* **2016,** *4* (3), 394-408.

[86] Fischer, B.; Heffeter, P.; Kryeziu, K.; Gille, L.; Meier, S. M.; Berger, W.; Kowol, C. R.; Keppler, B. K., Poly (lactic acid) nanoparticles of the lead anticancer ruthenium compound KP1019 and its surfactant-mediated activation. *Dalton Transactions* **2014,** *43* (3), 1096-1104.

[87] Yoo, J.; Won, Y.-Y., Phenomenology of the initial burst release of drugs from PLGA Microparticles. *ACS Biomaterials Science & Engineering* **2020,** *6* (11), 6053-6062.

[88] Zhou, H.; Chen, M.; Liu, Y.; Wu, S., Stimuli‐Responsive Ruthenium‐Containing Polymers. *Macromolecular rapid communications* **2018,** *39* (22), 1800372.

[89] Chen, M.; Sun, W.; Kretzschmann, A.; Butt, H.-J.; Wu, S., Nanostructured polymer assemblies stabilize photoactivatable anticancer ruthenium complexes under physiological conditions. *Journal of inorganic biochemistry* **2020,** *207*, 111052.

[90] Xie, C.; Sun, W.; Lu, H.; Kretzschmann, A.; Liu, J.; Wagner, M.; Butt, H.-J.; Deng, X.; Wu, S., Reconfiguring surface functions using visible-light-controlled metal-ligand coordination. *Nature communications* **2018,** *9* (1), 1-9.

[91] Liu, J.; Xie, C.; Kretzschmann, A.; Koynov, K.; Butt, H. J.; Wu, S., Metallopolymer Organohydrogels with Photo‐Controlled Coordination Crosslinks Work Properly Below 0° C. *Advanced Materials* **2020,** *32* (14), 1908324.

[92] Sun, W.; Parowatkin, M.; Steffen, W.; Butt, H. J.; Mailänder, V.; Wu, S., Ruthenium‐containing block copolymer assemblies: red‐light‐responsive metallopolymers with tunable nanostructures for enhanced cellular uptake and anticancer phototherapy. *Advanced healthcare materials* **2016,** *5* (4), 467-473.

[93] Sun, W.; Li, S.; Häupler, B.; Liu, J.; Jin, S.; Steffen, W.; Schubert, U. S.; Butt, H. J.; Liang, X. J.; Wu, S., An amphiphilic ruthenium polymetallodrug for combined photodynamic therapy and photochemotherapy in vivo. *Advanced Materials* **2017,** *29* (6), 1603702.

[94] Chakrabortty, S.; Agrawalla, B. K.; Stumper, A.; Vegi, N. M.; Fischer, S.; Reichardt, C.; Kögler, M.; Dietzek, B.; Feuring-Buske, M.; Buske, C., Mitochondria targeted protein-ruthenium photosensitizer for efficient photodynamic applications. *Journal of the American Chemical Society* **2017,** *139* (6), 2512-2519.

Chapter 2: Red-light-induced simultaneous dePEGylation, morphology transition, and zeta potential increase using amphiphilic metallodrug assemblies: improved tumor penetration and cellular internalization for efficient anticancer phototherapy

Xiaolong Zeng, Yufei Wang, Yun-Shuai Huang, Jianxiong Han, Wen Sun, Hans-Jürgen Butt, Xing-Jie Liang, and Si Wu**

X. Zeng, J. Han, Yun-Shuai Huang, Prof. S. Wu

CAS Key Laboratory of Soft Matter Chemistry

Hefei National Laboratory for Physical Sciences at the Microscale

Department of Polymer Science and Engineering

University of Science and Technology of China

Hefei 230026, China

E-mail: siwu@ustc.edu.cn

Y. Wang, Prof. X.-J. Liang

Chinese Academy of Sciences (CAS) Key Laboratory for Biomedical Effects of Nanomaterials and Nanosafety

CAS Center for Excellence in Nanoscience

National Center for Nanoscience and Technology

Beijing 100190, China

E-mail: liangxj@nanoctr.cn

Y. Wang, Prof. X.-J. Liang

University of Chinese Academy of Sciences

Beijing 100049, China

X. Zeng, J. Han, Prof. H.-J. Butt, Prof. S. Wu

Max Planck Institute for Polymer Research

Ackermannweg 10, 55128 Mainz, Germany

Prof. Dr. W. Sun

State Key Laboratory of Fine Chemicals

Dalian University of Technology

2 Linggong Road, Hi-Tech Zone, Dalian 116024, China

Keywords: metallodrugs, photo-cleavable, morphology transition, tumor penetration, zeta potential

The work in this chapter is based on the manuscript ‘Red-light-induced simultaneous dePEGylation, morphology transition, and zeta potential increase using amphiphilic metallodrug assemblies: improved tumor penetration and cellular internalization for efficient anticancer phototherapy’ which has been in preparation for submission.

2.1 Statement of contribution

Si Wu, Xing-Jie Liang and Hans-Jürgen Butt led the project.

Xiaolong Zeng prepared the materials and did the synthesis.

Xiaolong Zeng and Yufei Wang did the biological experiments.

Yun-Shuai Huang contributed to the NMR analysis.

Jianxiong Han contributed to TEM measurement.

Wen Sun contributed to ESI-MS measurement.

Xiaolong Zeng and Yufei Wang contributed equally to this work.

2.2 Introduction

Metallodrugs, such as platinum (Pt) complexes, have been widely used to treat cancer.[1] Recently, ruthenium (Ru) complexes have emerged as next-generation anticancer agents.[2] In particular, photoresponsive Ru complexes are of interest in phototherapy.[3] These complexes are generally nontoxic in dark but become toxic at irradiated sites. Photoactivation of these complexes only at tumor sites can improve the therapeutic selectivity.[4] Delivering photoresponsive Ru towards tumor is crucial in phototherapy.[5]

Modification of Ru complexes with polyethylene glycol (PEGylation) can prolong blood circulation and enable tumor accumulation.[5, 6] However, PEGylation suffers limitations.[7, 8] For example, PEGylation typically increases the size of Ru complexes, which hinder the tumor penetration.[7] PEGylation also neutralizes zeta potential of Ru complexes, which is antagonistic to cellular internalization.[7] To address these issues, removal of polyethylene glycol (dePEGylation) may be adopted at the tumor region.[9, 10] Furthermore, stimuli-responsive transition of size and zeta potential can be also taken into consideration.[11, 12] Decreasing size promotes deeper tumor penetration.[13, 14] Increasing zeta potential facilitates efficient cellular internalization.[15, 16] All of them are beneficial to deliver Ru complexes towards cancer cells.[17]

Photoactivation of Ru complexes in intracellular environment causes apoptosis of cancer cells.[18] However, photoresponsive Ru complexes are typically non-fluorescent, which cannot be visualized in cancer cells.[6, 19] The non-visualization may hinder the exploration of mechanisms of these complexes.[2] Thus, the anticancer mechanisms of actions of photoresponsive Ru complexes still possess challenges.

Herein, a fluorescent Ru complex (Ru-PEG), with the properties of light-induced dePEGylation and size decrement as well as zeta potential increment, is reported. Ru-PEG is an amphiphilic compound. A hydrophobic Ru(II) moiety was covalently linked to a fluorescent pyrene moiety. A hydrophilic pyridine-containing PEG ligand was coordinated to Ru center.

The hydrophobic Ru moiety was toxic because some Ru complexes showed anticancer activities.[20-22] The hydrophilic PEG moiety was biocompatible because it prolongs blood circulation and suppress nonspecific adsorption of proteins.[23] Ru-PEG self-assembled into vesicles, which accumulated at tumor sites via EPR effect. Irradiation of Ru-PEG induced the release of PEG, underwent morphology transition to form Ru-H2O large compound micelles (LCMs). These LCMs had smaller size, which lead to a deeper tumor penetration. Ru-H2O LCMs also hold higher zeta potential, which is beneficial to cellular internalization. Photo-induced the PEG release, the transition to small size LCMs, as well as the increment of zeta potential, made a combination effect to deliver toxic Ru towards cancer cells (**Figure 1**). Irradiation of Ru-PEG with red light generated $^1O_2$ for photodynamic therapy. Moreover, with the conjugation of fluorescent pyrene, Ru-PEG simultaneously served as imaging agents for spatiotemporal visualization. We found that Ru-PEG colocalized with lysosome, which further cause the release of cathepsin B under irradiation, to induce apoptosis. The fluorescent visualization of Ru-PEG helped us to better understand the anticancer mechanisms of action in intracellular environment.

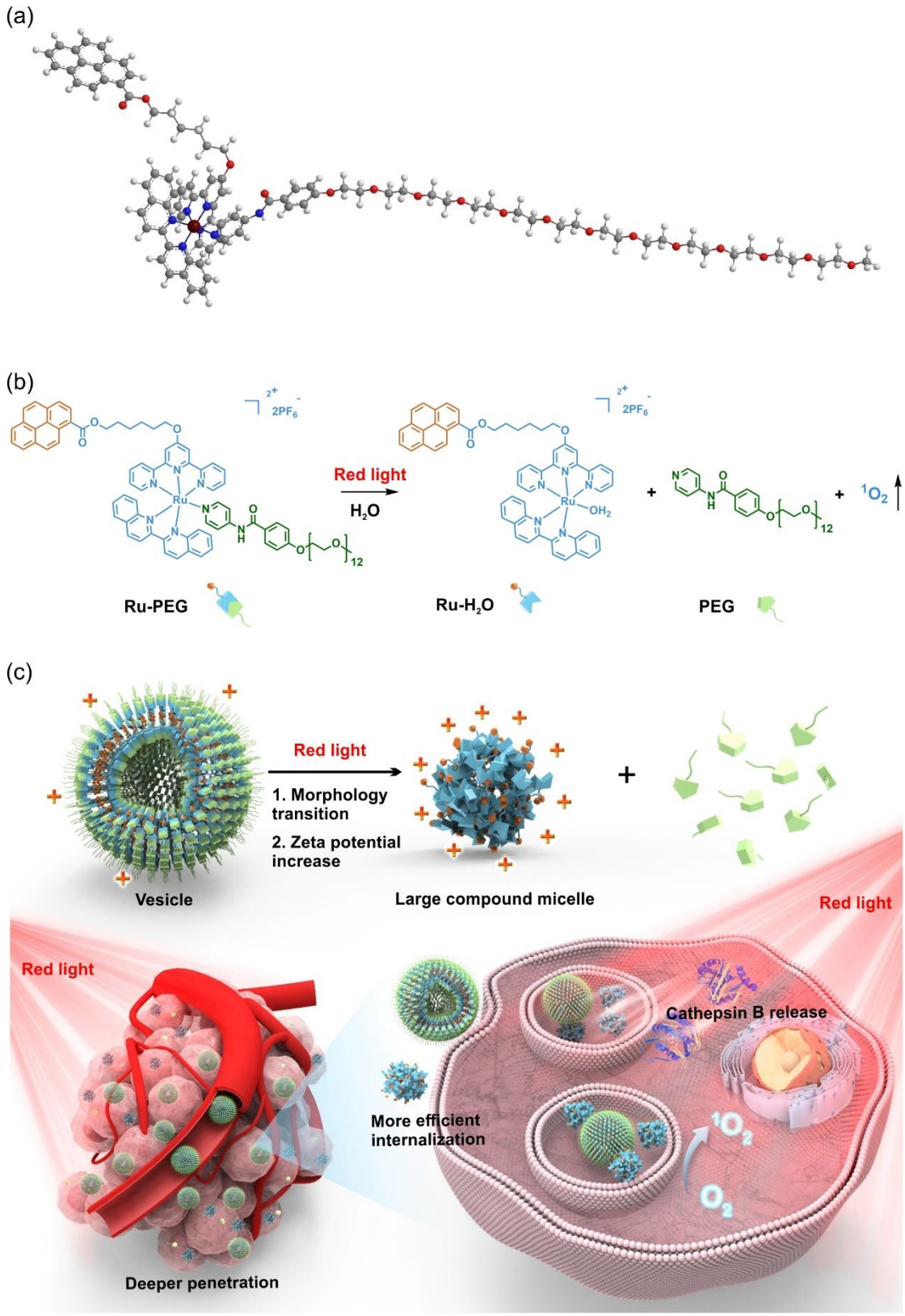

Figure 1. (a) Molecular dynamics simulation of Ru-PEG molecule. (b) Chemical structure and photoreaction of the amphiphilic Ru-PEG. Red light irradiation induced the release of the anticancer agent Ru-H_2O and the generation of $^1O_2$. (c) Self-assembly of Ru-PEG, its morphology transition and zeta potential increment upon red light irradiation, for deeper penetration and more efficient internalization.

2.3 Results and discussion

2.3.1 Synthesis of Ru-PEG

To prepare Ru-PEG, we first synthesized the pyridine-containing ligand PEG (Figure S1) and ruthenium (Ru) aquar complex Ru-H_2O (Figure S2) via multi-step routes. All intermediates were fully characterized using nuclear magnetic resonance (NMR) spectroscopy (Figure S5-11). Afterwards, the pyridine-containing ligand was coordinated with the Ru-H_2O via complexation (Figure S3). NMR spectroscopy and mass spectrometry (MS) demonstrated that Ru-PEG was successfully synthesized (Figure S12-S14).

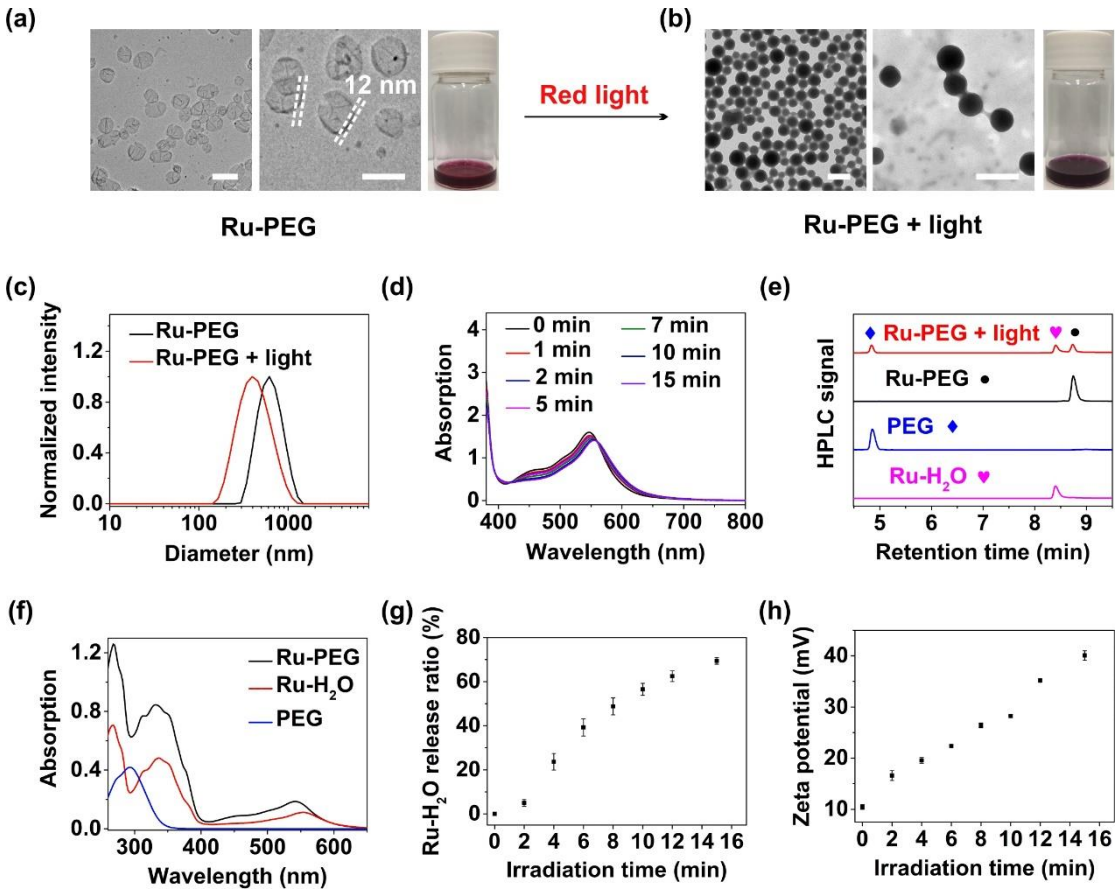

Figure 2. TEM images of Ru-PEG vesicles before (a) and after (b) light irradiation. Scale bar: 500 nm. (c) The diameter of Ru-PEG vesicles before and after light irradiation measured by dynamic light scattering (DLS). (d) UV-vis absorption spectra of Ru-PEG vesicles upon red light irradiation (25 mW cm^{-2}, 15 min) over time. (e) Photosubstitution of Ru-PEG studied by high-performance liquid chromatography (HPLC). The black dots (●) reflect Ru-PEG, the magenta heart shape (♥) reflect the released Ru-H_2O, and the blue diamond (♦) reflect the released PEG. Ru-PEG was irradiated using 656 nm light (25 mW cm-^{2}, 15 min). (f) UV-vis spectrum in HPLC system to assign the peaks in Figure 2e. (g) The release ratio of Ru-H_2O

from Ru-PEG vesicles under red light irradiation (25 mW cm^{-2}, 15 min). The release ratio is the actual release molar of Ru-H_2O divided by the theoretical molar of Ru-H_2O. (h) Zeta potential of Ru-PEG vesicles upon light irradiation (25 mW cm^{-2}, 15 min).

2.3.2 Self-assembly of Ru-PEG

We then prepared Ru-PEG nanostructure via self-assembly. Ru-PEG was dissolved in THF. Water was added dropwise to the solution to trigger self-assembly. Subsequently, Ru-PEG in an aqueous solution were obtained by removing THF via dialysis against water. Transmission electron microscopy (TEM) showed that Ru-PEG self-assembled into vesicles with an average diameter of 440 nm (**Figure 2a**). The wall thickness of these vesicles was ~12 nm, which was consistent with twice of the molecular length (Figure S18-S19). Dynamic light scattering (DLS) showed that Ru-PEG vesicles had an average hydrodynamic diameter of 520 nm (Figure 2c), which was comparable to the TEM observations. Moreover, Ru-PEG vesicles in aqueous solution were stable for 36 h in the dark (Figure S20). To investigate the mechanism of self-assembly, a Ru complex without the pyrene moiety (Ru2-PEG) was synthesized (Figure S4 and S15-S17). Ru2-PEG cannot form any defined nanostructures (Figure S22). These results demonstrated that linking with pyrene moiety contributed to the self-assembly via π-π stacking and hydrophobic effect (Figure S23).

2.3.3 Light-cleavable Ru-PEG and transformable properties

Ru-PEG are photoresponsive, which makes these vesicles morphology transformable. We then studied the morphology transition of Ru-PEG vesicles induced by red light irradiation (Figure 2b). These vesicles changed to large compound micelles (LCMs) after light irradiation, which was consistent with the self-assembled Ru-H_2O (Figure S21a and S21b). DLS showed that these LCMs had smaller size with diameter of 290 nm (Figure 2c). We also performed UV-vis absorption spectroscopy, to study the photoreaction of Ru-PEG vesicles (Figure 2d). Light

irradiation of Ru-PEG red-shifted the metal-to-ligand charge transfer (MLCT) band from 542 nm (λ_{max} of Ru-PEG) to 558 nm (λ_{max} of Ru-H_2O). The spectrum showed obvious change within 15 min, suggesting the efficient photosubstitution of Ru-PEG.

The TEM, DLS and UV-vis results demonstrated the qualitative photosubstitution of Ru-PEG. High-performance liquid chromatography (HPLC) was then performed to quantify the photosubstitution (Figure 2e). Ru-PEG is represented by only one signal. After 656 nm light irradiation (30 mW cm^{-2}, 15 min), two new peaks, the photoproducts, appeared. Comparing the retention time of photoproducts with that of pure PEG and Ru-H_2O, it confirmed that the new two peaks were assigned to PEG and Ru-H_2O, respectively. This was further demonstrated by UV-vis absorption spectroscopy detector in the HPLC system (Figure 2f). The integration ratio of PEG, Ru-H_2O and residual Ru-PEG was 30%, 32% and 38%, respectively. These results showed that light can induce the release of Ru-H_2O and PEG efficiently.

The released behavior of Ru-H_2O was further investigated by HPLC (Figure 2g and Figure S24). Up to 40% of Ru-H_2O was released at first 6 min irradiation. The released percentage achieved 70% when the irradiation time was prolonged to 15 min, indicating the efficient release profile of Ru-H_2O.

Light-induced the release of PEG also led to zeta potential increase (Figure 2h). Before irradiation, the zeta potential of Ru-PEG vesicles was +11 mV. Zeta potential gradually increased to +41 mV when the irradiation time was prolonged to 15 min. This was due to the released PEG, leading to the exposure of Ru-H_2O. Ru-H_2O had higher zeta potential (Figure S21c), which enhanced the zeta potential in solution.

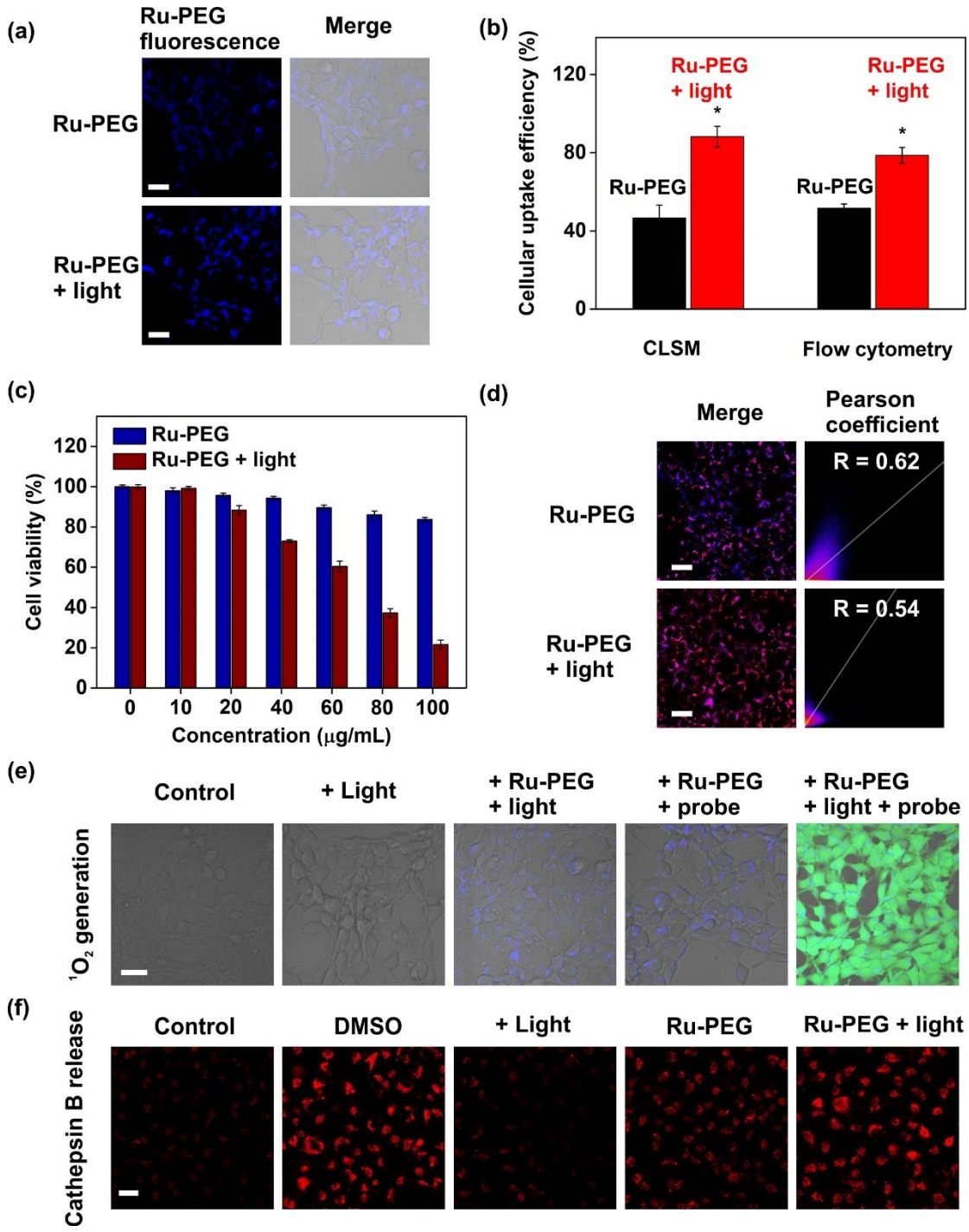

Figure 3. (a) Confocal laser scanning microscopy (CLSM) images of Ru-PEG vesicles and Ru-PEG vesicles after light irradiation, followed by incubation with 4T1 cancer cells for 2 h. Ru-PEG vesicles and Ru-PEG after irradiation were excited with a 405 nm laser (blue). Scale bars: 25 μm. (b) Cellular uptake against 4T1 cells when treated with Ru-PEG vesicles and Ru-PEG vesicles after light irradiation. Quantifications were calculated using imageJ software from CLSM images and flow cytometry. (c) Viability of 4T1 cancer cells treated with various concentration of Ru-PEG vesicles in the dark and under light irradiation. The cells were irradiated with 671 nm red light (25 mW cm^{-2}, 15 min) after incubation with Ru-PEG for 2 h. Cell viability was tested after the cells were further incubated in the dark for 24 h. (d) Confocal colocalization images and Pearson's colocalization coefficients (R) of Ru-PEG vesicles

incubated with 4T1 cells before and after irradiation. Ru-PEG vesicles were excited with a 405 nm laser (blue). Lysosome was labelled using LysoTracker deep red and excited at 633 nm (red). Scale bars: 50 μm. (e) Generation of intracellular $^1O_2$ in 4T1 cells observed by CLSM. $^1O_2$ was detected using the indicator DCFH-DA (green). Scale bars: 50 μm. (f) CLSM images of cathepsin B released from lysosomes to the cytosol induced under different conditions. DMSO was set as a positive control. Cathepsin B was labelled with Magic Red and excited at 633 nm (red). Scale bars: 50 μm.

2.3.4 Cellular uptake and in vitro cytotoxicity assessment

Ru complexes showed anticancer performances against cancer cells. Thus, we used Ru-PEG to deliver Ru towards 4T1 cells. We first investigated the cellular uptake against 4T1 cells (**Figure 3a**). 4T1 cells were incubated with Ru-PEG vesicles for 2 h in the dark. Subsequently, confocal laser scanning microscopy (CLSM) images were taken to observe the pyrene fluorescence, which was excited from Ru-PEG vesicles. The observation of blue fluorescence suggested that Ru-PEG vesicles can be taken up by 4T1 cells. After light irradiation, we further found that 4T1 cells can take up Ru-PEG more efficiently (Figure 3a). This was due to the photo-induced dePEGylation, leading to the morphology transition as well as the increment of zeta potential. All of them were beneficial for cellular internalization. As a comparison, Ru-H_2O LCMs was directly incubated with cells to demonstrate this observation (Figure S25). Moreover, we used ImageJ software to quantify the fluorescence intensity from CLSM images. The intensities for Ru-PEG and Ru-PEG after irradiation were 44% and 88%, respectively. Flow cytometry was also applied to quantify the cellular uptake. The uptake efficiency for Ru-PEG and Ru-PEG after irradiation were 48% and 79%, which was consistent with the results analyzed by ImageJ software (Figure 3b). These results demonstrated that photo-induced dePEGylation, morphology transition, as well as the increment of zeta potential contributed a higher cellular uptake efficiency.

Ru-PEG can generate $^1O_2$ under light irradiation. We applied 2,7-dichlorofluorescein diacetate (DCFH-DA) to detect the intracellular 1O2 production under light irradiation. DCFH-

DA is not fluorescent, but can be green fluorescent in the presence of $^1O_2$. Green fluorescence was observed when 4T1 cells irradiated with Ru-PEG in combination with the probe (Figure 3e). This observation indicated that irradiation of Ru-PEG in intracellular environment can generate $^1O_2$ for photodynamic therapy (PDT).

We then studied the colocalization of Ru-PEG with lysosome because lysosome is an effective target during PDT process (Figure 3d). Lysosome was stained using LysoTracker dyes. The blue fluorescence was from Ru-PEG. CLSM images showed that before light irradiation, the blue fluorescence preferably overlapped with the red emission in lysosome, with a colocalization coefficient up to 0.62. After light irradiation, the colocalization coefficient negligibly decreased to 0.54. Only partial Ru-PEG was observed to escape from lysosome (Figure S26). These results indicated that Ru-PEG mainly selectively localized in the lysosomes even after irradiation.

The efficient cellular uptake and lysosome localization encouraged us to evaluate the therapeutic effects of PDT of Ru-PEG. The anticancer performances of Ru-PEG against 4T1 cells were first investigated (Figure 3c). In the dark, the cell viability had negligible influence when incubating with Ru-PEG. However, after light irradiation, when the concentration of Ru-PEG was up to 100 μg/mL, the cell viability decreased to 21% against 4T1 cells. We infer that the decrement of cell viability occurred because of the generation of $^1O_2$ during PDT process. The generation of $^1O_2$ in lysosome result in lysosomal permeability via massive peroxidation of membrane lipids. The disruption of lysosome further caused the release of lysosomal proteases, such as cathepsin B, into cytoplasm. The released cathepsin B may cause apoptosis of cancer cells. Therefore, we applied a fluorescent magic red dye against 4T1 cells, to detect the release of cathepsin B caused by $^1O_2$ (Figure 3f). The control group display red dot-like fluorescence which located in lysosome. After incubating with Ru-PEG, and followed by light irradiation, the red fluorescence diffused from lysosome to cytosol. This was also observed in

the positive group, in which cells were treated with DMSO. These results demonstrated that cathepsin B was released from lysosome into cytosol after $^1O_2$-induced lysosomal damage, which further cause the apoptosis of 4T1 cells.

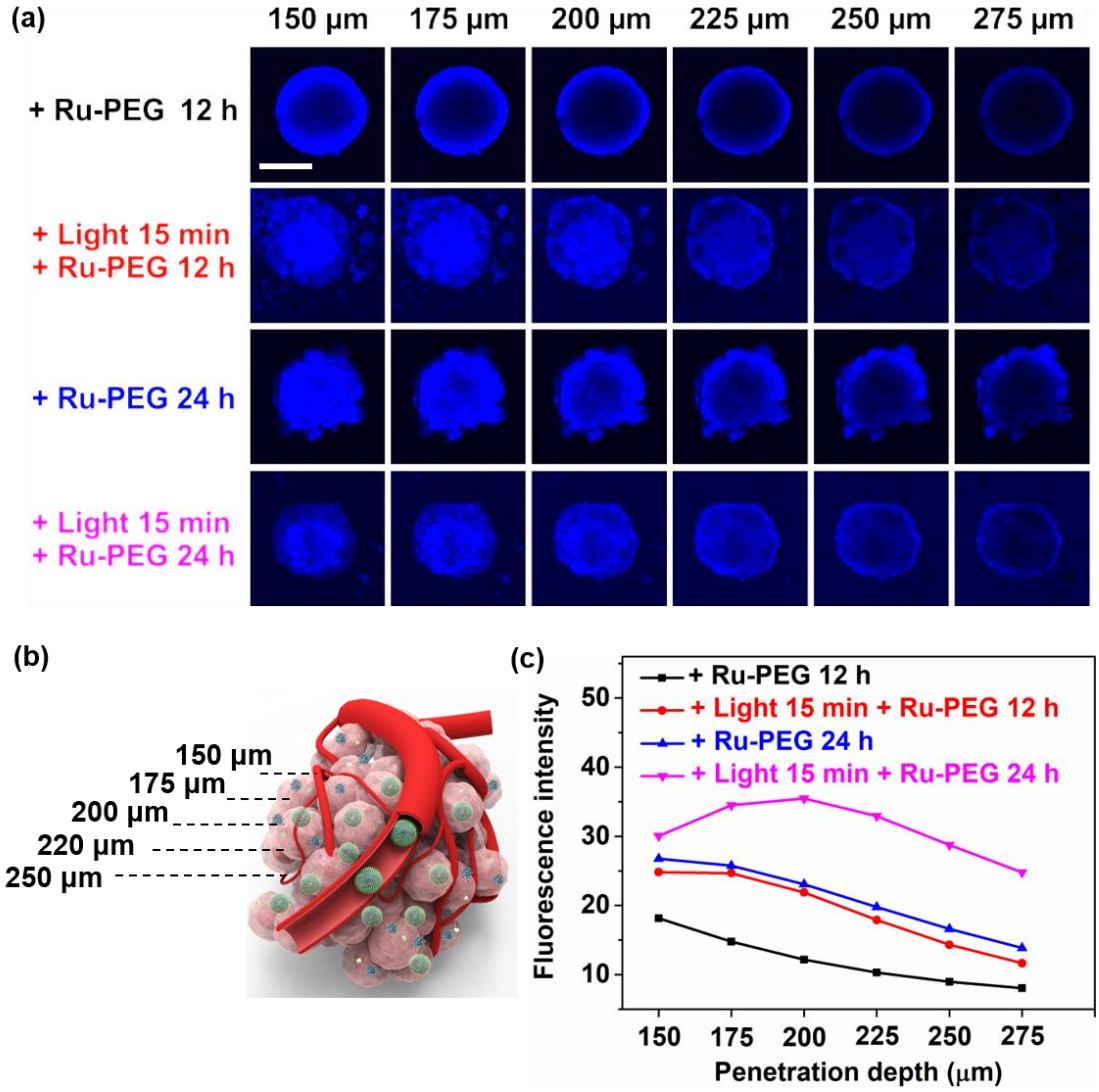

Figure 4. (a) CLSM images of Ru-PEG and Ru-PEG after light irradiation, followed by incubating with 4T1 multicellular tumor spheroids (MTSs) for 12, 24 h. Ru-PEG was excited at 405 nm. Scale bar = 200 μm. (b) Illustration of the MTSs that were visualized using CLSM in Z-stacks with 25 μm intervals. (c) Average fluorescence intensity at different penetration depth calculated by ImageJ software.

2.3.5 Tumor penetration ability of Ru-PEG

To further study the tumor penetration ability, we applied Ru-PEG vesicles in a 4T1 multicellular tumor spheroids (MTSs) model (**Figure 4a**). CLSM was performed using Z-stack at 25 μm intervals from apex to equator (Figure 4b). After incubating with Ru-PEG for 12 h, the fluorescence was only detected around the periphery of MTS but not the interior. When the incubating time was up to 24 h, the penetration depth gradually increased. However, irradiation of Ru-PEG for 15 min and further incubated with MTSs for 24 h, the blue fluorescence was observed throughout the spheroids and reach into the interior. We infer that the morphology transition of Ru-PEG, from larger vesicles to smaller LCMs, contributed the deeper penetration depth. As a comparison, Ru-H_2O LCMs were directly incubated with MTSs (Figure S27). We found that Ru-H_2O LCMs also located in the center of the spheroids and distributed throughout the whole spheroids. This was consistent with Ru-PEG after light irradiation. The average fluorescence intensities of each observed layer were calculated using ImageJ software (Figure 4c). Irradiation of Ru-PEG and further incubation for 24 h showed the highest fluorescence intensity. These results indicated that light-induced dePEGylation as well as morphology transition led to a deeper penetration depth of Ru-PEG vesicles.

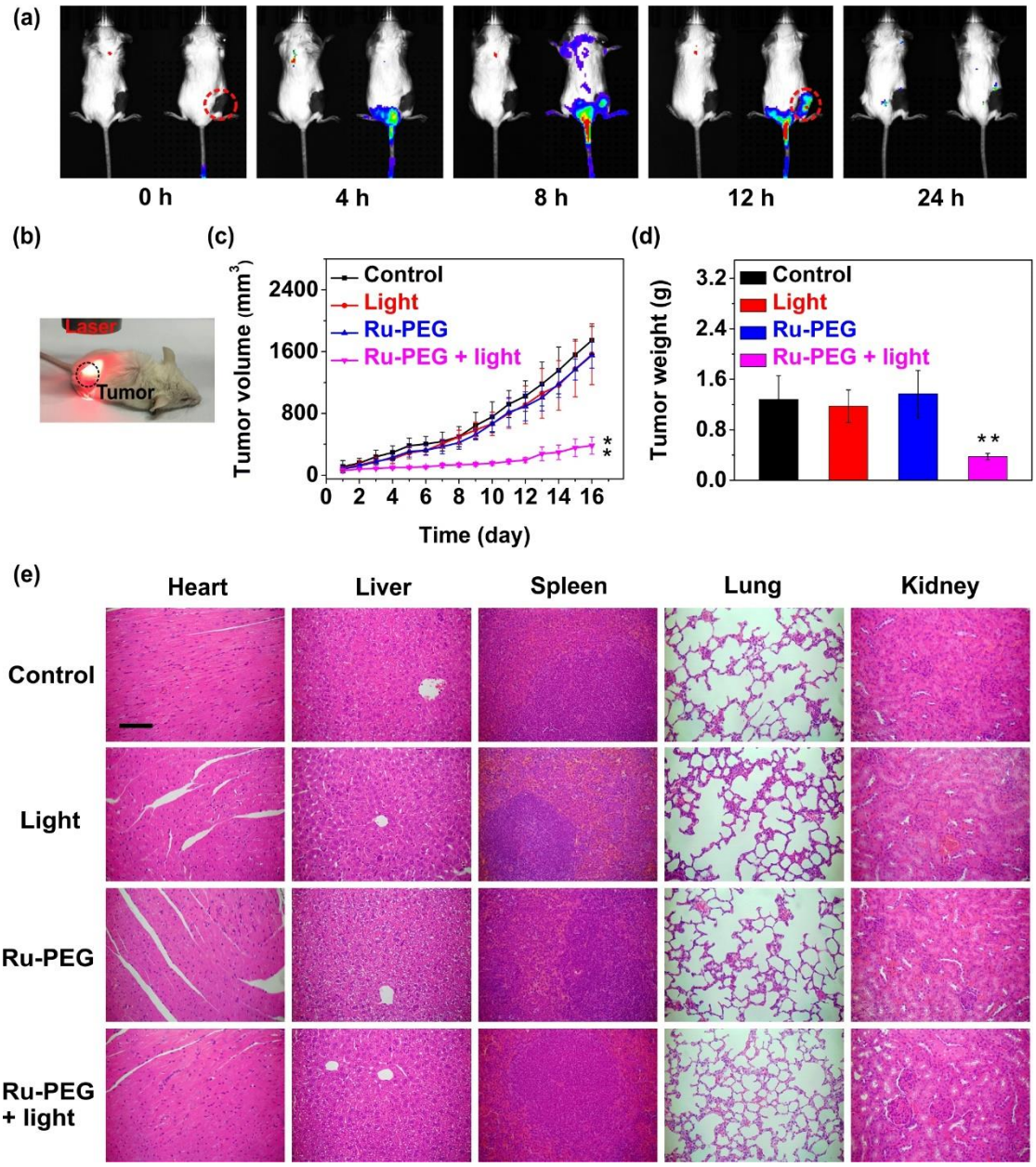

Figure 5. (a) Fluorescence images of 4T1 tumor-bearing mice after intravenous injection of saline (left, control) and Ru-PEG vesicles (right). Images were taken after injection for 0, 4, 8, 12 and 24 h. The dashed circle indicates the tumor. (b) A photograph shows red light irradiation on a mouse model. (c) Tumor volumes of 4T1 tumor-bearing mice during different treatments. (d) Average tumor weights at day 16 after different treatments. (e) Histopathological analysis by H&E staining of tissue sections isolated from 4T1 tumor-bearing mice. Scale bar: 100 μm.

2.3.6 In vivo anticancer assessment

Inspired by the anticancer performance of Ru-PEG in vitro, we further studied the anticancer effect of Ru-PEG in vivo. Hemolysis analysis indicated that Ru-PEG have good blood

compatibility (Figure S28). We then investigated the anticancer performance of Ru-PEG using a 4T1 tumor-bearing mouse model.

Ru-PEG accumulated at tumor sites when administered intravenously (Figure 5a). Fluorescence images of the mouse model (right) and a control mouse (left) were taken over time after injection. No fluorescence signal was observed at tumor site at first 4 h. A weak fluorescence appeared after 8 h post-injection. However, the fluorescence at tumor site reached a maximum intensity at 12 h, which indicated that Ru-PEG efficiently accumulated at the tumor site. The fluorescence intensity disappeared after 24 h, suggesting the vesicles were cleared through metabolism. In contrast, the control mouse injected with saline showed no fluorescence, which proved that the fluorescence was produced by the injected Ru-PEG vesicles. These results demonstrated that Ru-PEG vesicles accumulate at the tumor site, probably due to the EPR effect.

Twelve hours after Ru-PEG vesicles were injected into the mouse model, the tumor was irradiated with a 671 nm laser for 15 min (Ru-PEG + light group) (Figure 5b). Three additional experiments were conducted for comparison: 1) 4T1 tumor-bearing mice were injected with saline (Control Group); 2) 4T1 tumor-bearing mice were irradiated with light (Light Group); and 3) 4T1 tumor-bearing mice were injected with Ru-PEG (Ru-PEG Group). We compared the anticancer efficacy by monitoring the tumor volumes of each group over 16 days (Figure 5c). The tumor volume in the control group increased by ~17 times. The result of the light group was similar to that of the control group, indicating that mild light irradiation does not have an inhibitory effect (Figure S29). Ru-PEG treatment caused a negligible tumor inhibition, because no photo-generated $^1O_2$ was conducted. Compared to the three groups mentioned above, tumor growth in the Ru-PEG + light group was notably inhibited. This result suggested that the generated $^1O_2$ achieved good anticancer performance.

Subsequently, the mice were euthanized, and the tumors were isolated for analysis. The average tumor weight in the Ru-PEG + light group was much lighter than that in the other three groups (Figure 5d). Immunohistochemical analysis of isolated tumors were also performed to illustrate the mechanism of the anticancer activity using Ru-PEG vesicles (Figure S30). A hematoxylin and eosin (H&E) staining assay showed large areas of apoptosis and necrosis, which suggested that the Ru-PEG + light group treatment exhibited considerable tumor inhibition. Similar results were observed in TUNEL staining images. In addition, Ki67 staining assay offered additional evidence for the anticancer mechanism. Ki67 is a sensitive marker for cell proliferation. Comparing the fluorescence of Ki67 at tumor sites, we found that sparse fluorescence area in the Ru-PEG + light group. We hypothesized that the generated $^1O_2$ induced DNA damage, which increased genomic instability and apoptosis. This caused the decrement of Ki67 protein marker.

We also investigated the systemic toxicity during the treatments by comparing the H&E staining images of the main organs (heart, liver, lung, spleen, and kidney) (Figure 5e). Negligible pathological alteration of the organs was observed, indicating the low systemic toxicity of Ru-PEG. The body weights of the mice did not change significantly during the treatments (Figure S31), which suggests that the treatments had minimal side effects. These combined results demonstrate that the use of Ru-PEG can treat 4T1 tumors with improved selectivity and minimized systemic toxicity.

2.4 Conclusions

In conclusion, we synthesized a photo-responsive Ru-PEG vesicles with transformable properties for solid tumor treatment. Due to the design of the molecular structure, Ru-PEG exhibited morphology transition as well as zeta potential increment upon light irradiation. Outstanding anticancer performance both in vitro and in vivo were achieved using Ru-PEG

during the cellular internalization and tumor penetration process. Our study revealed that the favorable design of metallodrugs with transformable properties is a new strategy to enhance the anticancer efficacy. We believe that more multi-functional metallodrugs with transformable properties can be developed for effective cancer therapy in both research and clinic.

2.5 References

[1] T.C. Johnstone, K. Suntharalingam, S.J. Lippard, The next generation of platinum drugs: targeted Pt (II) agents, nanoparticle delivery, and Pt (IV) prodrugs, Chemical reviews 116(5) (**2016**) 3436-3486.

[2] L. Zeng, P. Gupta, Y. Chen, E. Wang, L. Ji, H. Chao, Z.S. Chen, The development of anticancer ruthenium(ii) complexes: from single molecule compounds to nanomaterials, Chem Soc Rev 46(19) (**2017**) 5771-5804.

[3] C. Mari, V. Pierroz, S. Ferrari, G. Gasser, Combination of Ru(ii) complexes and light: new frontiers in cancer therapy, Chem Sci 6(5) (**2015**) 2660-2686.

[4] S. Bonnet, Why develop photoactivated chemotherapy?, Dalton Transactions 47(31) (**2018**) 10330-10343.

[5] E. Villemin, Y.C. Ong, C.M. Thomas, G. Gasser, Polymer encapsulation of ruthenium complexes for biological and medicinal applications, Nature Reviews Chemistry 3(4) (**2019**) 261-282.

[6] W. Sun, S. Li, B. Häupler, J. Liu, S. Jin, W. Steffen, U.S. Schubert, H.J. Butt, X.J. Liang, S. Wu, An amphiphilic ruthenium polymetallodrug for combined photodynamic therapy and photochemotherapy in vivo, Advanced Materials 29(6) (**2017**) 1603702.

[7] J.M. Harris, R.B. Chess, Effect of pegylation on pharmaceuticals, Nature reviews Drug discovery 2(3) (**2003**) 214-221.

[8] L. Shi, J. Zhang, M. Zhao, S. Tang, X. Cheng, W. Zhang, W. Li, X. Liu, H. Peng, Q. Wang, Effects of polyethylene glycol on the surface of nanoparticles for targeted drug delivery, Nanoscale (**2021**).

[9] M. Zhou, H. Huang, D. Wang, H. Lu, J. Chen, Z. Chai, S.Q. Yao, Y. Hu, Light-triggered PEGylation/dePEGylation of the nanocarriers for enhanced tumor penetration, Nano letters 19(6) (**2019**) 3671-3675.

[10] L. Kong, F. Campbell, A. Kros, DePEGylation strategies to increase cancer nanomedicine efficacy, Nanoscale horizons 4(2) (**2019**) 378-387.

[11] N. Jia, W. Li, D. Liu, S. Wu, B. Song, J. Ma, D. Chen, H. Hu, Tumor microenvironment stimuli-responsive nanoparticles for programmed anticancer drug delivery, Molecular pharmaceutics 17(5) (**2020**) 1516-1526.

[12] J.-Z. Du, H.-J. Li, J. Wang, Tumor-acidity-cleavable maleic acid amide (TACMAA): a powerful tool for designing smart nanoparticles to overcome delivery barriers in cancer nanomedicine, Accounts of chemical research 51(11) (**2018**) 2848-2856.

[13] H. Cabral, Y. Matsumoto, K. Mizuno, Q. Chen, M. Murakami, M. Kimura, Y. Terada, M. Kano, K. Miyazono, M. Uesaka, Accumulation of sub-100 nm polymeric micelles in poorly permeable tumours depends on size, Nature nanotechnology 6(12) (**2011**) 815-823.

[14] C. Wong, T. Stylianopoulos, J. Cui, J. Martin, V.P. Chauhan, W. Jiang, Z. Popović, R.K. Jain, M.G. Bawendi, D. Fukumura, Multistage nanoparticle delivery system for deep penetration into tumor tissue, Proceedings of the National Academy of Sciences 108(6) (**2011**) 2426-2431.

[15] Z.-G. Yue, W. Wei, P.-P. Lv, H. Yue, L.-Y. Wang, Z.-G. Su, G.-H. Ma, Surface charge affects cellular uptake and intracellular trafficking of chitosan-based nanoparticles, Biomacromolecules 12(7) (**2011**) 2440-2446.

[16] Y.Y. Yuan, C.Q. Mao, X.J. Du, J.Z. Du, F. Wang, J. Wang, Surface charge switchable nanoparticles based on zwitterionic polymer for enhanced drug delivery to tumor, Advanced materials 24(40) (**2012**) 5476-5480.

[17] Q. Sun, Z. Zhou, N. Qiu, Y. Shen, Rational design of cancer nanomedicine: nanoproperty integration and synchronization, Advanced Materials 29(14) (**2017**) 1606628.

[18] W. Sun, R. Thiramanas, L.D. Slep, X. Zeng, V. Mailänder, S. Wu, Photoactivation of anticancer Ru complexes in deep tissue: How deep can we go, Chem. Eur. J 23 (**2017**) 10832-10837.

[19] W. Sun, Y. Wen, R. Thiramanas, M. Chen, J. Han, N. Gong, M. Wagner, S. Jiang, M.S. Meijer, S. Bonnet, Red‐Light‐Controlled Release of Drug–Ru Complex Conjugates from Metallopolymer Micelles for Phototherapy in Hypoxic Tumor Environments, Advanced Functional Materials 28(39) (**2018**) 1804227.

[20] L.N. Lameijer, D. Ernst, S.L. Hopkins, M.S. Meijer, S.H. Askes, S.E. Le Dévédec, S. Bonnet, A red‐light‐activated ruthenium‐caged NAMPT inhibitor remains phototoxic in hypoxic cancer cells, Angewandte Chemie 129(38) (**2017**) 11707-11711.

[21] V. Van Rixel, B. Siewert, S. Hopkins, S. Askes, A. Busemann, M. Siegler, S. Bonnet, Green light-induced apoptosis in cancer cells by a tetrapyridyl ruthenium prodrug offering two trans coordination sites, Chemical science 7(8) (**2016**) 4922-4929.

[22] K. Arora, M. Herroon, M.H. Al-Afyouni, N.P. Toupin, T.N. Rohrabaugh Jr, L.M. Loftus, I. Podgorski, C. Turro, J.J. Kodanko, Catch and release photosensitizers: combining dual-action ruthenium complexes with protease inactivation for targeting invasive cancers, Journal of the American Chemical Society 140(43) (**2018**) 14367-14380.

[23] R. Michel, S. Pasche, M. Textor, D.G. Castner, Influence of PEG architecture on protein adsorption and conformation, Langmuir 21(26) (**2005**) 12327-12332.

2.6 Supporting information

Materials

RuCl3•xH2O (99.9%), 2,2’-biquinoline (98%), silver hexafluorophosphate (98%), potassium hexafluorophosphate (99%), p-toluolsulfonylchlorid (99%), 1-pyrenecarboxylic acid (97%), methyl 4-hydroxybenzoate (99%), 4-aminopyridine (98%), potassium carbonate (99%), potassium tert-butoxide (98%), and methoxy-PEG12-hydroxyl (95%) were purchased from Sigma-Aldrich. 1,6-Dihydroxyhexane (99%), N,N’-dicyclohexylcarbodiimide (DCC) (99%), and triethylamine (99%) were purchased from Alfa Aesar. THF (technical grade, stabilizer free) was purchased from Acros Organics. 4'-Chloro-2,2',6',2"-terpyridine (>98%) was purchased from AEchem Scientific Corporation. 1,1’-Dioctadecyl-3,3,3’,3’-tetramethylindodicarbocyanine, 4-chlorobenzenesulfonate salt (DiD fluorescent dye) and LysoTracker™ deep red were purchased form Thermo Fisher Scientific. 2,7-dichlorofluorescein diacetate (DCFH-DA) and Magic Red dye were purchased form Solarbio, China. PBS with a pH of 7.4 (10×) was purchased from Life Technologies. All other solvents (HPLC grade) were purchased from Sigma-Aldrich or Fisher Scientific. Milli-Q water with a resistivity of 18.2 MΩ·cm was used in this study. Dialysis tubing (500 MWCO) was purchased from SERVA Electrophoresis GmbH, Germany.

Instruments and Characterization

^{1}H nuclear magnetic resonance (^{1}H NMR) was recorded on a 250-MHz Bruker Spectrospin NMR spectrometer at 25 ℃. ^{13}C nuclear magnetic resonance (^{13}C NMR) and ^{1}H - ^{1}H correlation spectroscopy (COSY) were recorded on a 300-MHz Bruker Spectrospin NMR spectrometer at 25 ℃. Mass spectrometric (MS) data were carried out using LTQ Orbit rap XL instruments at Dalian University of Technology, Dalian, China. HPLC analysis was performed on an Agilent HPLC system equipped with a 1100 Series Quaternary pump, a 1200 Series diode detector, and a Merck Chromolith Performance RP18e 100-3 mm HPLC column. UV-Vis detector in the

HPLC system was set at 260 nm for analysis. UV-Vis absorption spectra were measured on a Lambda 900 spectrometer (Perkin Elmer). Fluorescence spectra were recorded on a TIDAS II spectrometer (J&M). Transmission electron microscopy (TEM) images were taken on a Hitachi HT7700 Transmission Electron Microscope. The diameters of the nanoparticles were determined by dynamic light scattering (DLS) on a Nano ZS90 particle size analyzer, Malvern (UK). A DPSS laser with a wavelength of λ= 671 nm (CNI-671-200-LN-AC-3, Laser 2000 GmbH, Germany) was used to induce photoreactions of $[Ru(Ptpy)(biq)(BPEG)](PF_6)_2$ and $[Ru(Ptpy)(biq)(BPEG)](PF_6)_2$ vesicles. The laser was equipped with a thermoelectric cooling system. The output power of the laser was controlled by a tabletop laser driver (PSU-III-FDA, Changchun New Industries Optoelectronics Technology Co., Ltd., China) and measured using an optical power meter (model 407A, Spectra-Physics Corporation). A laser at 671 nm was employed as the light source for *in vitro* and *in vivo* experiments. The output power of the laser was controlled by a fiber coupled laser system (FC-671-1W, Changchun New Industries Optoelectronics Technology) and measured by a power meter (LP100/TS15, Changchun New Industries Optoelectronics Technology).

Synthesis

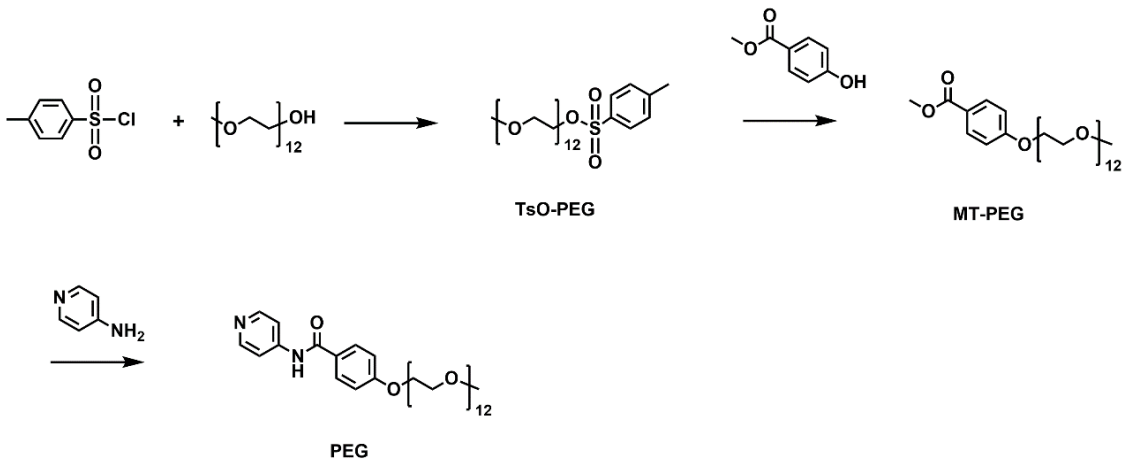

Figure S1. Synthetic route of PEG.

Synthesis of 3,6,9,12,15,18,21,24,27,30,33,36-dodecaoxaheptatriacontan-1-ol, 1-(4-methylbenzenesulfonate) (TsO-PEG) (Figure S1):

Methoxy-PEG12-hydroxyl (280.0 mg, 0.5 mmol) was dissolved in 3 mL THF, and then mixed with 1 ml NaOH aqueous solution (0.85 mM). The mixture was kept at 0 °C. A THF solution of *p*-toluenesulfonyl chloride (118.0 mg, 0.62 mmol) was added into the mixture. The reaction was further stirred overnight at room temperature. After reaction, the solution was concentrated in vacuo. The water-bath temperature was kept below 30°C. Subsequently, the concentrated solution was extracted with DCM two times. The combined organic layers were dried over Na2SO4. TsO-TEG was yielded as a pure colorless viscous liquid (315.3 mg, 0.44 mmol, 88%). ^{1}H NMR (250 MHz, CD_2Cl_2) δ 7.82 (d, J = 8.0 Hz, 2H), 7.41 (d, J = 7.9 Hz, 2H), 4.17 (d, J = 4.6 Hz, 2H), 3.63 (d, J = 2.5 Hz, 47H), 3.37 (s, 3H), 2.49 (s, 3H) (Figure S5).

Synthesis of methyl 4-[(26-hydroxy-3,6,9,12,15,18,21,24,27,30,33,36-octaoxahexacos-1-yl)oxy]benzoate (MT-PEG) (Figure S1):

TsO-TEG (300.0 mg, 0.42 mmol) was dissolved in 5 mL dry DMF, together with 4-hydroxybenzoate (77.0 mg, 0.5 mmol) and K2CO3 (116.0 mg, 0.84 mmol). The mixture was heated to 70°C for 20 h under nitrogen atmosphere. The solution displayed an intense brownish color shortly after launch. After reaction, water was added into the mixture. The crude product was extracted with DCM four times. The organic layers were combined and washed with water as well as brine, and subsequently dried over Na2SO4. After evaporation, the crude product was purified using column chromatography (eluent: methanol/DCM =1:20). MT-PEG was yielded as a pure colorless viscous liquid (225.2 mg, 0.32 mmol, 76%). ^{1}H NMR (250 MHz, CD_2Cl_2) δ 8.00 (m, 2H), 6.99 (d, J = 8.6 Hz, 2H), 4.21 (m, 2H), 3.88 (d, J = 3.1 Hz, 5H), 3.63 (s, 44H), 3.37 (s, 3H) (Figure S6).

Synthesis of benzamide, N-4-pyridinyl-4-[(26-hydroxy-3,6,9,12,15,18,21,24,27,30,33,36-octaoxahexacos-1-yl)oxy- (PEG) (Figure S1):

MT-PEG (69.4 mg, 0.1 mmol) and 4-aminopyridine (10.34 mg, 0.11 mmol) were dissolved in 1 mL THF (technical grade, stabilizer free). A THF solution of potassium tert-butoxide (2M, 0.1 mL) was added slowly to the mixture. The solution was further stirred uncapped for 2 h. The full conversion was monitored using TLC plate. After reaction, the solvent was evaporated. The crude product was purified using column chromatography (eluent: methanol/DCM = from 1:20 to 1:10) to yield a slight yellow liquid (60.3 mg, 0.079 mmol, 79%). ^{1}H NMR (250 MHz, CD_2Cl_2) δ 8.52 (d, J = 5.4 Hz, 2H), 8.44 (s, 1H), 7.94 (d, J = 8.6 Hz, 2H), 7.68 (d, J = 5.5 Hz, 2H), 7.06 (d, J = 8.7 Hz, 2H), 4.24 (t, J = 4.6 Hz, 2H), 3.89 (t, J = 4.8 Hz, 2H), 3.72 (dd, J = 5.8, 3.2 Hz, 2H), 3.61 (s, 40H), 3.53 (m, 2H), 3.36 (s, 3H) (Figure S7).

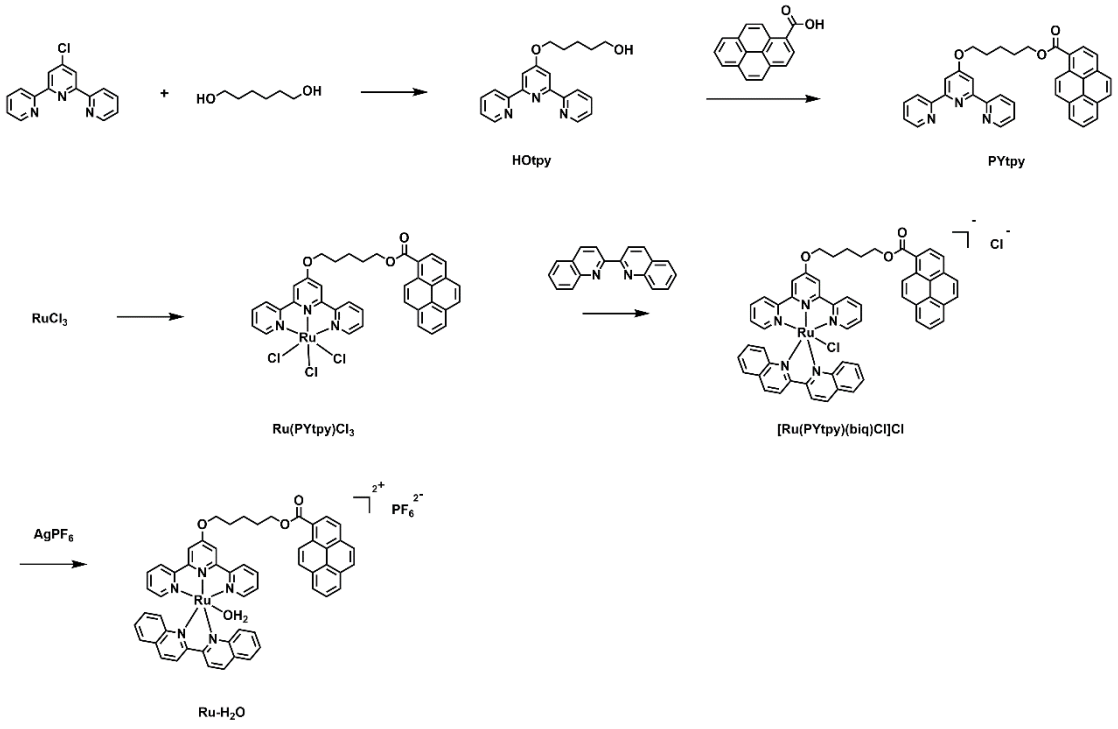

Figure S2. Synthetic route of Ru-H_2O.

Synthesis of 4'-hydroxyhexyloxy-2,2':6',2''-terpyridine (HOtpy) (Figure S2):

KOH (2.10 g, 37.5 mmol) were suspended in 32 mL dry DMSO. 1,6-dihydroxyhexane (4.41 g, 37.3 mmol) was added into the mixture. Subsequently, the mixture was stirred for 20 min at 80 °C under argon atmosphere. Then 4'-chloro-2,2':6',2''-terpyridine (1.83 g, 6.45 mmol) was added and the mixture was further stirred for 4 h at 80 °C. After reaction, the mixture was poured into 250 mL water and extracted with ethylacetate. The organic layer was combined and then removed by rotary evaporation. The resulting yellow oil was purified using column chromatography (eluent: ethyl acetate). HOtpy was obtained as a milky solid (1.72 g, 4.9 mmol, 76%). ^{1}H NMR (250 MHz, $CDCl_3$) δ 8.71 (dd, J = 15.1, 6.3 Hz, 4H), 8.09 (s, 2H), 7.92 (t, J = 7.6 Hz, 2H), 7.39 (dd, J = 7.6, 4.8 Hz, 2H), 4.30 (t, J = 6.3 Hz, 2H), 3.70 (t, J = 6.3 Hz, 2H), 1.89 (q, J = 6.8 Hz, 2H), 1.62 (m, 6H) (Figure S8).

Synthesis of 4-hydroxyhexyloxy-2,2':6',2''-terpyridine ester of pyrenecarboxylic acid (PYtpy) (Figure S2):

1-Pyrenecarboxylic acid (246.0 mg, 1 mmol), HOtpy (418.0 mg, 1.19 mmol) and DMAP (219.0 mg, 1.79 mmol) were dissolved in 25 ml dry DCM. DCC (309.0 mg, 1.5 mmol) was added to the mixture on an ice bath. The solution was then stirred for 24h at room temperature. After filtration, the solution was diluted with DCM, and washed with water followed by drying over MgSO4. The solution was concentrated, the resulting yellow oil was purified using column chromatography (eluent: ethyl acetate/petroleum ether = from 1:2 to 1:1). PYtpy was obtained as a yellow solid (387.4 mg, 0.67 mmol, 67%). ^{1}H NMR (250 MHz, $CDCl_3$) δ 9.19 (d, J = 9.5 Hz, 1H), 8.61 (d, J = 4.8 Hz, 2H), 8.54 (dd, J = 8.1, 2.2 Hz, 3H), 8.15 (m, 3H), 8.07 (m, 2H), 7.97 (m, 4H), 7.78 (t, J = 7.4 Hz, 2H), 7.25 (m, 2H), 4.46 (t, J = 6.5 Hz, 2H), 4.22 (t, J = 6.3 Hz, 2H), 1.87 (t, J = 5.8 Hz, 4H), 1.60 (m, 4H) (Figure S9).

Synthesis of Ru(PYtpy)Cl_3 (Figure S2):

$RuCl_3$•xH_2O (58.0 mg, 0.28 mmol) and PYtpy (162.0 mg, 0.28 mmol) were mixed in 40 mL absolute ethanol. The mixture was refluxed under argon for 4 h with vigorous magnetic stirring. After cooling down to room temperature, fine brown yellow powders appeared. The powders were filtered from the reddish yellow solution. The powders were then washed with ethanol and diethyl ether, followed by air-drying. Ru(PYtpy)Cl_3 was obtained as brown solid and used directly for next step (218.2 mg, 0.27 mmol, 98%).

Synthesis of [Ru(Ptpy)(biq)Cl]Cl (Figure S2):

Ru(PYtpy)Cl_3 (78.4 mg, 0.1 mmol) and 2,2'-biquinoline (25.6 mg, 0.1 mmol) were mixed in ethanol/H_2O mixture (14 mL, v/v = 1:1). The solution was bubbled with argon for 5 min and trimethylamine (15 µL) was then added to the mixture. The reaction was further refluxed under argon for 24 h. After reaction, the mixture was filtered hot. The filtrate was evaporated under reduced pressure. The crude product was purified using column chromatography (eluent: methanol/DCM =1:10 to 1:8). [Ru(PYtpy)(biq)Cl]Cl was obtained as violet powders (83.1 mg, 0.082 mmol, 82%). ^{1}H NMR (250 MHz, CD_2Cl_2) δ 9.72 (dd, J = 6.6, 3.6 Hz, 1H), 9.30 (d, J = 9.5 Hz, 1H), 8.87 (d, J = 8.8 Hz, 1H), 8.73 (m, 2H), 8.59 (d, J = 8.8 Hz, 1H), 8.24 (m, 13H), 7.86 (dd, J = 6.5, 3.4 Hz, 2H), 7.74 (m, 5H), 7.43 (t, J = 7.5 Hz, 1H), 7.27 (t, J = 7.9 Hz, 1H), 7.16 (t, J = 6.6 Hz, 2H), 6.90 (d, J = 8.9 Hz, 1H), 4.59 (q, J = 6.9 Hz, 4H), 2.07 (s, 4H) (Figure S10).

Synthesis of Ru-H_2O (Figure S2):

[Ru(PYtpy)(biq)(Cl)]Cl (50.0 mg, 0.049 mmol) and AgPF6 (30.0 mg, 0.11 mmol) were dissolved in acetone/ H_2O mixture (10 mL, v/v = 1:1). The solution was refluxed under argon

overnight in the dark. After reaction, the solution was cooled down and filtered to remove AgCl. The solvent was then reduced to ~5 mL. A saturated solution of KPF_6 was added. The resulting precipitate was filtered, washed with H_2O, and dried to give a fuchsia solid (45 mg, 0.036 mmol, 73%). ^{1}H NMR (250 MHz, CD_2Cl_2) δ 9.10 (d, J = 9.4 Hz, 1H), 8.86 (d, J = 8.8 Hz, 1H), 8.77 (d, J = 8.9 Hz, 1H), 8.64 (dd, J = 16.1, 8.3 Hz, 2H), 8.48 (d, J = 8.8 Hz, 1H), 8.31 (dd, J = 7.5, 5.6 Hz, 3H), 8.22 (m, 3H), 8.13 (m, 4H), 7.92 (m, 4H), 7.74 (dt, J = 22.5, 10.0 Hz, 5H), 7.49 (t, J = 7.4 Hz, 1H), 7.29 (d, J = 19.5 Hz, 3H), 6.97 (d, J = 8.6 Hz, 1H), 4.52 (dt, J = 10.0, 6.4 Hz, 4H), 2.02 (m, 4H), 1.78 (s, 4H) (Figure S11).

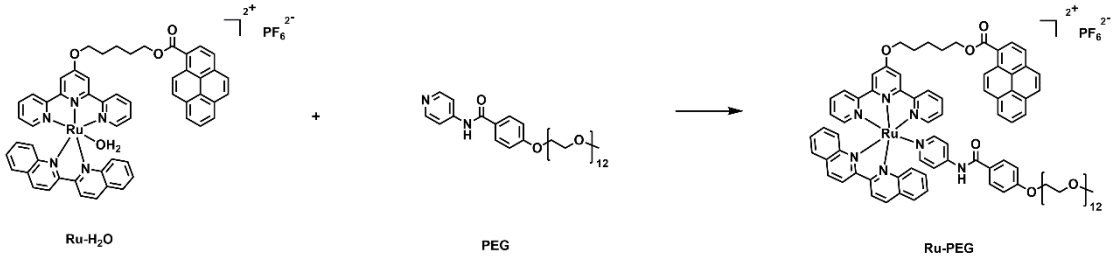

Figure S3. Synthetic route of Ru-PEG.

Synthesis of Ru-PEG (Figure S3):

Ru-H2O (60.0 mg, 0.048 mmol) and PEG (42.0 mg, 0.055 mmol) were mixed in 6 mL acetone. The solution was degassed for 5 min and refluxed overnight in the dark. After reaction, the solvent was evaporated. The resulting solid was then purified using column chromatography (eluent: methanol/DCM = from 1:10 to 1:6). Subsequently, the obtained product was further purified by precipitating from cold ethyl ether. The precipitates were filtered and then washed with cold ethyl ether, followed by drying in vacuum to a constant weight. Ru-PEG was obtained as a red solid (83.2 mg, 0.041 mmol, 87%). ^{1}H NMR (250 MHz, CD_2Cl_2) δ 9.14 (d, J = 9.4 Hz, 1H), 8.96 (s, 1H), 8.79 (d, J = 4.7 Hz, 2H), 8.55 (t, J = 7.6 Hz, 2H), 8.14 (m, 9H), 7.96 (q, J =

4.6 Hz, 4H), 7.78 (q, J = 7.2 Hz, 6H), 7.65 (d, J = 7.9 Hz, 2H), 7.40 (m, 3H), 7.27 (t, J = 5.5 Hz, 5H), 7.17 (d, J = 6.5 Hz, 2H), 6.76 (dd, J = 18.9, 8.6 Hz, 3H), 4.46 (t, J = 5.8 Hz, 4H), 4.01 (m, 3H), 3.70 (t, J = 4.5 Hz, 2H), 3.46 (s, 42H), 3.21 (s, 3H), 1.92 (s, 4H) (Figure S12). ESI-MS: $[M+Na-PF_6]^{2+}$: 929.85 (Figure S14).

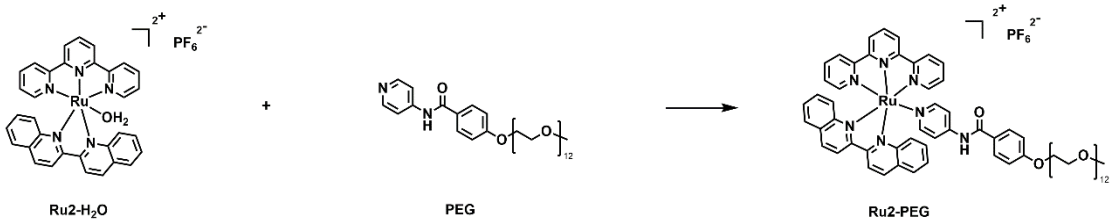

Figure S4. Synthetic route of Ru2-PEG.

Synthesis of Ru2-H_2O (Figure S4): It was synthesized according to the literature.

Synthesis of Ru2-PEG (Figure S4):

Ru2-H2O (50.0 mg, 0.055 mmol) and PEG (50.0 mg, 0.066 mmol) were mixed in 5 mL acetone. The solution was degassed for 5 min and reflux overnight in the dark. After reaction, the solvent was evaporated and purified using column chromatography (eluent: methanol/DCM =1:10). Subsequently, the obtained product was further purified by precipitating from cold ethyl ether. The precipitates were filtered and washed with cold ethyl ether, followed by drying in vacuum to a constant weight. Ru2-PEG was obtained as a pink solid (72.9 mg, 0.044 mmol, 81%). ^{1}H NMR (300 MHz, CD_2Cl_2) δ 9.11 (s, 1H), 8.98 (s, 2H), 8.70 (d, J = 8.8 Hz, 1H), 8.57 (d, J = 8.1 Hz, 2H), 8.36 (m, 5H), 8.02 (t, J = 7.9 Hz, 2H), 7.95 (d, J = 5.6 Hz, 2H), 7.88 (d, J = 8.5 Hz, 2H), 7.79 (t, J = 7.5 Hz, 2H), 7.55 (d, J = 6.8 Hz, 2H), 7.48 (m, 3H), 7.37 (m, 3H), 7.26 (d, J = 6.4 Hz, 2H), 6.93 (d, J = 8.5 Hz, 2H), 6.74 (d, J = 8.9 Hz, 1H), 4.16 (t, J = 4.5 Hz, 2H), 3.83 (t,

J = 4.6 Hz, 2H), 3.59 (d, J = 3.2 Hz, 44H), 3.33 (s, 3H) (Figure S15). ESI-MS: $[M-2PF_6]^{2+}$: 673.78 (Figure S17).

Sample preparation

Preparation of Ru-PEG vesicles:

2 mg Ru-PEG was dissolved in 0.4 mL THF. To trigger self-assembly of Ru-PEG, 1.6 mL distilled water was added dropwise into the solution. The dropwise speed was set as 2.5 sec/drop. The stirring rate was set as 500 rpm. Subsequently, the mixture was further stirred in the dark for 20 min. The obtained vesicles dispersion was kept still in the dark for 4 h. Afterwards the dispersion was dialyzed against 5 L Milli-Q water for 48 h using a dialysis tube (MW cutoff, 1 kDa). Milli-Q water was replaced every 12 h.

As a comparison, similar procedure was carried out to trigger self-assembly of Ru2-PEG. Specifically, 1.6 mL distilled water was added dropwise into 0.4 mL THF solution containing 2 mg Ru2-PEG. The dropwise speed was set as 2.5 sec/drop. The stirring rate was set as 500 rpm. The obtained solution was stirred in the dark for 20 min and further kept still in the dark overnight. Afterwards the solution was dialyzed against 5 L Milli-Q water for 48 h using a dialysis tube (MW cutoff, 1 kDa). Milli-Q water was replaced every 12 h.

Preparation of DiD dye-loaded Ru-PEG vesicles:

2 mg Ru-PEG was dissolved in 0.35 mL THF. 50 µL DiD solution (1 mg/mL in THF) was added into the Ru-PEG solution. To prepare DiD dye-loaded Ru-PEG vesicles, 1.6 mL distilled water was added dropwise into the mixture and kept still for another 4 h. The dropwise speed was set as 2.5 sec/drop. The stirring rate was set as 500 rpm. The DiD dye-loaded vesicles dispersion was dialyzed against 5 L Milli-Q water for 48 h using a dialysis tube (MW cutoff, 1 kDa). Milli-Q water was replaced every 12 h.

Cell experiments

Cell culture

4T1 mammary carcinoma cell line was cultured in RPMI-1640 medium. The medium was complemented with 10% fetal bovine serum (FBS, Invitrogen, USA) and 1% penicillin/streptomycin (Life Technologies, USA). The cell lines were maintained in humidified atmosphere at 37 °C and 5% of CO_2. 4T1 cell were treated with trypsin (0.25%) (Life technologies, USA) for 2 minutes to detach from cell culture flasks for further assays.

Cell viability assay

All cell viability tests were evaluated using a standard Cell Counting Kit-8 (CCK-8) assay kit (Solarbio, China). Typically, 4T1 cells were incubated with RPMI-1640 medium in 96-well plates at a density of 5.0×10^3 cells per well overnight. The medium was then replaced by RPMI-1640 that containing different metallodrugs assemblies in the dark. To investigate the cell viability under light irradiation, cell medium that containing Ru-H_2O or Ru-PEG vesicles was added and then cultured for 2 h, followed by irradiation for 15 min. Subsequently, cells were further incubated for 24 h. CCK-8 working solution was added as 10 μL per well, followed by another incubation for 2 h. Cell viability was assessed by measuring the absorbance at the wavelength of 450 nm on a microplate reader (EnSpire, Perkin Elmer). Treatment procedures were replicated five times for each sample.

Cell imaging by confocal laser scanning microscopy (CLSM)

For the cellular uptake experiments, 1×10^5 4T1 cells per milliliter were seeded in 35 mm diameter μ-dishes and cultured overnight in supplemented medium. The medium was replaced by fresh medium containing 30 μg/mL Ru-PEG vesicles or Ru-PEG after irradiation. The cells were incubated for 2 h. Ru-PEG vesicles were then removed by washing with PBS three times.

Live cells images were taken using CLSM (LSM710, Carl Zeiss). Ru-PEG vesicles were excited with a 405 nm laser and detected in the range from 425 to 475 nm.

For the colocalization experiments, 1×10^5 4T1 cells per milliliter were seeded in 35 mm diameter μ-dishes and cultured overnight in supplemented medium. The medium was replaced by fresh medium containing 30 μg/mL Ru-PEG vesicles. The cells were incubated for 2 h. After that, Ru-PEG vesicles were removed by washing with PBS three times. Lysosome was then stained by incubating with LysoTracker for 15 min. LysoTracker were further removed by washing with PBS. Live cells images were taken using CLSM (LSM710, Carl Zeiss). Ru-PEG were excited with a 405 nm laser and detected in the range from 425 to 475 nm. LysoTracker was excited with a 633 nm laser and detected in the range from 647 to 668 nm.

For the intracellular singlet oxygen ($^1O_2$) detection assay, the fluorescent probe DCFH-DA (Solarbio, China) was used according to the manufacture's instruction. Specifically, 1×10^5 4T1 cells per milliliter were seeded in 35 mm diameter μ-dishes and cultured overnight in supplemented medium. The cells were divided into five groups: (1) Control group; (2) + Light group; (3) + Ru-PEG vesicles + light group; (4) + Ru-PEG vesicles + probe group; (5) + Ru-PEG vesicles + light + probe group. The concentration of Ru-PEG was set as 30 μg/mL. Then each group was incubated with cells for 2 h. Afterwards, serum-free DCFH-DA solution (15 μM) was incubated with cells in (4) and (5) groups for 20 min. Cells in group (2), (3), and (5) were then irradiated with 671 nm red light for 15 min at an intensity of 25 mW/cm^2. Live cells imaged were taken using CLSM (LSM710, Carl Zeiss). DCFH-DA was excited with a 488 nm laser, detected in the range from 500 to 550 nm. The Ru-PEG vesicles were excited with a 405 nm laser and detected in the range from 425 to 475 nm.

The release of cathepsin B was detected using the fluorogenic Magic Red dye. Typically, 1×10^5 4T1 cells per milliliter were seeded in 35 mm diameter μ-dishes and cultured overnight in supplemented medium. The cells were divided into five groups: (1) Control group; (2) + DMSO

group; (3) + Light group; (4) + Ru-PEG vesicles group; (5) + Ru-PEG vesicles + light group. The concentration of Ru-PEG was set as 30 μg/mL. Cells in (2) were set as positive control group. Cells in group (3) and (5) were irradiated with 671 nm red light for 15 min at an intensity of 25 mW/cm^2. The cells were incubated for 2 h and then washed with PBS twice. Afterwards, Magic Red dye was treated with cells and further incubated for 1 h. After being washed twice with PBS, the cells were visualized by CLSM (LSM710, Carl Zeiss). Magic Red was excited with a 543 nm laser and detected in the range from 610 to 650 nm.

Multicellular tumor spheroids (MTSs) experiments

MTSs construction

MTSs were established using the handing drop method. Typically, 96-well plates were pretreated with 50 μL of 1.5% agarose per well. After cooling down to room temperature, the agarose gel formed. 1×10^5 4T1 cells per well were dropped slowly onto the agarose lid. 100 μL RPMI 1640 medium was added to each well, and replaced every 2 days, to culture the MTS. The lid was then slowly transferred to the cell incubator. After 4 days of incubation, the MTSs formed and used for further experiments.

Penetration analysis

4T1 MTSs were established and gently transferred to a confocal dish. By washing wish PBS once, the MTSs were treated with Ru-PEG or Ru-PEG pre-irradiated for 15 min. After 12 h or 24 h incubation, the MTSs were gently washed with PBS twice. The penetration depth in MTSs was investigated using CLSM in Z-stacks with 25 μm Z-intervals from apex to equator. Ru-PEG were excited with a 405 nm laser and detected in the range from 425 to 475 nm.

Animal experiments

Animal use and tumor model establishment

BALB/c mice (female, 18-20 g, 4-6 weeks) were purchased from Vital River Laboratory Animal Center (Beijing, China). All mice were maintained under specific pathogen-free conditions and had free access to food and water throughout all the experiments. All protocols for animal studies conformed to the Guide for the Care and Use of Laboratory Animals.

The tumor model was established by inoculating 1.2×10^6 4T1 cells in the flank region of each mouse. Tumor volume was measured using a vernier caliper and calculated as $V=L*W^2/2$, where L and W were the length and width of the tumor, respectively.

Hemolysis analysis

The fresh whole blood was obtained from BALB/c mice using sodium citrate as an anti-coagulant with a blood/ anticoagulant ratio of 9:1. The whole blood was subsequently centrifuged at 1000 × g for 5 min and then the plasma and buffy coat layer were removed. The obtained red blood cells (RBCs) were collected and washed with saline for three times, followed by suspending in 15 mL saline. The RBCs suspension was incubated with saline containing different concentrations of Ru-PEG vesicles with the ratio of 1:1 (v/v). The final concentration of Ru-PEG vesicles was ranging from 100 to 500 μg/mL. The positive hemolysis control was induced by replacing saline with same volume of water. The negative hemolysis control was saline without any Ru-PEG vesicles. Each sample was repeated three times. All samples were incubated at 37 ℃ for 24 h. After incubation, the RBCs were centrifuged at 1000 × g for 5 min. The absorbance of supernatants at 540 nm was measured by microplate reader. The hemolysis percentage was calculated by measuring the optical density (OD) as the following formula:

Hemolysis (%) = [(OD of sample absorbance – OD of background absorbance)/ (OD of positive control –OD of negative control)] × 100%.

In vivo fluorescence imaging

When the tumor size was approximately 100 mm^3, 4T1 tumor-bearing mice were treated with saline as control group or DiD-loaded Ru-PEG vesicles as experimental group. Saline or Ru-PEG was intravenously injected. The dosage of Ru-PEG vesicles was 10 mg/kg. 0, 4, 8, 12, 24 h post injection, the mice were anesthetized with isoflurane and imaged under the in vivo imaging system (IVIS Spectrum, PerkinElmer). The excitation wavelength was fixed at 633 nm.

In vivo anticancer efficacy evaluation

The anticancer efficacy was evaluated by monitoring the tumor volumes using 4T1 tumor-bearing mice. The tumor nodules were allowed to reach approximately 100 mm^3 before initial treatment. All the mice were numbered using ear tags. The initial tumor volume and body weight were recorded. Subsequently, the mice were randomly divided into four groups: (1) a group of 4T1 tumor-bearing mice was injected with saline (control group); (2) a group of 4T1 tumor-bearing mice was injected with saline and irradiated with light only (light group); (3) a group of 4T1 tumor-bearing mice was injected with Ru-PEG vesicles (Ru-PEG group); (4) a group of 4T1 tumor-bearing mice was injected with Ru-PEG vesicles and irradiation at tumor sites 12 h post injection (Ru-PEG + light group). The number of mice in each group was five. Injections were performed on the first, third and fifth day during the treatments. Mice in group (3) and (4) were treated with equivalent dosage of 4 mg/kg Ru-PEG vesicles. 671 nm light irradiation (125 $mWcm^{-2}$, 15 min) in group (4) was performed after 12 h i.v. injection of Ru-PEG vesicles. To exclude the effect by light irradiation, Mice in group (2) were set as a negative control. The body weight and tumor volume of each mouse were measured every day. At day 17, mice in each group were sacrificed. Tumor were isolated for weighing.

Histological analyses

At the end of tumor inhibition experiments, the mice from each group were sacrificed and tumor were collected. Main organs including heart, liver, lung, kidney and spleen were also collected and fixed in 4% formaldehyde solution followed by paraffin embedding. The treated tumors and organs were then cut into pieces with thickness of 2 μm, and stained with hematoxylin and eosin (H&E) to assess histological alterations by microscope. Embedding and H&E staining were done by Wuhan Servicebio Technology Co., Ltd.

TUNEL and Ki67 assay

The isolated tumors were fixed in 4% formaldehyde solution followed by paraffin embedding and TUNEL/Ki67 staining. Typically, the paraffin embedded tumors were cut into approximately 8.0 μm by a rotary microtome (YD-1508A) and stained with 0.25% toluidine blue O. The DNA fragmentation was labelled using a TUNEL apoptosis detection kit. The cell proliferation indicator Ki67 staining assays were performed according to the standard protocol. Embedding and TUNEL/Ki67 staining were done by Wuhan Servicebio Technology Co., Ltd. Antibodies were purchased from Wuhan Servicebio Technology Co., Ltd. Samples were observed by CLSM.

Statistical analysis

One-way ANOVA with Tukey's multiple comparison analysis was used to determine the significance of differences between different groups. Data were calculated and appropriate statistical results were marked as $*p < 0.05$ and $***p < 0.001$.

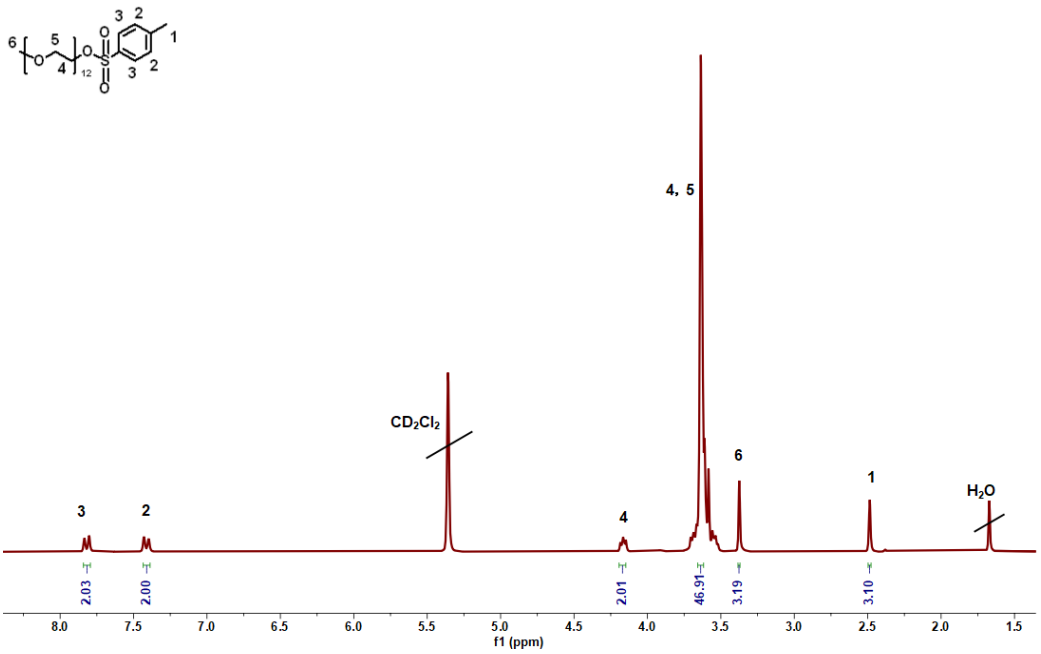

Figure S5. ^{1}H NMR of TsO-PEG (250 MHz, CD_2Cl_2).

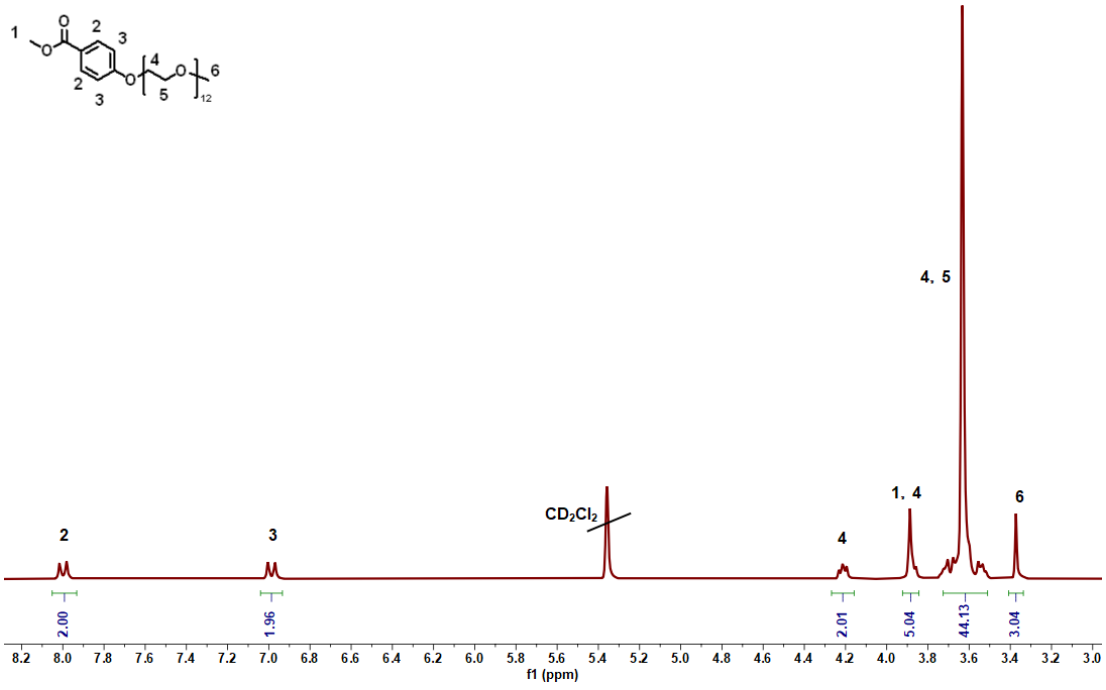

Figure S6. ^{1}H NMR spectrum of MT-PEG (250 MHz, CD_2Cl_2).

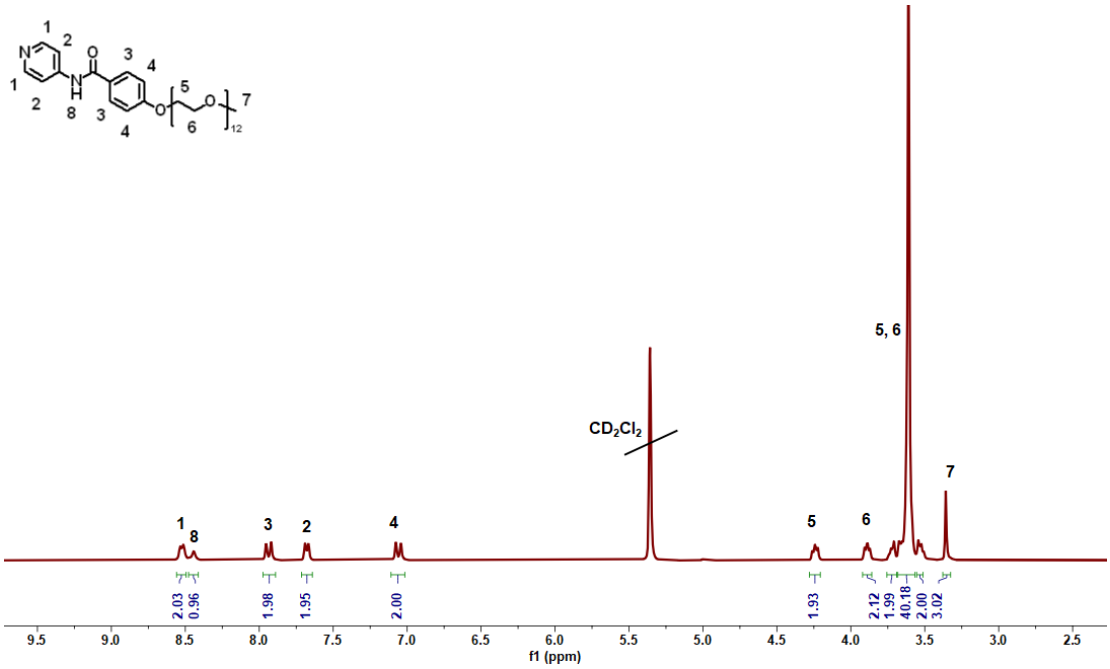

Figure S7. ^{1}H NMR of PEG (250 MHz, CD_2Cl_2).

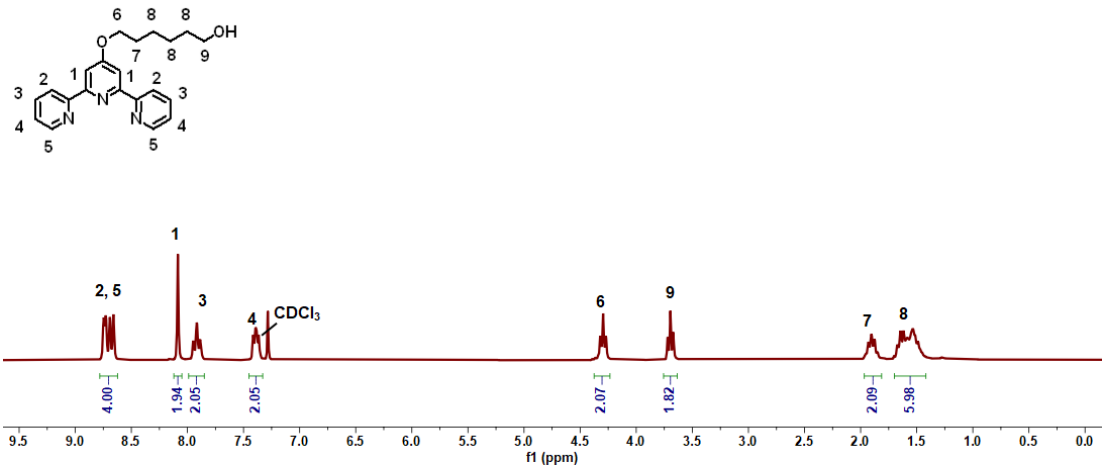

Figure S8. ^{1}H NMR of HOtpy (250 MHz, $CDCl_3$).

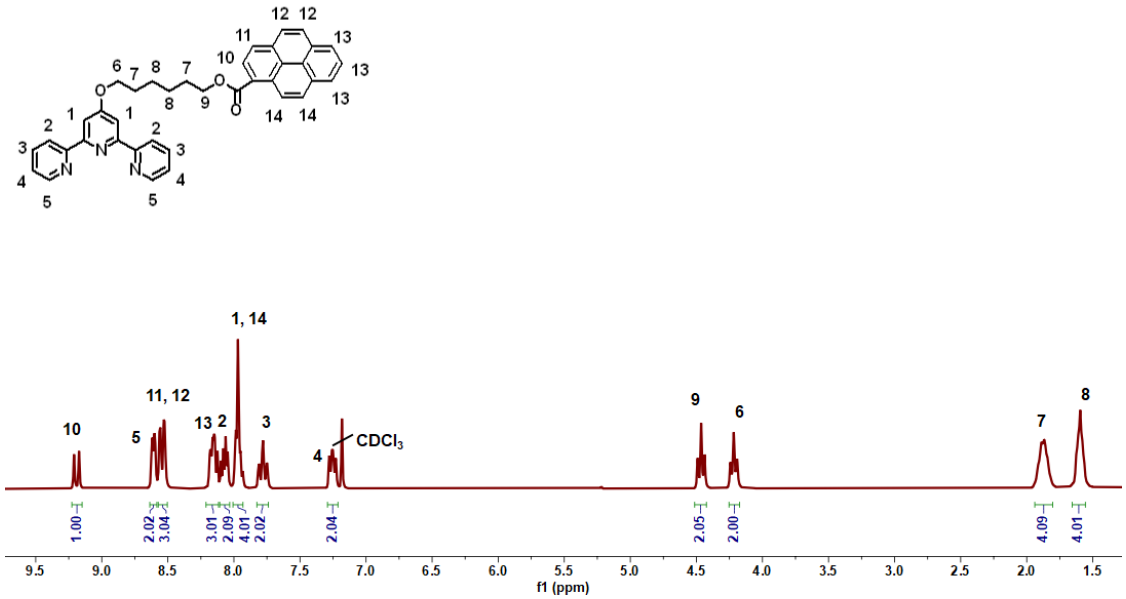

Figure S9. ^{1}H NMR of PYtpy (250 MHz, $CDCl_3$).

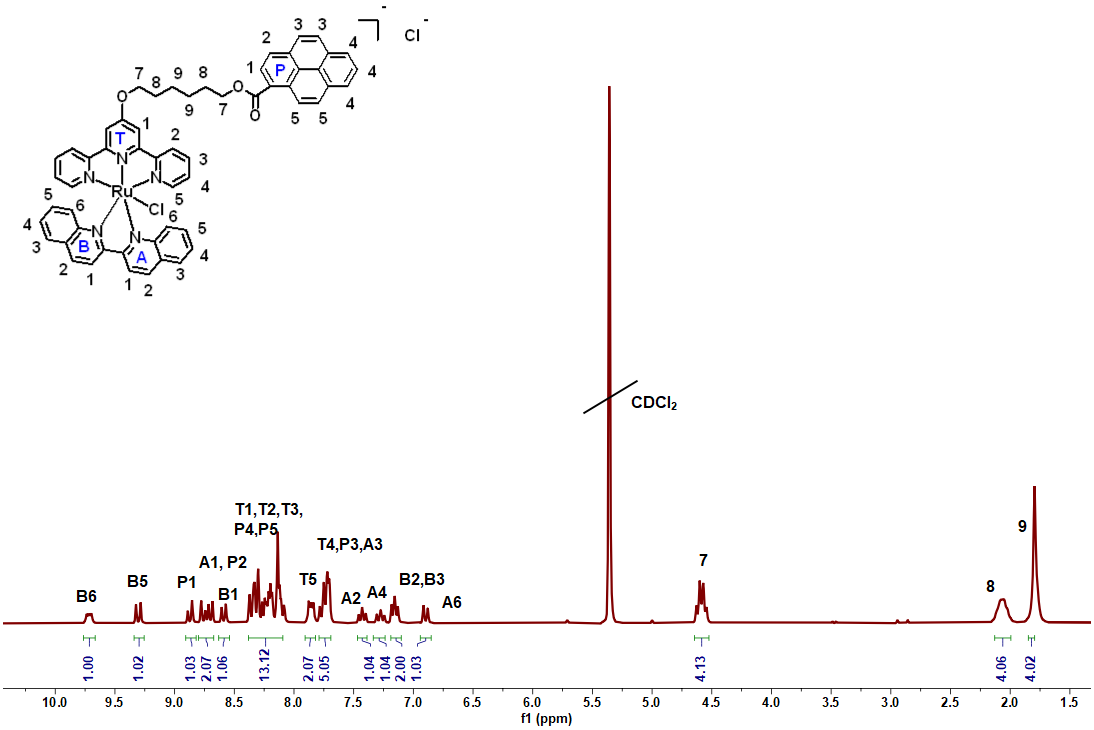

Figure S10. ^{1}H NMR of [Ru(PYtpy)(biq)Cl]Cl (250 MHz, CD_2Cl_2).

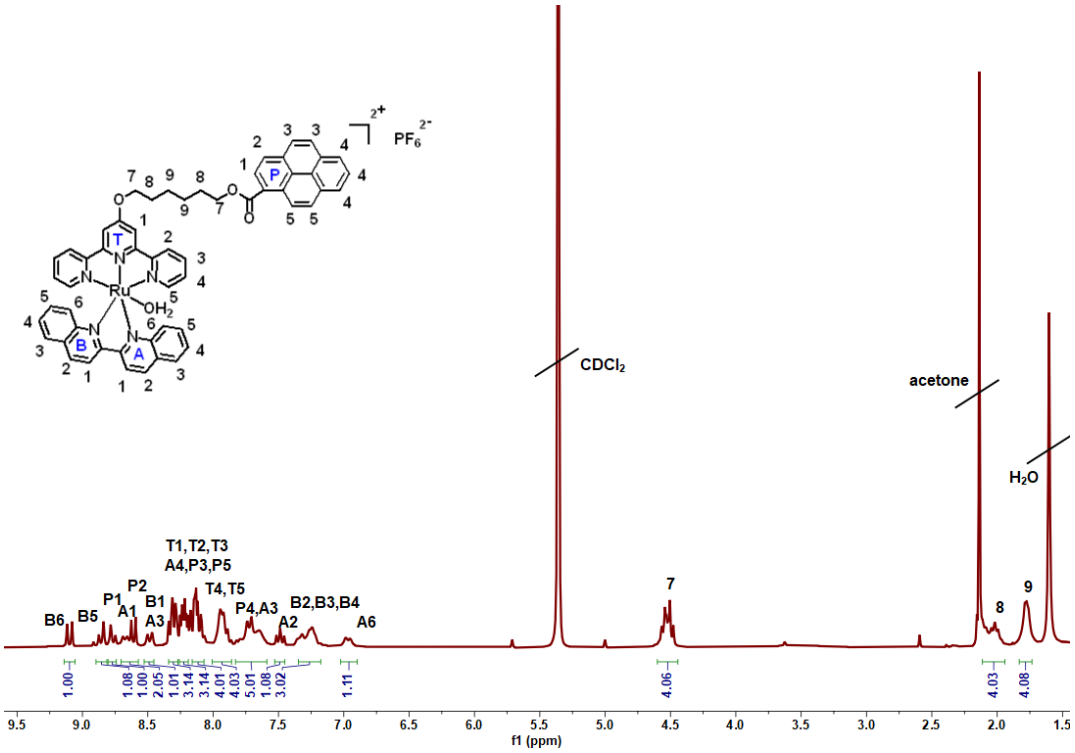

Figure S11. ^{1}H NMR of Ru-H_2O (250 MHz, CD_2Cl_2).

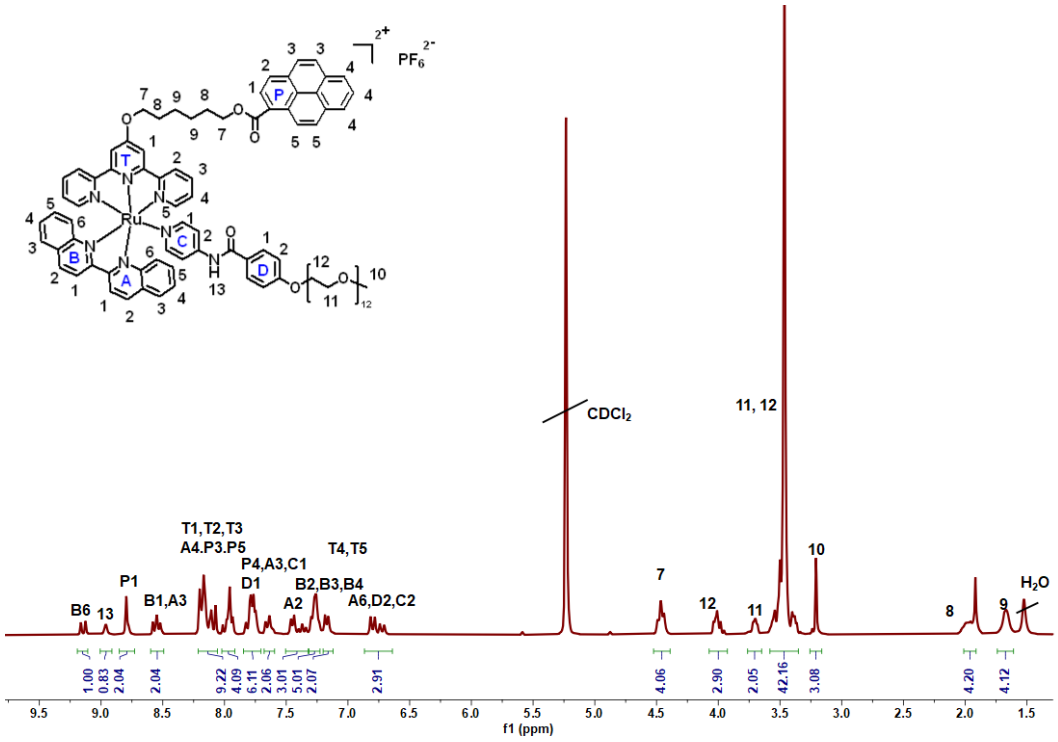

Figure S12. ^{1}H NMR of Ru-PEG (300 MHz, CD_2Cl_2).

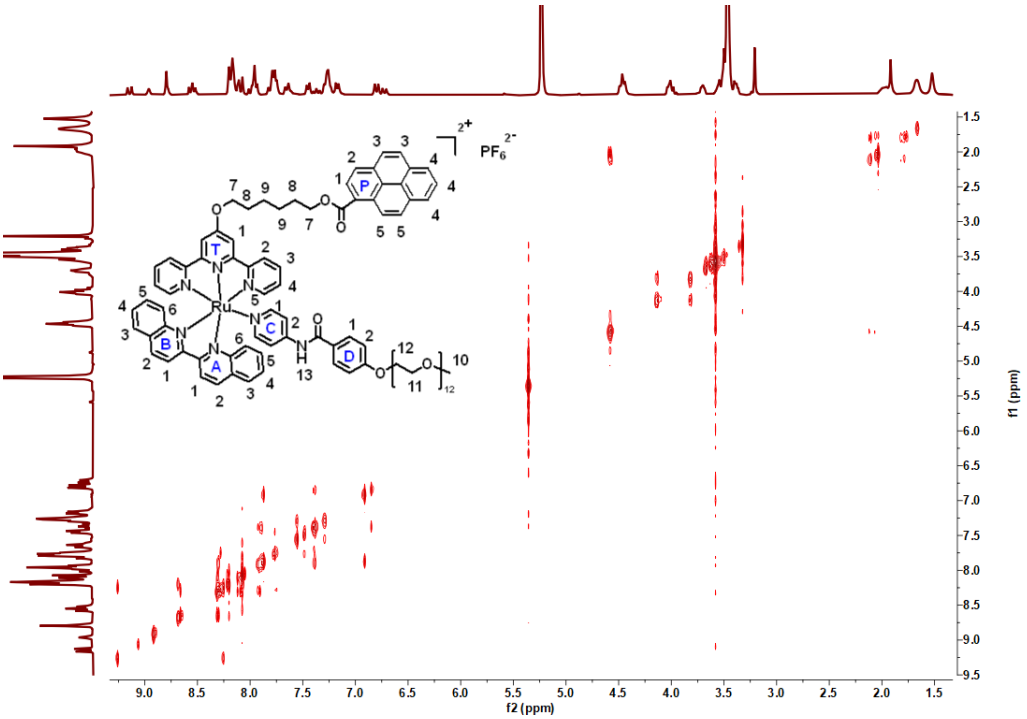

Figure S13. COSY of Ru-PEG (300 MHz, CD_2Cl_2).

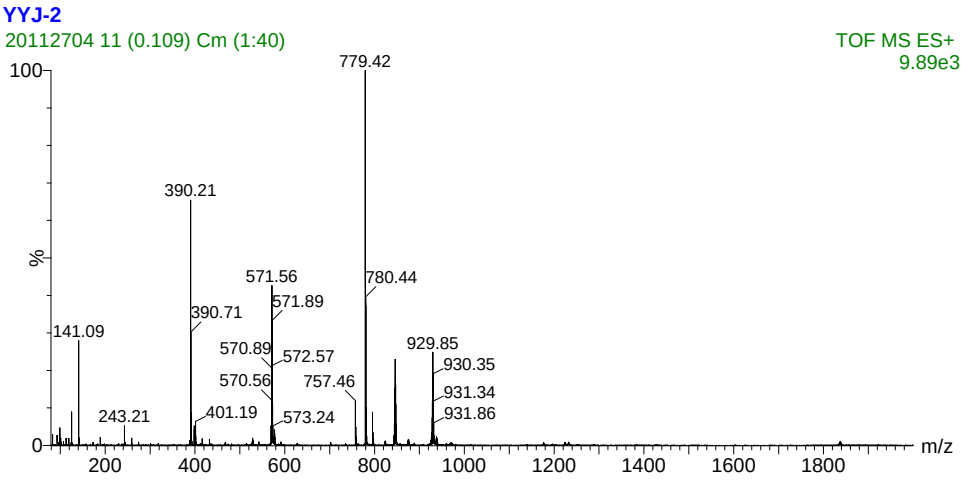

Figure S14. ESI-MS of Ru-PEG (M = Ru-PEG, L = PEG). m/z = 929.8 is assigned to $[M+Na-PF_6]^{2+}$, m/z = 571.5 is assigned to $[M+Na-2PF_6]^{3+}$, m/z = 779.5 is assigned to $[L+Na]^{+}$, m/z = 390.2 is assigned to $[L+H+Na]^{2+}$.

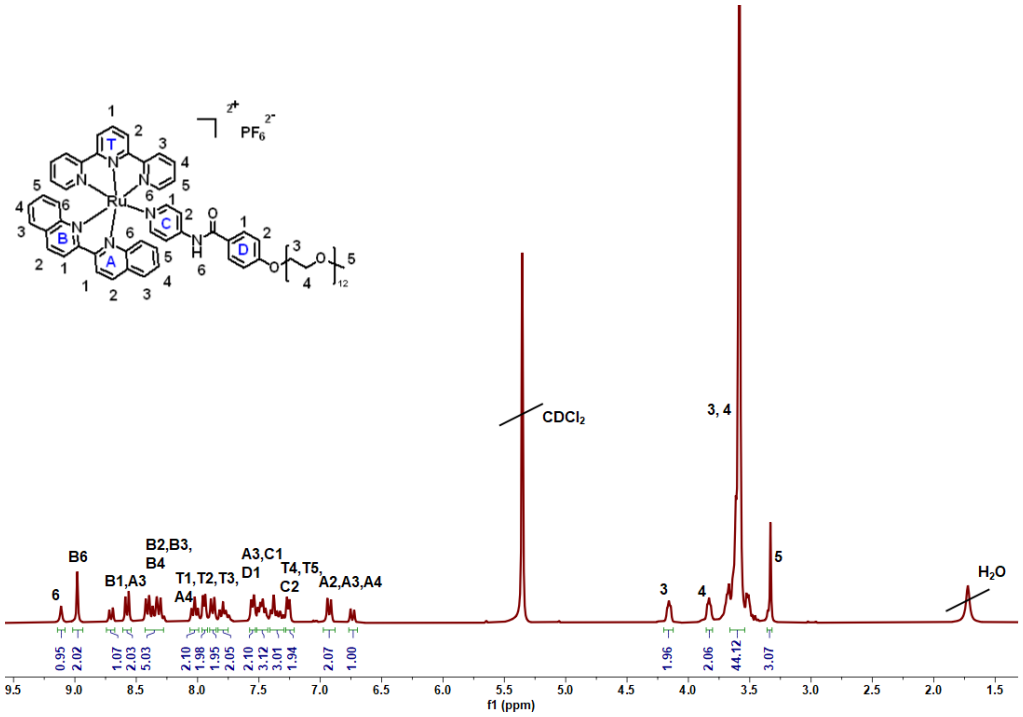

Figure S15. ^{1}H NMR of Ru2-PEG (300 MHz, CD_2Cl_2).

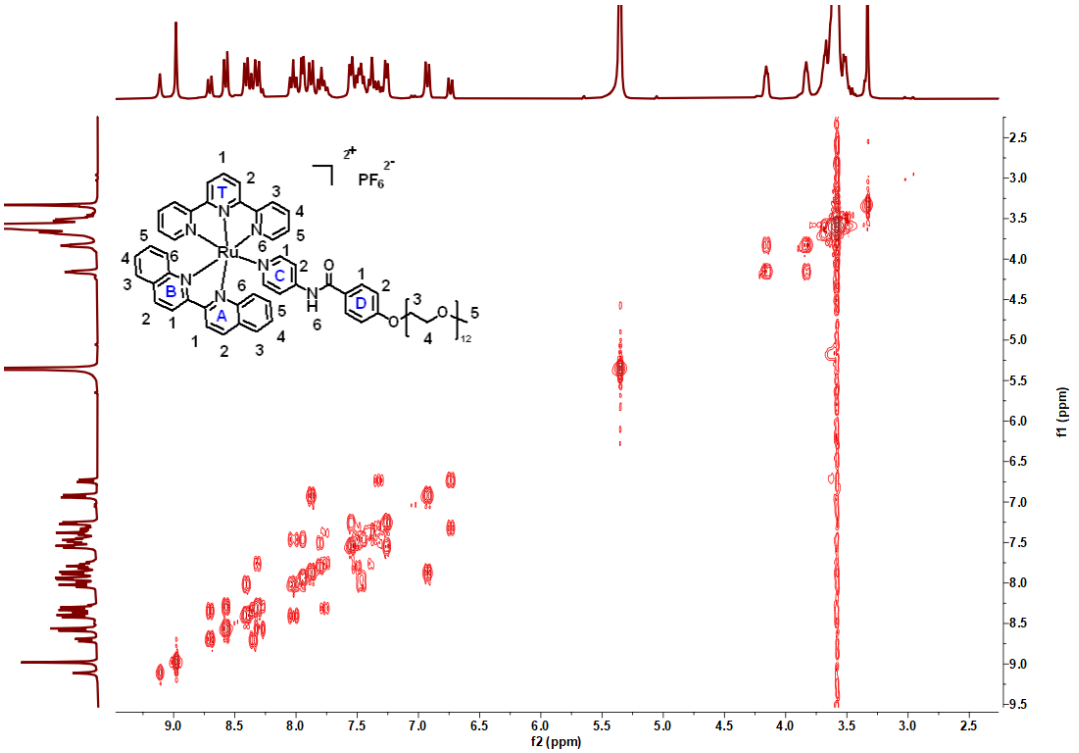

Figure S16. COSY of Ru2-PEG (300 MHz, CD_2Cl_2).

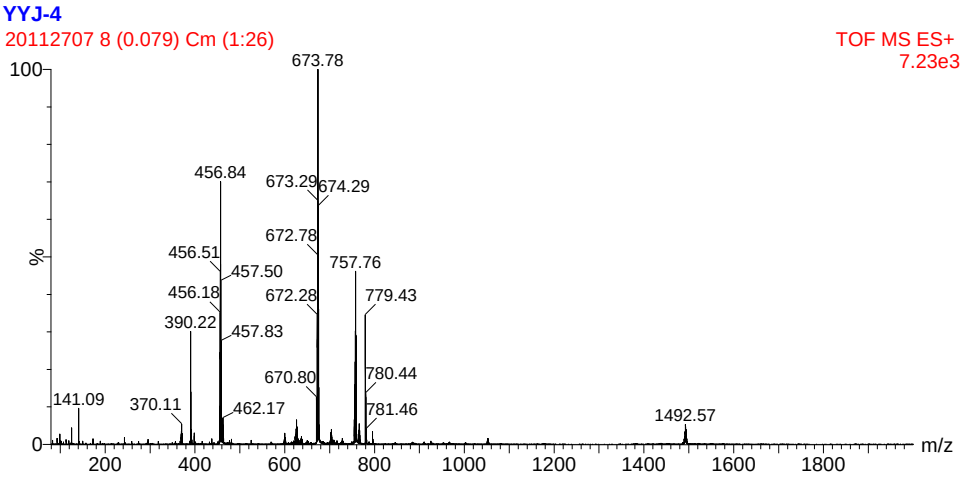

Figure S17. ESI-MS of Ru2-PEG (M = Ru2-PEG, L = PEG). m/z = 456.84 is assigned to $[M+Na_2PF_6]^{3+}$, m/z = 673.78 is assigned to $[M-2PF_6]^{2+}$, m/z = 757.76 is assigned to $[M+Na-PF_6]^{2+}$, m/z = 390.22 is assigned to $[L+Na+H]^{2+}$.

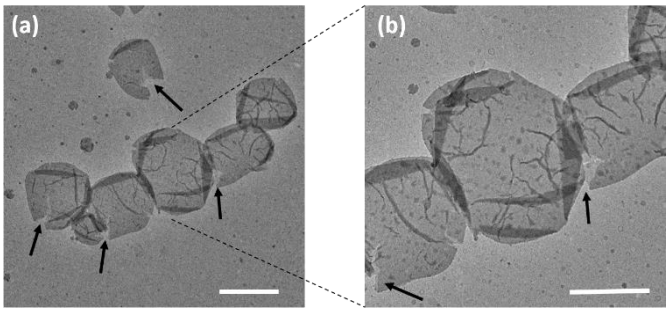

Figure S18. (a) TEM image of self-assembled Ru-PEG. Scale bar: 500 nm. (b) TEM image of self-assembled Ru-PEG in the selected area. Scale bar: 200 nm. Some nano-objects with open mouths (indicated as black arrows) illustrated that these self-assembled Ru-PEG are hollow and vesicular.[1]

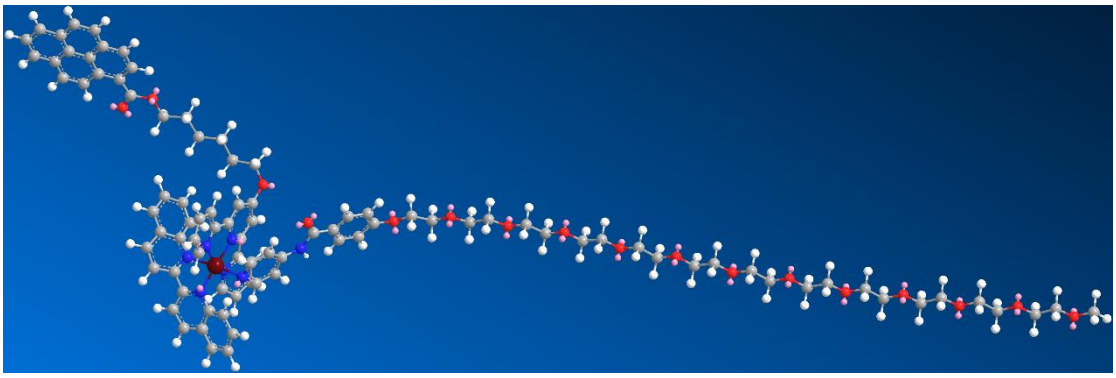

Figure S19. Molecular dynamics simulation using MM2 method by Chem3D software for Ru-PEG molecule. The length of one Ru-PEG molecule was calculated to be ~6.2 nm. The wall thickness of self-assembled Ru-PEG was measured to be ~12 nm, which was consistent with two times of the length of one Ru-PEG molecule. These results further demonstrated Ru-PEG self-assembled into vesicles.

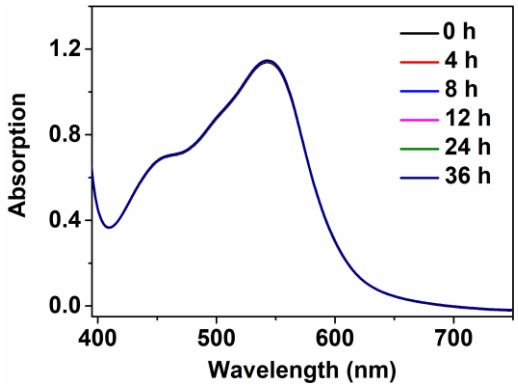

Figure S20. Stability of Ru-PEG vesicles over 36 h studied by UV-vis. The UV-vis spectra showed negligible change after 36 h, indicating good stability of Ru-PEG vesicles.

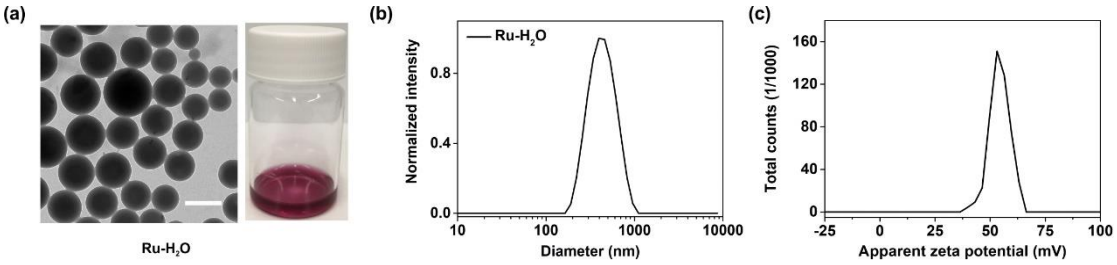

Figure S21. (a) TEM image and photograph of Ru-H_2O large compound micelles (LCMs). Scale bar: 500 nm. (b) The diameter of Ru-H_2O LCMs measured by DLS. (c) Zeta potential of Ru-H_2O LCMs.

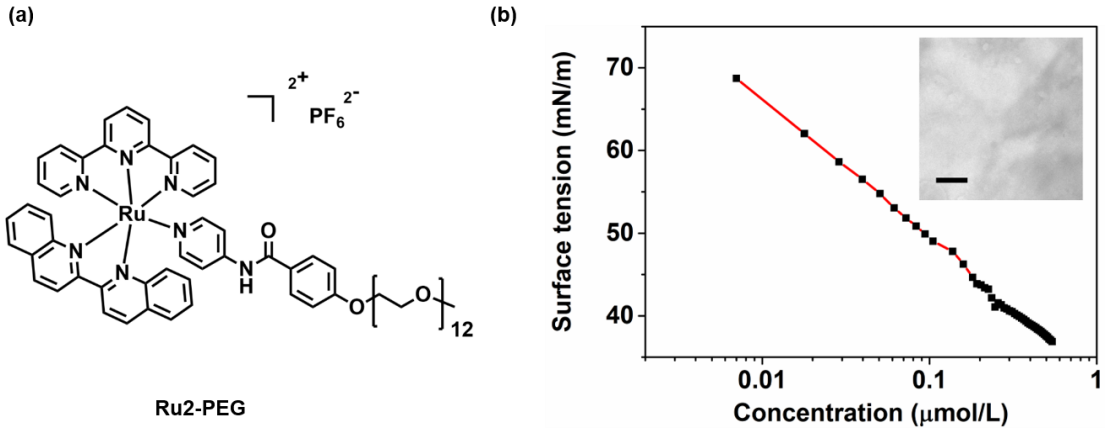

Figure S22. (a) Chemical structure of Ru2-PEG. (b) Surface tension of Ru2-PEG upon adding of water. The inserted figure shows the TEM image of self-assembly of Ru2-PEG which is lacking of the pyrene moiety. Comparing with the self-assembled nanostructure of Ru-PEG in Figure 2 in the main manuscript, Ru2-PEG showed random aggregates reminiscent of a precipitate. These results clearly showed Ru-PEG were able to self-assemble into vesicles most probably due to the π-π stacking and hydrophobic effect of pyrene moiety.

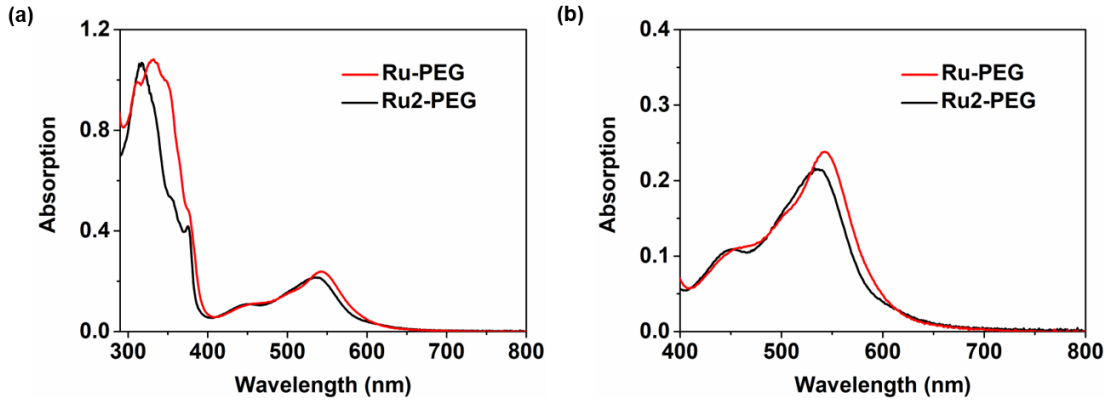

Figure S23. (a) UV-Vis spectrum of self-assembled Ru-PEG and Ru2-PEG. (b) Enlarged UV-Vis spectrum of self-assembled Ru-PEG and Ru2-PEG from 400 nm to 800 nm. The MLCT band of Ru2-PEG located at 533 nm. The MLCT band of Ru-PEG located at 543 nm, which was red shifted by 10 nm than that of Ru2-PEG. The red-shifted wavelength demonstrated the presence of π-π stacking interactions in Ru-PEG, owing to the pyrene moiety.[2] Moreover, the

bathochromic absorption peak increased, which also indicated the aggregation process originated from pyrene moiety.[3] These results clearly demonstrated that the introducing of pyrene contributed the self-assembly via π-π stacking.

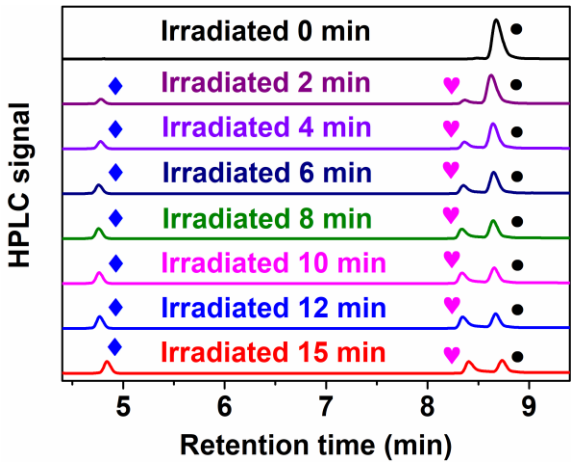

Figure S24. The released behavior of Ru-PEG vesicles upon light irradiation studied by HPLC. The black dots (●) reflect Ru-PEG, the magenta heart shape (♥) reflect the released Ru-H_2O, and the blue diamond (♦) reflect the released PEG ligand.

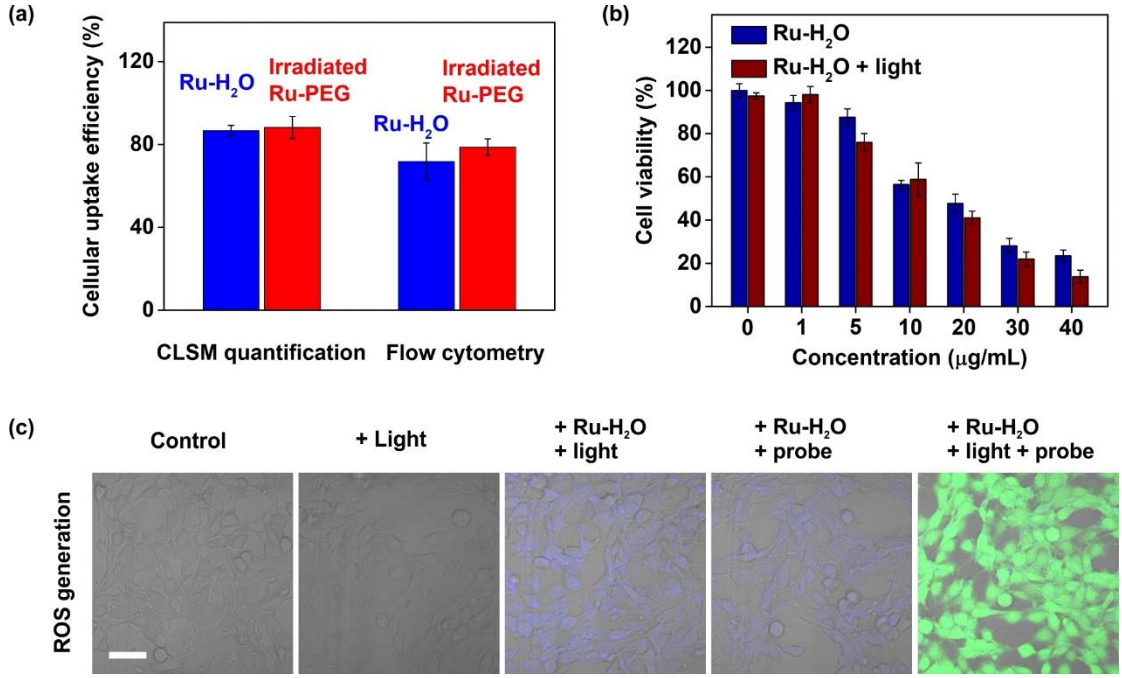

Figure S25. (a) Cellular uptake by 4T1 cells when treated with Ru-H_2O LCMs and irradiated Ru-PEG. Quantifications were calculated using imageJ software from CLSM images and flow cytometry. (b) Viability of 4T1 cancer cells treated with various concentration of Ru-H_2O LCMs in the dark and under light irradiation. The cells were incubated with Ru-H_2O for 2 h and followed by irradiating with 671 nm red light (25 mW cm^{-2}, 15 min). Cell viability was tested after the cells were further incubated in the dark for 24 h. (c) Generation of intracellular $^1O_2$ in 4T1 cells observed by CLSM. $^1O_2$ was detected using the indicator DCFH-DA (green). Scale bars: 50 μm.

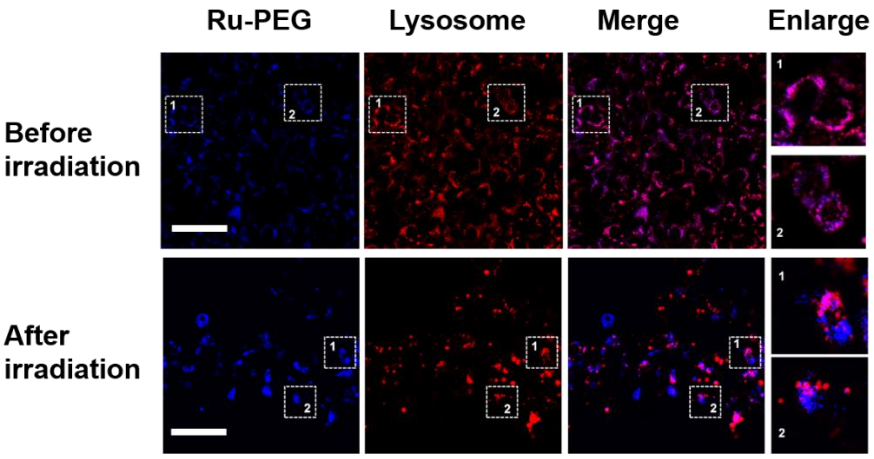

Figure S26. CLSM images of Ru-PEG colocalized with lysosome. The cells were incubated with Ru-PEG for 2 h or incubated with Ru-PEG followed by irradiating with red light (671 nm, 25 mW cm^{-2}, 15 min). Lysosome was stained using LysoTracker dyes. Ru-PEG vesicles were excited with a 405 nm laser (blue). Lysosome was labelled using LysoTracker deep red and excited with a 633 nm lase (red). Scale bars: 100 μm. Before light irradiation, Ru-PEG was preferably colocalized with lysosome. Whereas, after light irradiation, partial Ru-PEG was observed to escape from lysosome.

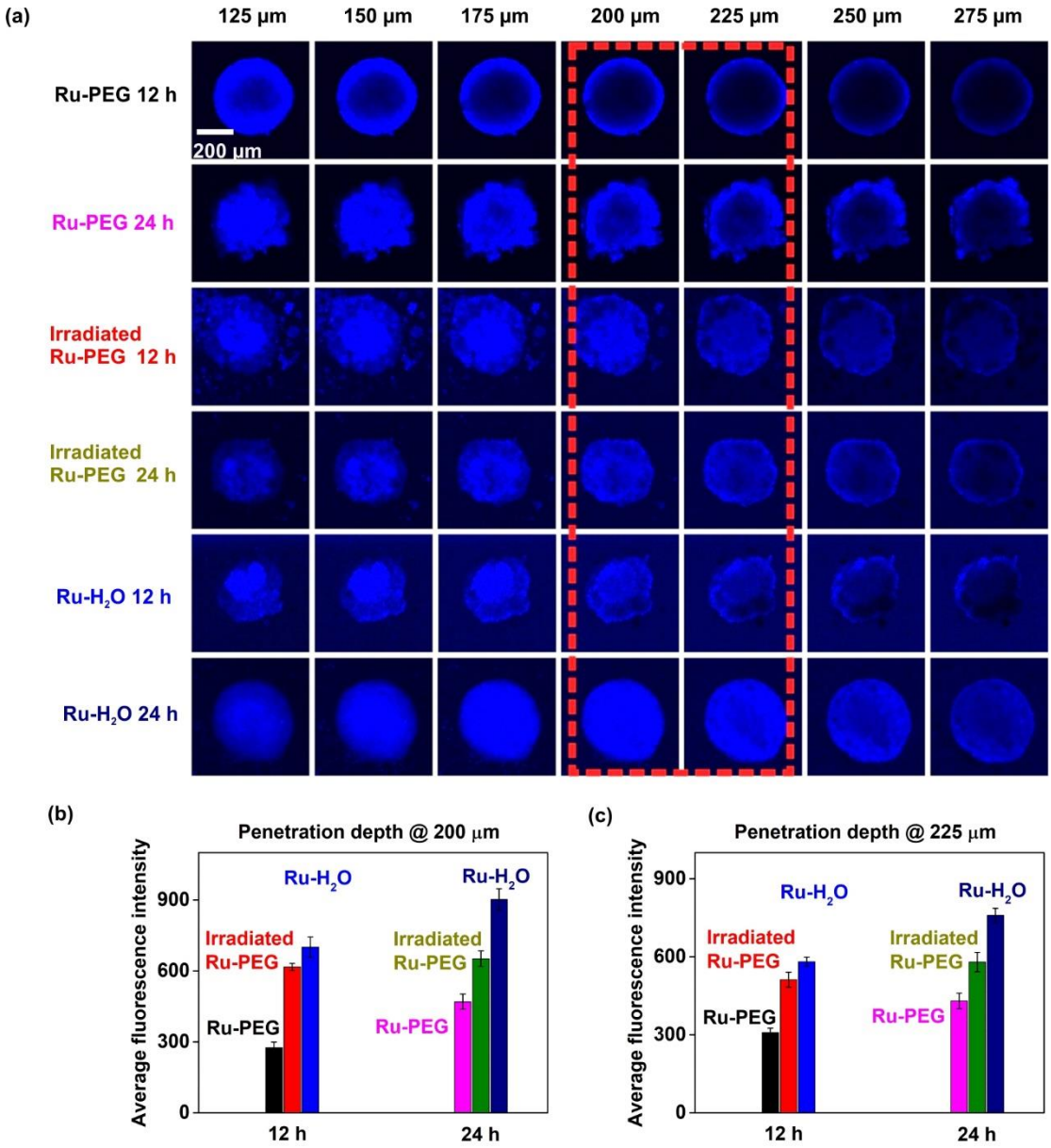

Figure S27. (a) In vitro tumor penetration of Ru-PEG vesicles, irradiated Ru-PEG and Ru-H_2O LCMs in 4T1 multicellular tumor spheroids (MTS). Ru-PEG and Ru-H_2O were excited at 405 nm. The MTS were visualized using CLSM in Z-stacks with 25 μm intervals. Scale bar = 200 μm. (b) Average fluorescence intensity at 200 μm penetration depth calculated by ImageJ software. (c) Average fluorescence intensity at 225 μm penetration depth calculated by ImageJ software.

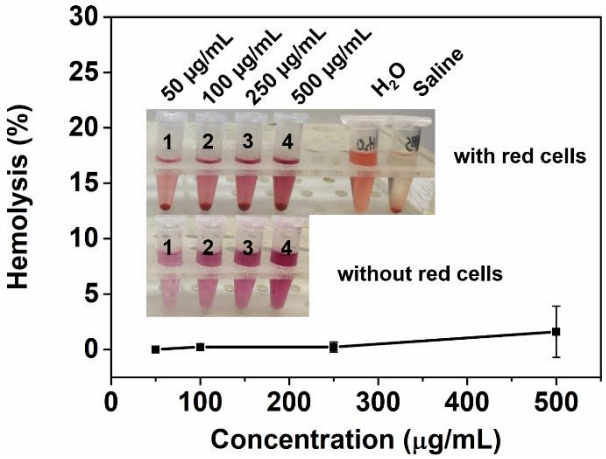

Figure S28. Blood hemolysis treated with Ru-PEG vesicles at various concentrations from 50 μg/mL to 500 μg/mL. Water was set as a positive control and saline was set as a negative control. Even after incubation for 24 h, these nanoparticles exhibited non-hemolytic with hemolysis lower than the permissible level of 5%. Ru-PEG vesicles were compatible with red blood cells.

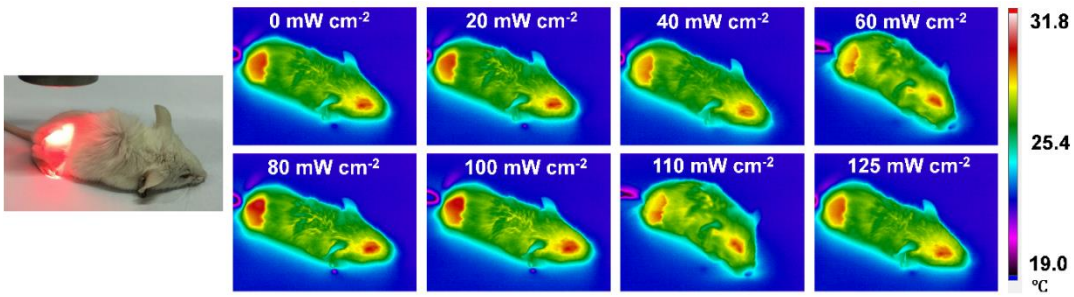

Figure S29. Thermal IR imaging of a 4T1 tumor-bearing mouse exposed to 671 nm red light irradiation at various dosages. Light irradiation did not cause overheating problem.

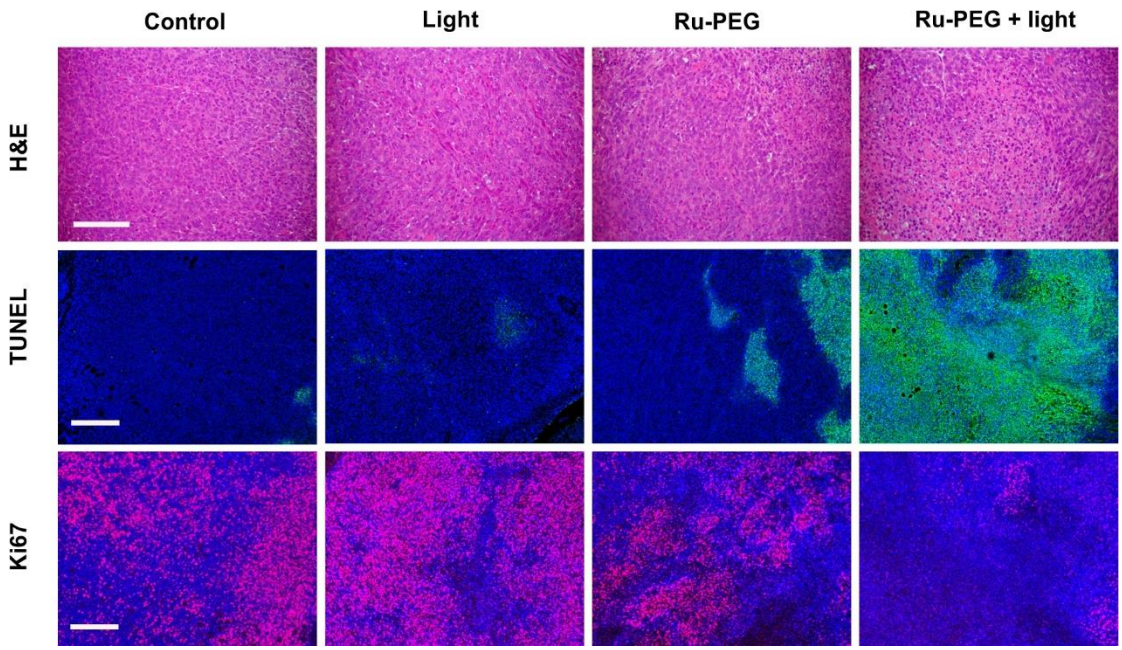

Figure S30. Histopathological analysis by H&E staining of tumor sections isolated from 4T1 tumor-bearing mice. Scale bar: 100 μm.

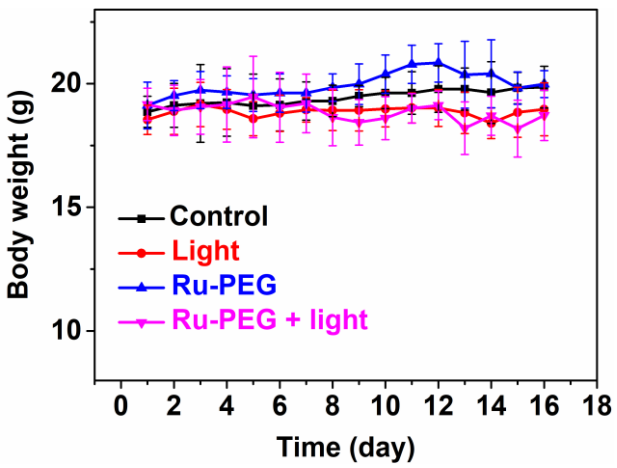

Figure S27. Body weight changes of mice during treatments (n = 5).

Reference

[1] L. Chen, J. Xiang, Y. Zhao, Q. Yan, Reversible self-assembly of supramolecular vesicles and nanofibers driven by chalcogen-bonding interactions, Journal of the American Chemical Society 140(23) (**2018**) 7079-7082.

[2] R. Nandy, M. Subramoni, B. Varghese, S. Sankararaman, Intramolecular π-stacking interaction in a rigid molecular hinge substituted with 1-(pyrenylethynyl) units, The Journal of organic chemistry 72(3) (**2007**) 938-944.

[3] P.P. Yang, Q. Luo, G.B. Qi, Y.J. Gao, B.N. Li, J.P. Zhang, L. Wang, H. Wang, Host materials transformable in tumor microenvironment for homing theranostics, Advanced Materials 29(15) (**2017**) 1605869.

Chapter 3: Fighting against drug-resistant tumors using a dual-responsive Pt(IV)/Ru(II) bimetallic polymer

Xiaolong Zeng, Yufei Wang, Jianxiong Han, Wen Sun, Hans-Jürgen Butt, Xing-Jie Liang, and Si Wu**

X. Zeng, J. Han, Prof. S. Wu

CAS Key Laboratory of Soft Matter Chemistry

Hefei National Laboratory for Physical Sciences at the Microscale

Department of Polymer Science and Engineering

University of Science and Technology of China

Hefei 230026, China

E-mail: siwu@ustc.edu.cn

Y. Wang, Prof. X.-J. Liang

Chinese Academy of Sciences (CAS) Key Laboratory for Biomedical Effects of Nanomaterials and Nanosafety

CAS Center for Excellence in Nanoscience

National Center for Nanoscience and Technology

Beijing 100190, China

E-mail: liangxj@nanoctr.cn

Y. Wang, Prof. X.-J. Liang

University of Chinese Academy of Sciences

Beijing 100049, China

X. Zeng, J. Han, Prof. H.-J. Butt, Prof. S. Wu

Max Planck Institute for Polymer Research

Ackermannweg 10, 55128 Mainz, Germany

Prof. Dr. W. Sun

State Key Laboratory of Fine Chemicals

Dalian University of Technology

2 Linggong Road, Hi-Tech Zone, Dalian 116024, China

Keywords: metallodrugs, photo-responsive, morphological transformation, tumor penetration, zeta potential

Published in Advanced Materials, 2020, 32(43): 2004766.

3.1 Statement of contribution

Si Wu convinced the idea.

Si Wu, Xing-Jie Liang and Hans-Jürgen Butt led the project.

Xiaolong Zeng prepared the materials and did the synthesis.

Xiaolong Zeng and Yufei Wang did the biological experiments.

Jianxiong Han contributed to TEM measurement.

Wen Sun contributed to ESI-MS measurement.

Xiaolong Zeng and Yufei Wang contributed equally to this work.

3.2 Introduction

Cisplatin and various other Pt(II) anticancer drugs are administered to the majority of patients undergoing chemotherapy.[1, 2] The development of drug resistance during chemotherapy treatment is a major problem; cisplatin becomes inefficient in patients after extended use.[3, 4] Cisplatin resistance is due to multiple deactivation pathways that render the treatment inefficient.[1] First, proteins such as serum albumin in blood deactivate cisplatin.[5] Second, cisplatin cannot be efficiently taken up by cisplatin-resistant cancer cells.[6] Third, intracellular biomolecules such as metallothionein (MT) and glutathione (GSH) may strongly bind and sequester cisplatin.[7] Fourth, the DNA of cancer cells that are damaged by cisplatin, can be repaired by proteins.[8] All these deactivation pathways hinder the curative effects of cisplatin.

Some strategies have been developed to overcome the above-mentioned deactivation pathways. For example, Pt(IV) prodrugs, which release cisplatin in cancer cells, have been developed.[9-12] Pt(IV) prodrugs are more resistant to ligand substitution reactions than cisplatin because Pt(IV) centers are saturated and kinetically more inert.[1] Thus, Pt(IV) can minimize unwanted side reactions with biomolecules prior to DNA binding. Another strategy to overcome deactivation is to combine cisplatin with other anticancer agents such as paclitaxel, 5-fluorouracil, gemcitabine or ruthenium complexes.[13-16] Mixtures of anticancer agents possess multiple targets and actions; this strategy strengthens the therapeutic effects via the different anticancer mechanisms of the different agents.[14] A third strategy to overcome deactivation is to use nano-carriers for the delivery of cisplatin.[17, 18] Some nano-carriers can circulate longer in the bloodstream, accumulate at tumor tissue via the enhanced permeation and retention (EPR) effect, be taken up by tumor cells efficiently, and release Pt drugs on demand.[19-22] These properties of nano-carriers can prevent deactivation pathways. Although the

above-mentioned strategies prevented certain deactivation pathways for cisplatin, it is difficult to overcome multiple deactivation pathways. Thus, reversing cisplatin resistance poses a challenge.

Herein, the design of a dual-responsive Pt(IV)/Ru(II) bimetallic polymer PolyPt/Ru to overcome multiple deactivation pathways for cisplatin is reported. We demonstrated the use of PolyPt/Ru for the treatment of cisplatin-resistant tumors in a patient-derived xenograft (PDX) mouse model (**Figure 1**). PolyPt/Ru is an ABA-type triblock polymer with a hydrophobic Pt(IV)/Ru(II) bimetallic block and two hydrophilic poly(ethylene glycol) (PEG) blocks. The Pt(IV) moieties in the hydrophobic block are prodrugs that produce cisplatin in intracellular reduction environments. The Ru(II) moieties were incorporated in the hydrophobic block because some Ru(II) complexes show anticancer activity and have entered clinical trials.[23, 24] In particular, some Ru(II) complexes can generate $^1O_2$ and undergo ligand substitution under light irradiation.[25-30] Photocaged Ru(II) complexes are usually nontoxic to nonirradiated tissues and can become toxic in cancer cells through photoactivation.[24, 29] This photoactivation strategy can improve selectivity in cancer treatment. The Ru(II) moieties in PolyPt/Ru can generate $^1O_2$ for photodynamic therapy (PDT) and release anticancer Ru(II) complexes for photoactivated chemotherapy (PACT). Additionally, we used the hydrophilic and biocompatible PEG block because it can prolong blood circulation and suppress nonspecific adsorption of proteins that deactivate metallodrugs.[31-33] PolyPt/Ru self-assembles into nanoparticles, which accumulate at tumor sites and are taken up by cisplatin-resistant cancer cells, where it releases cisplatin in the reductive microenvironments. Irradiating PolyPt/Ru with red light generates $^1O_2$ and induces degradation of the Ru(II) moieties, and the release of anticancer Ru(II) complexes. The damage caused by the released Ru(II) complexes and $^1O_2$ are different from those

caused by cisplatin, which can eliminate the deactivation pathway via repair.[34] The combination of the released cisplatin and Ru(II) complexes as well as the generated $^1O_2$ has a synergistic effect against cisplatin-resistant tumors. Therefore, PolyPt/Ru can overcome multiple deactivation pathways and reverse cisplatin resistance. Photoactivation of PolyPt/Ru only occurs at the irradiated tumor tissue, which further improves the selectivity of the cancer treatment.

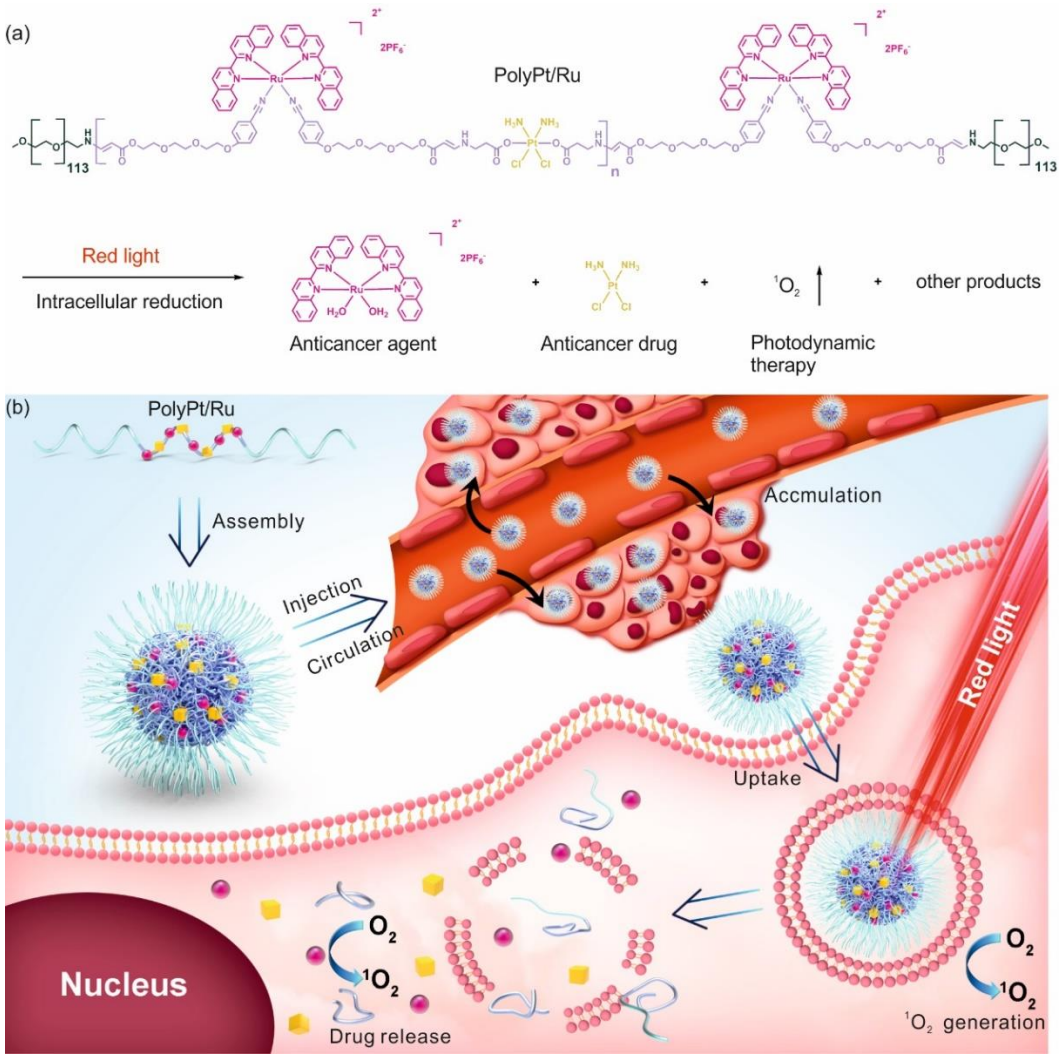

Figure 1. (a) Structure of the amphiphilic triblock copolymer PolyPt/Ru. Red light irradiation and intracellular reduction induced degradation of the polymer, generation of $^1O_2$, and release of the anticancer drug cisplatin and the anticancer agent $[Ru(biq)_2(H_2O)_2](PF_6)_2$ (biq = 2,2'-biquinoline). (b) Schematic illustration of self-

assembly, extracellular and intracellular processes for anticancer therapy using PolyPt/Ru.

3.3 Result and discussion

3.3.1 Synthesis of PolyPt/Ru

To prepare PolyPt/Ru, we synthesized the Ru(II)-containing monomer $[Ru(biq)_2(PCE)_2](PF_6)_2$ (biq = 2,2'-biquinoline, PCE = propiolic acid 2-[2-[2-(4-cyanophenoxy)ethoxy]ethoxy]ethyl ester) (Figure S1) and Pt(IV)-containing monomer precursor $[Pt(NH_3)_2Cl_2(AAE)_2](TFA)_2$ (AAE = 3-aminopropionic acid ester, TFA = trifluoroacetic acid) (Figure S2) via multi-step routes. The monomers and intermediates were fully characterized using nuclear magnetic resonance (NMR) spectroscopy and mass spectrometry (MS) (Figure S4-S15). Subsequently, the Pt(IV)-containing monomer precursor was deprotonated and polymerized with the Ru(II)-containing monomer via spontaneous amino-yne click polymerization (Figure S3, S16). Finally, PolyPt/Ru was synthesized by terminating the polymer with poly(ethylene glycol) methyl ether amine (mPEG5k-NH_2) (Figure S3). NMR spectroscopy and gel permeation chromatography (GPC) demonstrated that PolyPt/Ru was successfully synthesized (Figure S17 and S18). The molar mass of PolyPt/Ru measured by NMR spectroscopy was 17 kg mol^{-1}, which was comparable to that measured by GPC (18 kg mol^{-1}). The weight fraction of the Pt(IV)/Ru(II) block was ~42%, indicating that PolyPt/Ru has a high content of anticancer Pt(IV) and Ru(II) moieties.

3.3.2 Self-assembly of PolyPt/Ru

We prepared the PolyPt/Ru nanoparticles via self-assembly. PolyPt/Ru was dissolved in a THF/DMF mixture. Water was added dropwise to the mixture to trigger the self-assembly. Subsequently, PolyPt/Ru nanoparticles in an aqueous solution were obtained by removing the THF and DMF via dialysis against water. Transmission electron microscopy (TEM) showed that PolyPt/Ru self-assembled into nanoparticles with an average diameter of 90 nm (**Figure 2**a). Dynamic light scattering (DLS) results showed that the PolyPt/Ru nanoparticles had an average hydrodynamic diameter of 111 nm (Figure 2b), which was comparable to the TEM result. The PolyPt/Ru nanoparticles in aqueous solution were stable for 24 h in the dark (Figure S19).

3.3.3 Dual-responsiveness of PolyPt/Ru

The Ru(II) and Pt (IV) moieties in PolyPt/Ru are light- and reduction-responsive, making PolyPt/Ru nanoparticles degradable (Figure 1). We studied the degradation of PolyPt/Ru nanoparticles induced by red light irradiation, GSH treatment, and the combination of red light and GSH treatment using DLS (Figure 2c). The average diameter of the original PolyPt/Ru nanoparticles was 111 nm. After red light irradiation, photoproducts with diameters of 56 nm and 269 nm appeared. This observation suggested that the PolyPt/Ru nanoparticles degraded into smaller-sized fragments, and some larger-sized hydrophobic aggregates of photoproducts. Similar DLS signals were observed when PolyPt/Ru nanoparticles were treated with GSH. When PolyPt/Ru nanoparticles were treated with a combination of light and GSH, the smaller fragments disappeared, and larger aggregates were formed. TEM observations further confirmed that light or GSH treatments resulted in morphological changes (Figure S20).

We also performed GPC measurements in a good solvent (DMF), to analyze the degraded products (Figure 2d). The hydrophobic products were easily dissolved in DMF to detect the degraded fragments through GPC. The PolyPt/Ru polymer eluted earlier than the relative degradation products. The delay in the retention time of the products indicated the formation of a series of low-molecular-weight fragments, which confirmed that light and GSH degraded PolyPt/Ru. In addition, UV-vis absorption spectroscopy showed that photosubstitution of the Ru(II) moieties occurred when the PolyPt/Ru nanoparticles were irradiated with red light in the presence or absence of GSH (Figure S21). Irradiating PolyPt/Ru nanoparticles in the presence of GSH resulted in a faster reaction. This observation indicated that the degradation of Pt(IV) moieties using GSH promoted the photoreactivity of the Ru(II) moieties in the PolyPt/Ru nanoparticles (Figure S22).

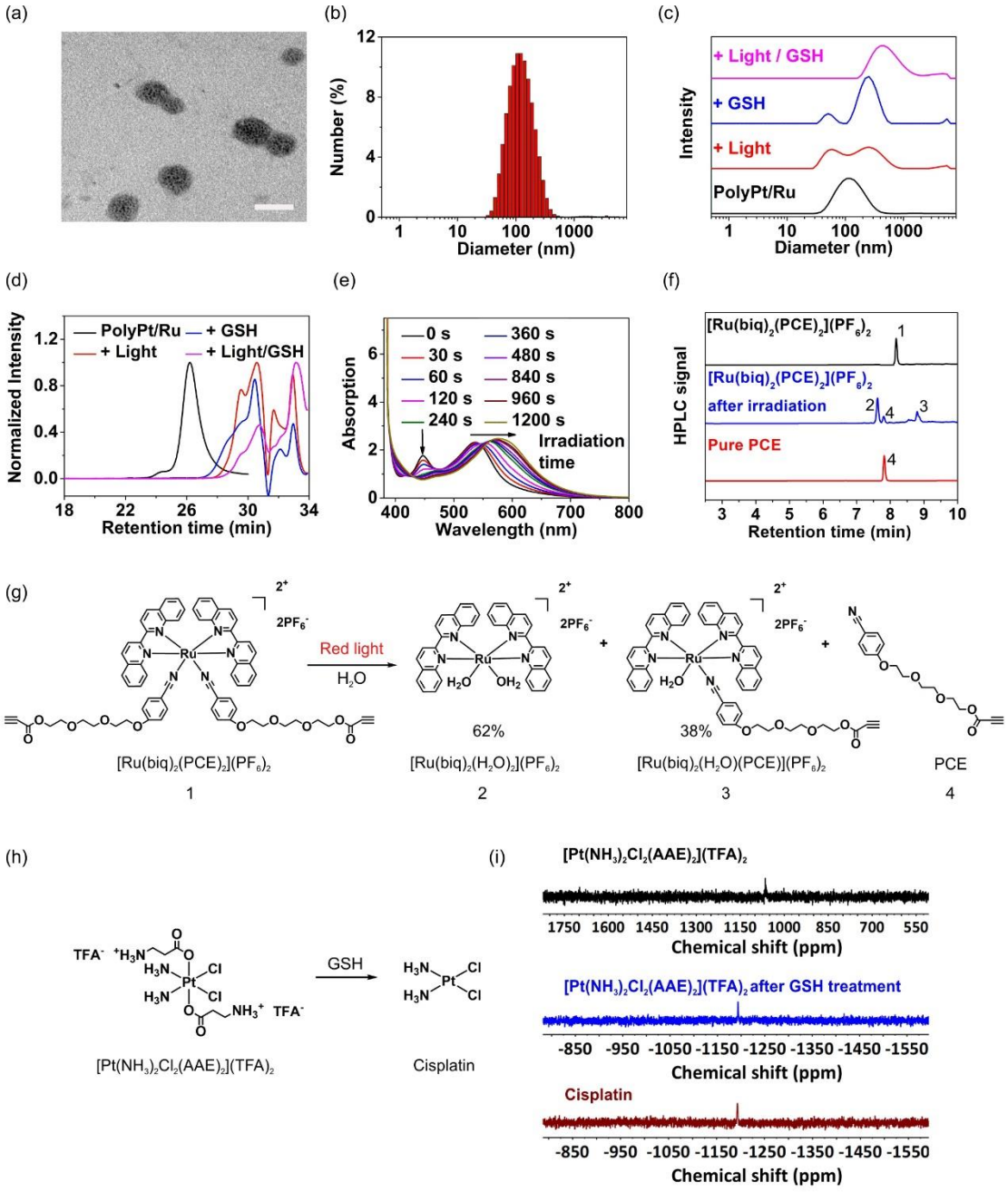

Figure 2. (a) A TEM image of PolyPt/Ru nanoparticles. Scale bar: 100 nm. (b) The diameter of PolyPt/Ru nanoparticles measured by dynamic light scattering (DLS). (c) DLS measurements of PolyPt/Ru nanoparticles. + Light: PolyPt/Ru nanoparticles after light irradiation (671 nm, 125 mW cm^{-2}, 20 min); + GSH (glutathione): PolyPt/Ru nanoparticles after GSH treatment (5.0 mM, 4 h); + Light/GSH: PolyPt/Ru nanoparticles after light irradiation (671 nm, 125 mW cm^{-2}, 20 min) with GSH treatment (5.0 mM, 4 h). (d) GPC traces of PolyPt/Ru. + Light: PolyPt/Ru after light irradiation (671 nm, 125 mW cm^{-2}, 20 min); + GSH: PolyPt/Ru after GSH treatment (5.0 mM, 4 h); + Light/GSH: PolyPt/Ru after light irradiation (671 nm, 125 mW cm^{-2}, 20 min) with GSH treatment (5.0 mM, 4 h). (e) UV-vis absorption spectra of $[Ru(biq)_2(PCE)_2](PF_6)_2$ under light irradiation (671 nm, 125 mW cm^{-2}) over time. (f) Photosubstitution of $[Ru(biq)_2(PCE)_2](PF_6)_2$ studied by high-performance liquid

chromatography (HPLC). $[Ru(biq)_2(PCE)_2](PF_6)_2$ was irradiated using 671 nm light (125 mW cm^{-2}, 20 min). (g) Scheme for the photosubstitution of $[Ru(biq)_2(PCE)_2](PF_6)_2$. (h) Scheme for the reduction of $[Pt(NH_3)_2Cl_2(AAE)_2](TFA)_2$. (i) ^{195}Pt NMR spectra of $[Pt(NH_3)_2Cl_2(AAE)_2](TFA)_2$, $[Pt(NH_3)_2Cl_2(AAE)_2](TFA)_2$ after GSH treatment (5.0 mM, 4 h), and pure cisplatin.

The TEM, DLS, GPC and UV-vis absorption spectroscopy results demonstrated the qualitative degradation of PolyPt/Ru. PolyPt/Ru degradation is difficult to quantify because the products are complex mixtures. Therefore, $[Ru(biq)_2(PCE)_2](PF_6)_2$ and $[Pt(NH_3)_2Cl_2(AAE)_2](TFA)_2$ were used as model compounds to investigate the reaction mechanism. UV-vis spectroscopy was used to study the photosubstitution of $[Ru(biq)_2(PCE)_2](PF_6)_2$ (Figure 2e). Red light irradiation of $[Ru(biq)_2(PCE)_2](PF_6)_2$ red-shifted the metal-to-ligand charge transfer (MLCT) band from 535 nm (λ_{max} of $[Ru(biq)_2(PCE)_2](PF_6)_2$) to 586 nm ($\lambda_{max}$ of $[Ru(biq)_2(H_2O)_2](PF_6)_2$). The spectral change was achieved within 20 min, suggesting the efficient photosubstitution of $[Ru(biq)_2(PCE)_2](PF_6)_2$. High-performance liquid chromatography (HPLC) was then performed to quantify the photosubstitution of $[Ru(biq)_2(PCE)_2](PF_6)_2$ (Figure 2f). $[Ru(biq)_2(PCE)_2](PF_6)_2$ is represented by the signal peak, **1**. After 671 nm light irradiation (125 mW cm^{-2}, 20 min), peak **1** disappeared, and three new peaks, the photoproducts, appeared. Comparing the retention time of the photoproducts with pure PCE ligand confirmed that peak **4** was the PCE. Furthermore, according to the UV-vis absorption spectroscopy detector in the HPLC system, peaks **2** and **3** could be assigned to $[Ru(biq)_2(H_2O)_2](PF_6)_2$ and $[Ru(biq)_2(PCE)(H_2O)](PF_6)_2$, respectively (Figure S23). The contents of $[Ru(biq)_2(H_2O)_2](PF_6)_2$ and $[Ru(biq)_2(PCE)(H_2O)](PF_6)_2$ were 62% and 38%, which showed that most of the PCE ligands were cleaved from $[Ru(biq)_2(PCE)_2](PF_6)_2$ via red light irradiation (Figure 2g).

The reduction-responsiveness mechanism of $[Pt(NH_3)_2Cl_2(AAE)_2](TFA)_2$ was investigated using ^{195}Pt NMR spectroscopy (Figure 2h, i). The chemical shift of $[Pt(NH_3)_2Cl_2(AAE)_2](TFA)_2$ was located at 1067.1 ppm. The chemical shifts of both cisplatin and the reductive product were located at −1194.7 ppm, suggesting that the reductive product was cisplatin. The ^{195}Pt NMR results showed that $[Pt(NH_3)_2Cl_2(AAE)_2](TFA)_2$ produced cisplatin via GSH treatment.

3.3.4 In vitro cytotoxicity against drug resistant cancer cells

Cisplatin released from PolyPt/Ru can inhibit cancer cell growth. The half-maximal inhibitory concentration (IC_{50}) values of cisplatin for the sensitive A549 and BEL-7404 cancer cells were as low as 16.10 and 5.68 μg/mL, respectively (Table 1). These results showed that cisplatin efficiently inhibited the growth of sensitive cancer cells. However, the IC_{50} values of cisplatin for the resistant A549-DDP and 7404-CP20 cancer cells were an order of magnitude higher (Table 1), which indicates that cisplatin is ineffective against resistant cancer cells.

Furthermore, we studied the anticancer performance of $[Pt(NH_3)_2Cl_2(AAE)_2](TFA)_2$, which can produce cisplatin under intracellular reduction environments. The IC_{50} values of $[Pt(NH_3)_2Cl_2(AAE)_2](TFA)_2$ for the sensitive A549 and BEL-7404 cells, and the resistant A549-DDP and 7404-CP20 cells were 41%, 14%, 58%, and 54% lower than those of cisplatin (Table 1), respectively. This indicates that $[Pt(NH_3)_2Cl_2(AAE)_2](TFA)_2$ can inhibit both sensitive and resistant cancer cells more efficiently than cisplatin.

Table 1. Half-maximal inhibitory concentration (IC_{50}) values of cisplatin, $[Pt(NH_3)_2Cl_2(AAE)_2](TFA)_2$ and $[Ru(biq)_2(H_2O)_2](PF_6)_2$ (Figure S24).

Cell line	Cisplatin IC_{50}[a)]	$Pt(NH_3)_2Cl_2(AAE)_2(TFA)_2$ IC_{50}	$[Ru(biq)_2(H_2O)_2](PF_6)_2$		
			IC_{50}, dark	IC_{50}, light	PI[c)]
sensitive A549	16.10 (0.92)	9.38 (0.99) [d)]	3.66 (1.02)	2.72 (0.93)	1.34
sensitive BEL-7404	5.68 (0.86)	4.89 (0.93)	2.97 (0.93)	0.68 (0.19)	4.36
cisplatin-resistant A549-DDP[b)]	100.1 (3.46)	41.80 (0.72)	19.70 (0.94)	5.99 (0.97)	3.28
cisplatin-resistant 7404-CP20[b)]	77.30 (0.96)	35.10 (1.00)	28.70 (1.11)	8.87 (1.09)	3.23

[a)] The IC_{50} unit is μg/mL. [b)] Resistance factor (RF) against cisplatin, defined as IC_{50} (resistant cell) against cisplatin / IC_{50} (sensitive cell) against cisplatin. The RF of A549-DDP and 7404-CP20 cells was 6.21 and 13.60, respectively. [c)] Phototoxicity index (PI), defined as IC_{50}, dark / IC_{50}, light. [d)] Standard error of each independent experiment.

$[Ru(biq)_2(H_2O)_2](PF_6)_2$ released from PolyPt/Ru has anticancer activity against sensitive cancer cells.[35] Its anticancer activity is enhanced via photoirradiation because of $^1O_2$ generation (Figure S25).[35] Here, we compared its activity against sensitive and resistant cells. In the dark, the IC_{50} values of $[Ru(biq)_2(H_2O)_2](PF_6)_2$ for the sensitive A549 and BEL-7404 cells were 3.66 and 2.97 μg/mL, respectively (Table 1). Upon red light irradiation, the IC_{50} values of $[Ru(biq)_2(H_2O)_2](PF_6)_2$ for the sensitive cells were as low as 2.72 and 0.68 μg/mL; the anticancer efficacy of $[Ru(biq)_2(H_2O)_2](PF_6)_2$ against the sensitive cells was enhanced via photoirradiation because of $^1O_2$ generation. Furthermore, the IC_{50} values of $[Ru(biq)_2(H_2O)_2](PF_6)_2$ for the resistant A549-DDP and 7404-CP20 cells were 19.70 and 28.70 μg/mL in the dark (Table 1). Upon red light irradiation, the IC_{50} values of $[Ru(biq)_2(H_2O)_2](PF_6)_2$ for the resistant cells were as low as 5.99 and 8.87 μg/mL, respectively. The IC_{50} values of $[Ru(biq)_2(H_2O)_2](PF_6)_2$ for A549-DDP and 7404-CP20 after photoirradiation were 70% and 69% lower than those

in the dark, respectively. This demonstrated that $[Ru(biq)_2(H_2O)_2](PF_6)_2$ exhibited enhanced anticancer activity against resistant cancer cells.

3.3.5 Cellular uptake and in vitro cytotoxicity assessment

The anticancer efficacy of $[Pt(NH_3)_2Cl_2(AAE)_2](TFA)_2$ and $[Ru(biq)_2(H_2O)_2](PF_6)_2$ encouraged us to deliver PolyPt/Ru nanoparticles into cisplatin-resistant cancer cells. We studied the uptake of PolyPt/Ru nanoparticles by cisplatin-resistant cancer cells. Both resistant A549-DDP and 7404-CP20 cells were incubated with PolyPt/Ru nanoparticles for 6 h in the dark. Subsequently, confocal laser scanning microscopy (CLSM) images were taken at 4 h and 6 h. The observation of red fluorescence indicated that PolyPt/Ru nanoparticles were efficiently taken up by both resistant cancer cells (**Figure 3**a, b and Figure S27, 28). Flow cytometry was used to quantitatively analyze the uptake efficiency of PolyPt/Ru nanoparticles (Figure S26). After incubation for 6 h, the uptake efficiencies for A549-DDP and 7404-CP20 cells were 76.4% and 54.4%, respectively. These results demonstrated that PolyPt/Ru nanoparticles were efficiently taken up by the cisplatin-resistant cells.

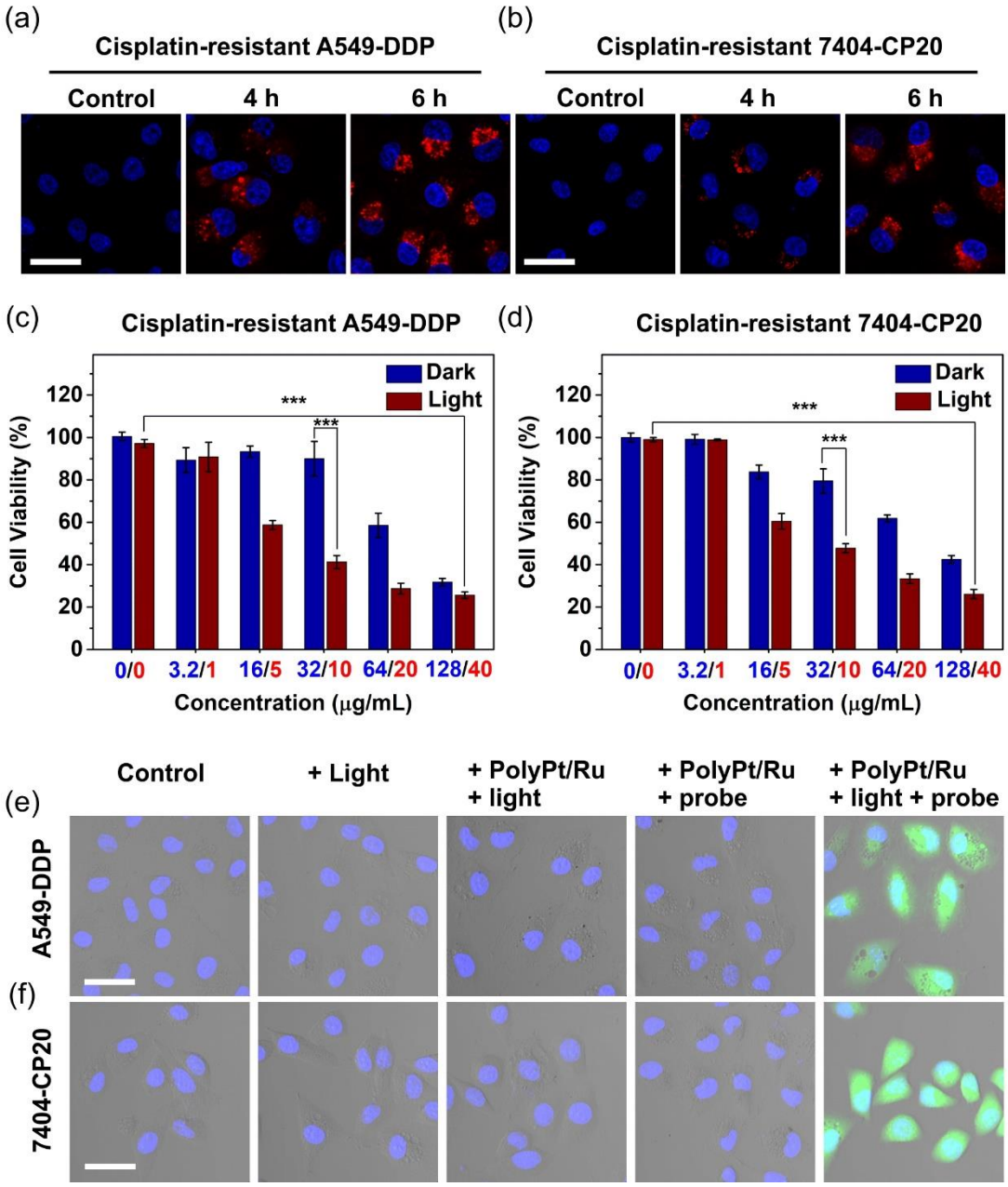

Figure 3. (a) and (b) Confocal laser scanning microscopy (CLSM) images of PolyPt/Ru nanoparticles (red) after incubation with cisplatin-resistant A549-DDP (a) and 7404-CP20 (b) cancer cells for different time periods. Nuclei were stained with Hoechst 33343 (blue). Scale bars: 25 μm. (c) and (d) Viability of cisplatin-resistant A549-DDP (c) and 7404-CP20 (d) cancer cells treated with equivalent Ru(II) and Pt(IV) concentrations in the nanoparticles in the dark and under light irradiation. The equivalent Ru(II) concentration was shown in blue color and the equivalent Pt(IV) concentration was shown in red color. The cells were irradiated with 671 nm red light (125 mW cm^{-2}, 20 min) after incubation with PolyPt/Ru nanoparticles for 6 h. Cell viability was tested after the cells were further incubated in the dark for 24 h. (e) and (f) Generation of intracellular $^1O_2$ in A549-DDP and 7404-CP20 cells as observed by CLSM. The cells were divided into five groups: control group; + light group: cancer cells irradiated with light (671 nm light, 125 mW cm^{-2}, 1 min); +PolyPt/Ru + light

group: cancer cells with PolyPt/Ru nanoparticles and light irradiation (671 nm light, 125 mW cm^{-2}, 1 min); +PolyPt/Ru + probe group: cancer cells with PolyPt/Ru nanoparticles and the $^1O_2$ probe; +PolyPt/Ru + light + probe group: cancer cells with PolyPt/Ru nanoparticles, $^1O_2$ probe, and light irradiation (671 nm light, 125 mW cm^{-2}, 1 min). Nuclei were stained with DAPI (blue). $^1O_2$ was detected using the indicator DCFH-DA (green). Scale bars: 50 μm.

We then investigated the anticancer performance of PolyPt/Ru nanoparticles against cisplatin-resistant cells (Figure 3c, d). In the dark, the cell viabilities decreased as the concentration of the nanoparticles increased. When the equivalent Ru(II) and Pt(IV) concentrations in the nanoparticles were 128 and 40 μg/mL, the cell viabilities decreased to 31% and 42% for the A549-DDP and 7404-CP20 cells, respectively. We infer that the decrease in cell viability occurred because cisplatin was produced via the reduction of the Pt(IV) moieties in PolyPt/Ru. Moreover, light irradiation further decreased the viability of the cancer cells (Figure 3c, d). The enhanced cytotoxicity was attributed to $^1O_2$ generated and $[Ru(biq)_2(H_2O)_2](PF_6)_2$ released (Figure S28). The generation of $^1O_2$ in resistant A549-DDP and 7404-CP20 cells was detected using a green fluorescent probe (Figure 3e, f). No green fluorescence was observed in the absence of PolyPt/Ru nanoparticles, the probe, or light irradiation. However, green fluorescence was observed when the cells with PolyPt/Ru nanoparticles and the probe were irradiated with red light. Additionally, the cytotoxicity caused by the release of cisplatin and $[Ru(biq)_2(H_2O)_2](PF_6)_2$, along with the generated $^1O_2$ was notable (Figure S29). Their synergistic effects reversed cisplatin resistance (Figure S30, 31).

3.3.6 In vivo anticancer assessment

Encouraged by the anticancer efficacy of PolyPt/Ru nanoparticles *in vitro*, we studied the anticancer efficacy of PolyPt/Ru nanoparticles *in vivo*. Hemolysis analysis indicated

that PolyPt/Ru nanoparticles have good blood compatibility (Figure S32). We then investigated the anticancer performance of PolyPt/Ru nanoparticles using a hepatic patient-derived cancer xenograft (PDX) mouse model. PDX models are vastly similar to patient tumors because the tumor tissue is taken from patients and grown in physiologically relevant tumor microenvironments.[36, 37] PDX models have been applied in molecular and genetic investigations of drug resistance in previous studies.[38-40]

To study the accumulation of nanoparticles, a PDX tumor-bearing mouse was intravenously injected with PolyPt/Ru nanoparticles from the tail vein. Fluorescence images of the mouse model (right) and a control mouse (left) were taken over time after injection (**Figure 4**a). No signal and a weak signal were observed at 0 and 4 h in the mouse model, respectively. The fluorescence from PolyPt/Ru nanoparticles at the tumor site reached a maximum at 12 h, which indicated that PolyPt/Ru nanoparticles efficiently accumulated at the tumor site. The fluorescence intensity at 24 h became weaker, suggesting that the nanoparticles were cleared through metabolism. In contrast, the control mouse injected with saline showed no fluorescence, which proved that the fluorescence was produced by the injected nanoparticles. These experiments demonstrated that PolyPt/Ru nanoparticles accumulate at the tumor site, which we deduced was due to the well-known EPR effect.

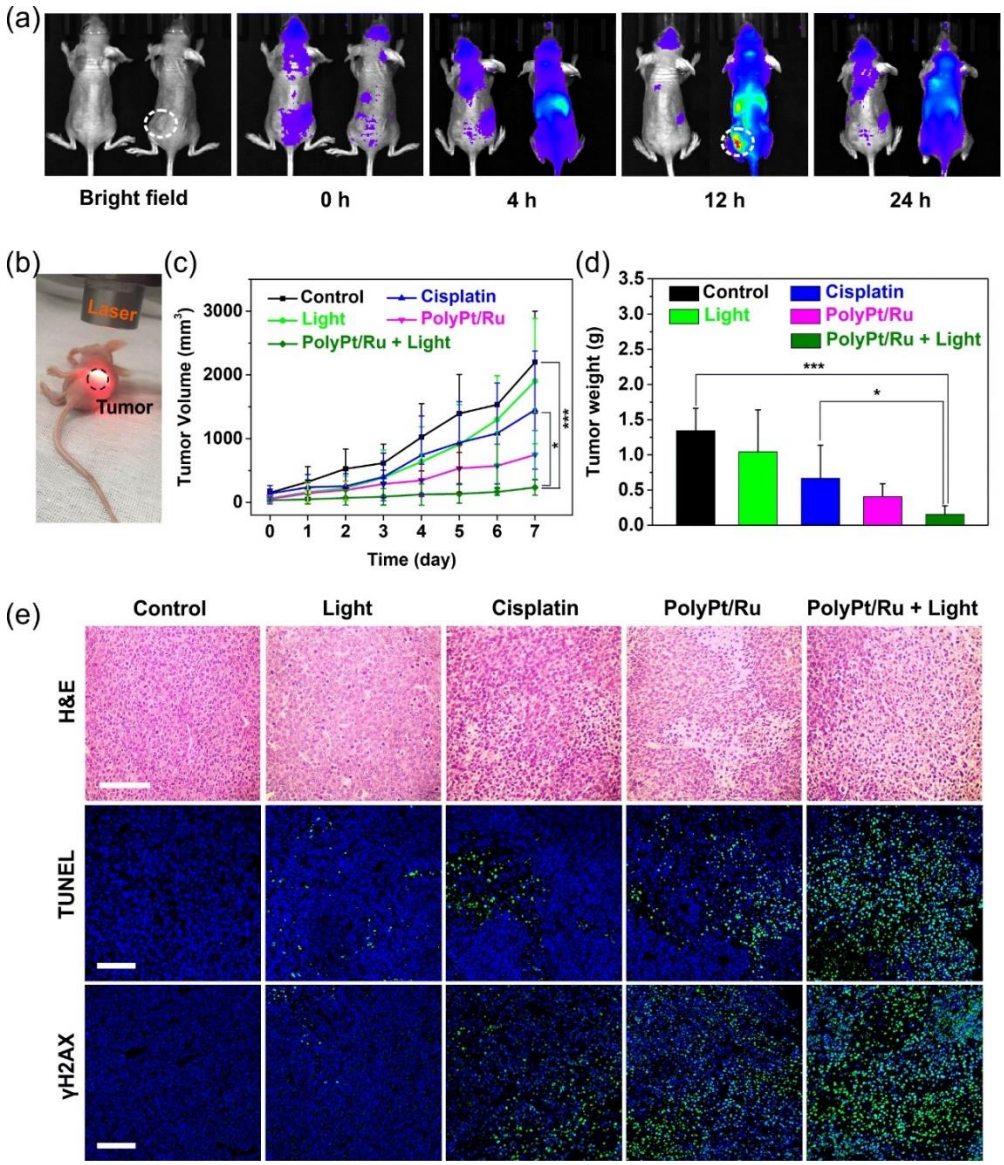

Figure 4. (a) Fluorescence images of PDX tumor-bearing mice after intravenous injection of saline (left, control) and PolyPt/Ru nanoparticles (right). Images were taken after injection for 0, 4, 12 and 24 h. The dashed circle indicates the tumor. (b) A photograph shows red light irradiation on a mouse model. (c) Tumor volumes of PDX tumor-bearing mice during different treatments. (d) Average tumor weights at day 7 after different treatments. (e) H&E, TUNEL, and γH2AX staining of tumor sections isolated from the mice on day 7. The damaged DNA strands and γH2AX were labelled by FITC (green). Cell nuclei were stained with DAPI (blue). Scale bars: 100 μm.

Twelve hours after PolyPt/Ru nanoparticles were intravenously injected into the mouse model, the tumor was irradiated with a 671 nm laser for 20 min (PolyPt/Ru + light group). Four additional experiments were conducted for comparison: 1) PDX

tumor-bearing mice were injected with saline (Control Group); 2) PDX tumor-bearing mice were irradiated with light (Light Group); 3) PDX tumor-bearing mice were injected with an equivalent dosage of cisplatin (Cisplatin Group), and 4) PDX tumor-bearing mice were injected with PolyPt/Ru nanoparticles (PolyPt/Ru Group). We compared the anticancer efficacy by monitoring the tumor volumes of each group over 7 days (Figure 4c). The tumor volume in the control group increased by ~30 times. The result of the light group was similar to that of the control group, indicating that mild light irradiation does not have an inhibitory effect (Figure S33, 34). Cisplatin treatment caused a tumor growth of ~13 times, since PDX tumors are resistant to cisplatin. For the PolyPt/Ru group, the increase in the tumor volume was smaller (~8 times) than those in the previous groups. This result indicated that the Pt(IV) moieties in PolyPt/Ru contributed to tumor inhibition. Compared to the four groups mentioned above, tumor growth in the PolyPt/Ru + light group was notably inhibited. This result suggests that the synergistic effects of this treatment improved the anticancer performance.

Subsequently, the mice were euthanized, and the tumors were isolated for analysis (Figure S36). The average tumor weight in the PolyPt/Ru + light group was much lighter than that in the other four groups (Figure 4d). Immunohistochemical analyses were also performed to illustrate the mechanism of the anticancer activity using PolyPt/Ru nanoparticles (Figure 4e). A hematoxylin and eosin (H&E) staining assay showed large areas of apoptosis and necrosis, which suggested that the PolyPt/Ru + light group treatment exhibited considerable tumor inhibition. Similar results were observed in TUNEL staining images. Furthermore, the γH2AX staining assay provided more insight into the anticancer mechanism since γH2AX is a sensitive marker for DNA damage (Figure S35). Comparing γH2AX formation at tumor sites, we found that enhanced genomic DNA damage appeared in the PolyPt/Ru + light group. We

hypothesized that the released anticancer agents induced DNA damage, which increased genomic instability and apoptosis. Once DNA damage occurs, γH2AX forms clusters near the impaired DNA strands.

We also investigated the systemic toxicity during the treatments by comparing the H&E staining images of the main organs (heart, liver, lung, spleen, and kidney) (Figure S38). Negligible pathological alteration of the organs was observed, indicating the low systemic toxicity of PolyPt/Ru. The body weights of the mice did not change significantly during the treatments (Figure S39), which suggests that the treatments had minimal side effects. The combined results demonstrate that the use of PolyPt/Ru can treat PDX tumors with improved efficacy and minimized systemic toxicity.

3.4 Conclusions

In conclusion, we synthesized a dual-responsive, bimetallic polymer, PolyPt/Ru, to overcome multiple deactivation pathways for cisplatin. PolyPt/Ru showed excellent performance against cisplatin-resistant tumors due to the design of the polymer structure, and the synergistic effects of the bimetallic moieties. Cisplatin resistance in a PDX model was reversed using PolyPt/Ru. Our study revealed that the design of multi-metallic polymers with multi-responsiveness is a new strategy to treat drug-resistant cancers. Since many bioactive metal complexes exist, the design principles reported here provide a foundation for the design of multi-metallic polymers for biomedical applications. We anticipate that more multi-metallic polymers with adjustable functions can be developed for personalized nanomedicine and enhanced clinical effectiveness.

3.5 References

[1] T. C. Johnstone, K. Suntharalingam, S. J. Lippard, *Chem. Rev.* **2016**, *116*, 3436.

[2] W. Zhang, J. Shen, H. Su, G. Mu, J.-H. Sun, C.-P. Tan, X.-J. Liang, L.-N. Ji, Z.-W. Mao, *ACS Appl. Mater. Interfaces* **2016**, *8*, 13332.

[3] X.-J. Liang, H. Meng, Y. Wang, H. He, J. Meng, J. Lu, P. C. Wang, Y. Zhao, X. Gao, B. Sun, *Proc. Natl. Acad. Sci. USA* **2010**, *107*, 7449.

[4] M. D. Hall, M. Okabe, D.-W. Shen, X.-J. Liang, M. M. Gottesman, *Annu. Rev. Pharmacol. Toxicol.* **2008**, *48*, 495.

[5] G. Ferraro, L. Massai, L. Messori, A. Merlino, *Chem. Commun.* **2015**, *51*, 9436.

[6] S. Li, C. Li, S. Jin, J. Liu, X. Xue, A. S. Eltahan, J. Sun, J. Tan, J. Dong, X.-J. Liang, *Biomaterials* **2017**, *144*, 119.

[7] Y. Min, C. Q. Mao, S. Chen, G. Ma, J. Wang, Y. Liu, *Angew. Chem., Int. Ed.* **2012**, *124*, 6846.

[8] J. Hu, J. D. Lieb, A. Sancar, S. Adar, *Proc. Natl. Acad. Sci. USA* **2016**, *113*, 11507.

[9] Z. Wang, Z. Xu, G. Zhu, *Angew. Chem., Int. Ed.* **2016**, *55*, 15564.

[10] W. H. Ang, I. Khalaila, C. S. Allardyce, L. Juillerat-Jeanneret, P. J. Dyson, *J. Am. Chem. Soc.* **2005**, *127*, 1382.

[11] X. Ling, X. Chen, I. A. Riddell, W. Tao, J. Wang, G. Hollett, S. J. Lippard, O. C. Farokhzad, J. Shi, J. Wu, *Nano Lett.* **2018**, *18*, 4618.

[12] M. Stilgenbauer, A. M. Jayawardhana, P. Datta, Z. Yue, M. Gray, F. Nielsen, D. J. Bowers, H. Xiao, Y.-R. Zheng, *Chem. Commun.* **2019**, *55*, 6106.

[13] Y. H. Kim, S. W. Shin, B. S. Kim, J. H. Kim, J. G. Kim, Y. J. Mok, C. S. Kim, H. S. Rhyu, J. H. Hyun, J. S. Kim, *Cancer* **1999**, *85*, 295.

[14] J. Karges, T. Yempala, M. Tharaud, D. Gibson, G. Gasser, *Angew. Chem., Int. Ed.* **2020**, *59*, 7069.

[15] M. Michalak, M. S. Lach, M. Antoszczak, A. Huczyński, W. M. Suchorska, *Molecules* **2020**, *25*, 537.

[16] Y. Zheng, D. Y. Zhang, H. Zhang, J. J. Cao, C. P. Tan, L. N. Ji, Z. W. Mao, *Chem. Eur. J.* **2018**, *24*, 18971.

[17] R. K. Pathak, S. Dhar, *J. Am. Chem. Soc.* **2015**, *137*, 8324.

[18] Z.-T. Cao, Z.-Y. Chen, C.-Y. Sun, H.-J. Li, H.-X. Wang, Q.-Q. Cheng, Z.-Q. Zuo, J.-L. Wang, Y.-Z. Liu, Y.-C. Wang, *Biomaterials* **2016**, *94*, 9.

[19] R. Xing, Q. Zou, C. Yuan, L. Zhao, R. Chang, X. Yan, *Adv. Mater.* **2019**, *31*, 1900822.

[20] J. Li, D. Cui, Y. Jiang, J. Huang, P. Cheng, K. Pu, *Adv. Mater.* **2019**, *31*, 1905091.

[21] M. Abbas, Q. Zou, S. Li, X. Yan, *Adv. Mater.* **2017**, *29*, 1605021.

[22] X. Xu, P. E. Saw, W. Tao, Y. Li, X. Ji, S. Bhasin, Y. Liu, D. Ayyash, J. Rasmussen, M. Huo, *Adv. Mater.* **2017**, *29*, 1700141.

[23] L. Zeng, P. Gupta, Y. Chen, E. Wang, L. Ji, H. Chao, Z.-S. Chen, *Chem. Soc. Rev.* **2017**, *46*, 5771.

[24] C. Mari, V. Pierroz, S. Ferrari, G. Gasser, *Chem. Sci.* **2015**, *6*, 2660.

[25] L. N. Lameijer, T. G. Brevé, V. H. van Rixel, S. H. Askes, M. Siegler, S. Bonnet, *Chem. Eur. J.* **2018**, *24*, 2709.

[26] W. Sun, R. Thiramanas, L. D. Slep, X. Zeng, V. Mailänder, S. Wu, *Chem. Eur. J.* **2017**, *23*, 10832.

[27] G. Carrone, L. Zayat, L. D. Slep, R. Etchenique, *Phys. Chem. Chem. Phys.* **2017**, *19*, 2140.

[28] L. Zayat, C. Calero, P. Alborés, L. Baraldo, R. Etchenique, *J. Am. Chem. Soc.* **2003**, *125*, 882.

[29] L. N. Lameijer, D. Ernst, S. L. Hopkins, M. S. Meijer, S. H. Askes, S. E. Le Dévédec, S. Bonnet, *Angew. Chem., Int. Ed.* **2017**, *129*, 11707.

[30] M. H. Al-Afyouni, T. N. Rohrabaugh, K. F. Al-Afyouni, C. Turro, *Chem. Sci.* **2018**, *9*, 6711.

[31] P. del Pino, F. Yang, B. Pelaz, Q. Zhang, K. Kantner, R. Hartmann, N. Martinez de Baroja, M. Gallego, M. Möller, B. B. Manshian, *Angew. Chem., Int. Ed.* **2016**, *128*, 5573.

[32] A. Salvati, A. S. Pitek, M. P. Monopoli, K. Prapainop, F. B. Bombelli, D. R. Hristov, P. M. Kelly, C. Åberg, E. Mahon, K. A. Dawson, *Nat. Nanotechnol.* **2013**, *8*, 137.

[33] J. Chen, J. Ding, Y. Wang, J. Cheng, S. Ji, X. Zhuang, X. Chen, *Adv. Mater.* **2017**, *29*, 1701170.

[34] B. S. Howerton, D. K. Heidary, E. C. Glazer, *J. Am. Chem. Soc.* **2012**, *134*, 8324.

[35] W. Sun, S. Li, B. Häupler, J. Liu, S. Jin, W. Steffen, U. S. Schubert, H. J. Butt, X. J. Liang, S. Wu, *Adv. Mater.* **2017**, *29*, 1603702.

[36] Y. Cong, H. Xiao, H. Xiong, Z. Wang, J. Ding, C. Li, X. Chen, X. J. Liang, D. Zhou, Y. Huang, *Adv. Mater.* **2018**, *30*, 1706220.

[37] L. Rao, G. T. Yu, Q. F. Meng, L. L. Bu, R. Tian, L. S. Lin, H. Deng, W. Yang, M. Zan, J. Ding, *Adv. Funct. Mater.* **2019**, *29*, 1905671.

[38] K.-T. Kim, H. W. Lee, H.-O. Lee, S. C. Kim, Y. J. Seo, W. Chung, H. H. Eum, D.-H. Nam, J. Kim, K. M. Joo, *Genome biol.* **2015**, *16*, 127.

[39] C. A. Stewart, C. M. Gay, Y. Xi, S. Sivajothi, V. Sivakamasundari, J. Fujimoto, M. Bolisetty, P. M. Hartsfield, V. Balasubramaniyan, M. D. Chalishazar, *Nat. Cancer* **2020**, *1*, 423.

[40] O. Poirion, X. Zhu, T. Ching, L. X. Garmire, *Nat. Commun.* **2018**, *9*, 4892.

3.6 Supporting Information

Materials

$RuCl_3 \bullet xH_2O$ (99.9%), 2,2'-biquinoline (98%), cis-diammineplatinum(II) dichloride (95%), 4-hydroxybenzonitrile (98%), 2-[2-(2-chloroethoxy)ethoxy]ethanol (96%), propiolic acid (95%), potassium tetrachloroplatinate(II) (98%), sodium hexachloroplatinate(IV) hexahydrate (98%), 1,3-diphenyliso benzofuran (DPBF) (97%) were purchased from Sigma-Aldrich. Boc-β-alanine (99%), N,N'-dicyclohexylcarbodiimide (DCC) (99%) , potassium hexafluorophosphate (98%), silver hexafluorophosphate (98%) were purchased from Alfa Aesar. Poly(ethylene glycol) methyl ether amine (mPEG5k-NH_2) was purchased from Creative PEGWorks. 1,1'-dioctadecyl-3,3,3',3'-tetramethylindodicarbocyanine, 4-chlorobenzenesulfonate salt (DiD fluorescent dye) was purchased form Thermo Fisher Scientific. PBS buffer with a pH of 7.4 was purchased from Life Technologies. All other solvents (HPLC grade) were purchased from Sigma-Aldrich or Fisher Scientific. Milli-Q water with a resistivity of 18.2 MΩ·cm was used in this study. Dialysis tubing (3.5K MWCO) was purchased from SERVA Electrophoresis GmbH, Germany.

Instruments and Characterization

^1H nuclear magnetic resonance (^1H NMR), ^{13}C nuclear magnetic resonance (^{13}C NMR) and ^1H -^1H correlation spectroscopy (COSY) were recorded on a 250 or 300 MHz Bruker Spectrospin NMR spectrometer at 25 ℃. ^{195}Pt nuclear magnetic resonance (^{195}Pt NMR) spectra were recorded on a 500 MHz Bruker Spectrospin NMR spectrometer at 25 ℃. The chemical shift (δ) was externally referenced using K_2PtCl_4 for Pt(II) complexes and Na_2PtCl_6 for Pt(IV) complexes. The molecular weights and molecular

weight distributions of the polymers were determined using a PSS-WinGPC (pump: SECcurity) equipped with UV and RI detectors running in dimethylformamide (DMF) with 1g/L LiBr at 50 °C calibrated against polystyrene standards. HPLC analysis was performed on an Agilent HPLC system equipped with a 1100 Series Quaternary pump, a 1200 Series diode detector, and a Merck Chromolith Performance RP18e 100-3 mm HPLC column. UV-vis detector in the HPLC system was set at 260 nm for analysis. UV-vis absorption spectra were measured on a Lambda 900 spectrometer (Perkin Elmer). Fluorescence spectra were recorded on a TIDAS II spectrometer (J&M). Transmission electron microscopy (TEM) images were taken on a Hitachi HT7700 Transmission Electron Microscope. The diameters of the nanoparticles were determined by dynamic light scattering (DLS) on a Nano ZS90 particle size analyzer, Malvern (UK). A DPSS laser with a wavelength of λ= 671 nm (CNI-671-200-LN-AC-3, Laser 2000 GmbH, Germany) was used to induce photoreactions of $[Ru(biq)_2(PCE)_2](PF_6)_2$ and PolyPt/Ru nanoparticles. The laser was equipped with a thermoelectric cooling system. The output power of the laser was controlled by a tabletop laser driver (PSU-III-FDA, Changchun New Industries Optoelectronics Technology Co., Ltd., China) and measured using an optical power meter (model 407A, Spectra-Physics Corporation). A laser at 671 nm was employed as the light source for *in vitro* and *in vivo* experiments. The output power of the laser was controlled by a fiber coupled laser system (FC-671-1W, Changchun New Industries Optoelectronics Technology) and measured by a power meter (LP100/TS15, Changchun New Industries Optoelectronics Technology).

Synthesis

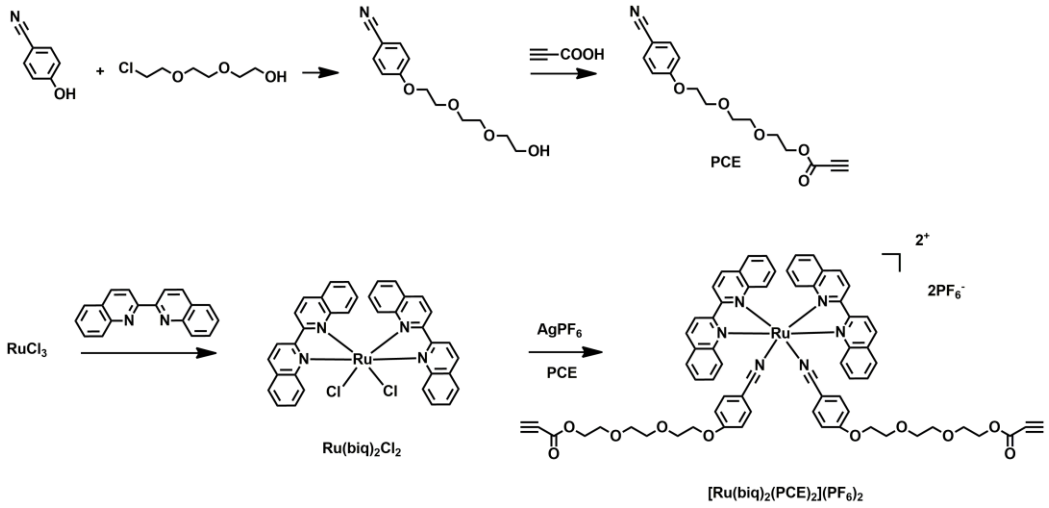

Figure S1. Synthetic route of $[Ru(biq)_2(PCE)_2](PF_6)_2$.

Synthesis of [2-[2-(2-hydroxyethoxy)ethoxy]ethoxy]benzonitrile (Figure S1)

A DMF (20 mL) solution containing 4-hydroxybenzonitrile (1.19 g, 10.00 mmmol), K_2CO_3 (1.38 g, 10.00 mmmol) and KI (100 mg, 0.60 mmmol) was heating to 110 ℃ for 30 min. Subsequently, 2-[2-(2-chloroethoxy)ethoxy]ethanol (1.85 g, 11.00 mmmol) in 10 mL DMF was added dropwise to the aforementioned mixture and stirred at 110 ℃ for 24 h. After cooling to room temperature, the solvent was evaporated. The crude product was purified through column chromatography using ethyl acetate/petroleum ether (from 1/1 to 2/1) as the eluent. [2-[2-(2-hydroxyethoxy)ethoxy]ethoxy] benzonitrile was obtained as a colorless oil (2.12 g, 84.4%). ^{1}H NMR (300 MHz, CD_2Cl_2) δ 7.66 – 7.57 (m, 2H), 7.05 – 6.98 (m, 2H), 4.19 (dd, J = 5.6, 3.6 Hz, 2H), 3.89 – 3.84 (m, 2H), 3.73 – 3.65 (m, 6H), 3.58 (dd, J = 5.5, 3.5 Hz, 2H).

Synthesis of propiolic acid 2-[2-[2-(4-cyanophenoxy)ethoxy]ethoxy]ethyl ester (PCE, Figure S1)

Propiolic acid (700 mg, 10.00 mmol), [2-[2-(2-hydroxyethoxy)ethoxy]ethoxy] benzonitrile (2.51 g, 10.00 mmol) and 4-dimethylaminopyridine (122 mg, 1.00 mmol) were dissolved in 20 mL dry dichloromethane (DCM) under argon atmosphere. Dicyclohexylcarbodiimide (DCC) (2.06 g, 10.00 mmol) in 10 mL DCM was added dropwise in an ice bath. After stirring at room temperature for 24 h, the solution was filtrated and evaporated. The crude product was purified through column chromatography using ethyl acetate/petroleum ether (from 1/2 to 1/1) as the eluent. PCE was obtained as a light yellow oil (2.64 g, 87.1%). ^{1}H NMR (300 MHz, CD_2Cl_2) δ 7.70 – 7.59 (m, 2H), 7.06 – 6.98 (m, 2H), 4.38 – 4.31 (m, 2H), 4.20 (dd, J = 5.7, 3.5 Hz, 2H), 3.88 (dd, J = 5.7, 3.6 Hz, 2H), 3.71 (pd, J = 4.9, 2.3 Hz, 6H), 3.02 (s, 1H).

Synthesis of $Ru(biq)_2Cl_2$ (Figure S1)

$Ru(biq)_2Cl_2$ was synthesized according to the literature.[1]

Synthesis of $[Ru(biq)_2(PCE)_2](PF_6)_2$ (Figure S1)

$Ru(biq)_2Cl_2$ (200 mg, 0.28 mmol) and $AgPF_6$ (92 mg, 0.58 mmol) were dissolved in 1:1 ethanol/H_2O mixture (10 mL). The mixture was degassed and refluxed at 80 ℃ overnight in an argon (Ar) atmosphere. After cooling to room temperature, AgCl was removed and the solution was reduced to 5 mL. Subsequently, saturated KPF_6 solution was added. The precipitate was filtered, followed by washing with a small amount of H_2O, and dried to obtained $[Ru(biq)_2(H_2O)_2](PF_6)_2$. Afterwards,

$[Ru(biq)_2(H_2O)_2](PF_6)_2$ (206 mg, 0.22 mmol) and PCE (139 mg, 0.46 mmol) were dissolved in 15 mL acetone. The solution was degassed and refluxed at 55 ℃ in the dark for 12 h. After cooling to room temperature, the solvent was evaporated and the crude product was purified through column chromatography using methonal/DCM (from 1/10 to 1/8) as the eluent. $[Ru(biq)_2(PCE)_2](PF_6)_2$ was obtained as a red solid (154 mg, 46.3%). ^{1}H NMR (300 MHz, CD_2Cl_2) δ 9.51 (d, J = 8.8 Hz, 2H), 8.68 (d, J = 8.7 Hz, 2H), 8.34 (t, J = 9.1 Hz, 6H), 8.06 (d, J = 7.6 Hz, 2H), 7.93 (d, J = 8.6 Hz, 4H), 7.83 (d, J = 8.7 Hz, 2H), 7.56 (t, J = 7.4 Hz, 2H), 7.46 (d, J = 8.6 Hz, 4H), 6.96 (d, J = 8.7 Hz, 6H), 6.83 (d, J = 8.7 Hz, 2H), 4.33 – 4.24 (m, 4H), 4.16 (t, J = 4.6 Hz, 4H), 3.82 (t, J = 4.5 Hz, 4H), 3.71 – 3.60 (m, 12H), 3.00 (s, 2H). ^{13}C NMR (300 MHz, CD_2Cl_2) δ 163.77, 160.34, 160.11, 152.43, 150.66, 149.60, 132.76, 129.46, 128.94, 101.06, 74.96, 74.34, 70.64, 70.54, 69.14, 68.45, 68.18, 65.64, 65.22. ESI-MS: $[M-2PF_6]^{2+}$: calcd. 610.1629; obsd. 610.1635. Δ = 0.9 ppm.

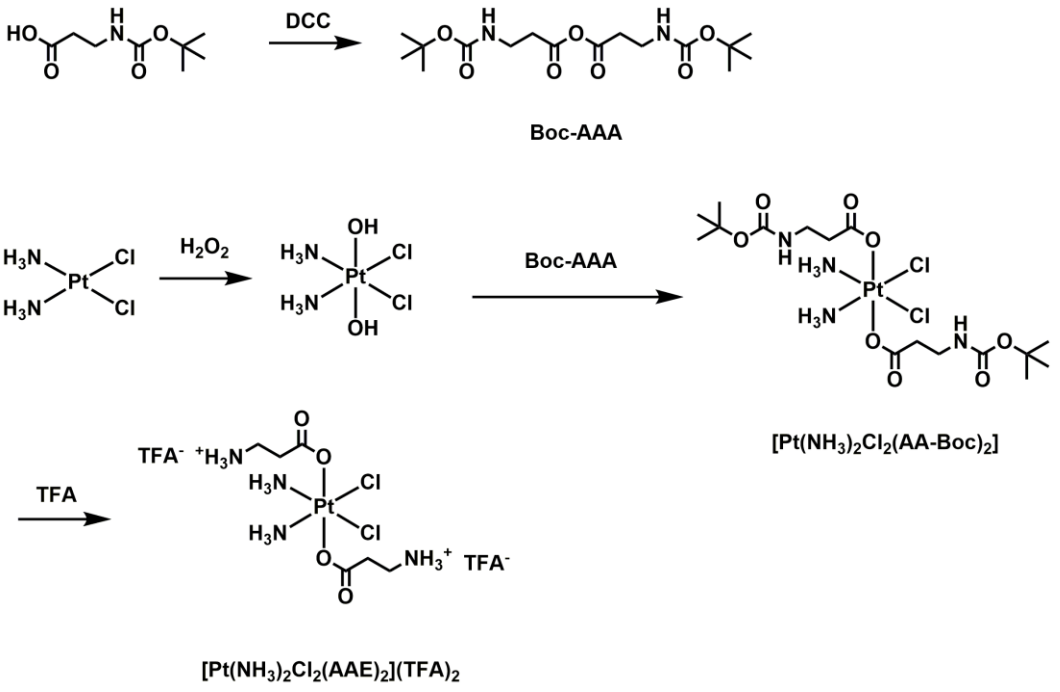

Figure S2. Synthetic route of $[Pt(NH_3)_2Cl_2(AAE)_2](TFA)_2$.

Synthesis of N-Boc aminopropanoic acid anhydride (Boc-AAA, Figure S2)

Boc-β-alanine (600 mg, 3.20 mmmol) was dissolved in dry 5 mL DCM. The solution was cooling down to 0 ℃ in an ice bath. DCC (320 mg, 1.58 mmol) in 5 mL DCM was added dropwise into the above solution. After stirring at room temperature for 24 h, the solution was filtrated and evaporated. The crude product was taken up by small amount of toluene and stored in refrigerator for 4 h. The precipitation was removed and the solvent was evaporated. Boc-AA was obtained as a colorless oil without any further purification (1.02 g, 89.7%). ^{1}H NMR (300 MHz, $CDCl_3$) δ 5.09 (s, 2H), 3.45 (q, J = 6.0 Hz, 4H), 2.70 (t, J = 5.9 Hz, 4H), 1.45 (s, 18H).

Synthesis of $[Pt(NH_3)_2Cl_2(AA\text{-}Boc)_2]$ (Figure S2)

To obtain $[Pt(NH_3)_2Cl_2(AA\text{-}Boc)_2]$, first cisplatin (169 mg, 0.56 mmol) was oxidized with H_2O_2 to afford $[PtCl_2(NH_3)_2(OH)_2]$, then followed by mixing with Boc-AAA (1.02 g, 2.82 mmol) in DMF. The mixture was kept at 50 ℃ overnight. Subsequently, DMF was removed under high vacuum, a small amount of methanol was added into the resulting yellow oil. The solution was added dropwise into diethyl ether and the forming precipitate was collected by centrifugation. $[Pt(NH_3)_2Cl_2(AA\text{-}Boc)_2]$ was obtained as white solid after washing with water and diethyl ether (178 mg, 43.9%). ^{1}H NMR (300 MHz, MeOD) δ 3.29 (dd, J = 6.4, 4.4 Hz, 4H), 2.51 (dd, J = 8.6, 4.3 Hz, 4H), 1.45 (s, 18H).

Synthesis of $[Pt(NH_3)_2Cl_2(AAE)_2](TFA)_2$ (Figure S2)

$[Pt(NH_3)_2Cl_2(AA\text{-}Boc)_2]$ (100 mg, 0.27 mmol) was dissolved in 2 mL DCM/TFA (1:1, v/v) mixture. The solution was stirred at room temperature for 30 min. Afterwards, the solvent was removed under a stream of Ar atmosphere. A small amount of DCM was added to re-dissolve the crude product. The formed solution was added dropwise in a cold diethyl ether. The resulting precipitate was collected by centrifugation. $[Pt(NH_3)_2Cl_2(AAE)_2](TFA)_2$ was obtained as white solid (95.6 mg, 74.9%). ^{1}H NMR (250 MHz, D2O) δ 3.10 (t, J = 6.4 Hz, 4H), 2.72 (t, J = 6.4 Hz, 4H). ESI-MS: $[M+H]^+$: calcd. 477.0498; obsd. 477.0414. Δ = 7 ppm.

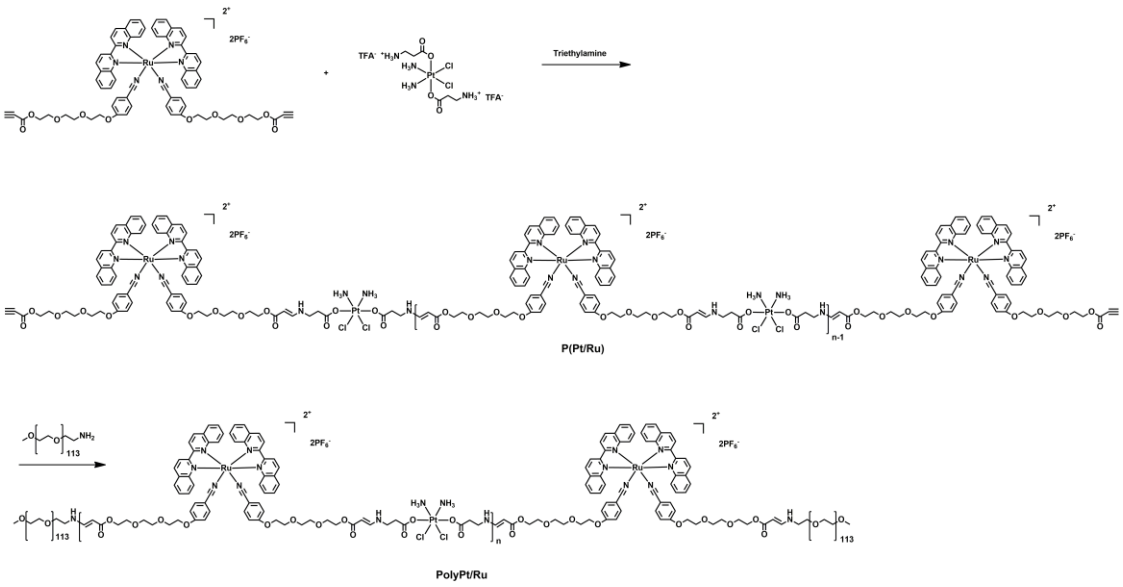

Figure S3. Synthetic route of P(Pt/Ru) and PolyPt/Ru.

Synthesis of P(Pt/Ru) (Figure S3)

Polymerization was performed via a spontaneous amino-yne click reaction according to the reported literature.[2, 3] To start with, $[Ru(biq)_2(PCE)_2](PF_6)_2$ (151 mg, 0.10 mmol) was added into a 5 mL Schlenk tube equipped with a mini magnetic stir bar. The tube was degassed and flushed with Ar atmosphere. 200 μL DMF containing $[Pt(NH_3)_2Cl_2(AAE)_2](TFA)_2$ (54 mg, 0.08 mmol) along with 20 μL DIPEA was injected dropwise into the tube and stirred at room temperature in the dark overnight. After reaction, the mixture was poured into cold diethyl ether and stored in -20 ℃ overnight. The precipitates were filtered and washed with acetone three times, followed by drying in vacuum to a constant weight. P(Pt/Ru) was obtained as a light red solid (124 mg).

Synthesis of PEG-*b*-P(Pt/Ru)-*b*-PEG (PolyPt/Ru, Figure S3)

To obtain PolyPt/Ru, poly(ethylene glycol) methyl ether amine (mPEG5k-NH_2) with a primary amine was used to terminate the ethynyl groups.[4] Typically, 100 mg P(Pt/Ru) was added into a 5 mL Schlenk tube equipped with a mini magnetic stir bar. The tube was degassed and flushed with Ar atmosphere. mPEG5k-NH_2 (110 mg, 0.022 mmol) in 1 mL DMF was injected into the tube by syringe, and then stirred at room temperature for 12 h. Subsequently, the mixture was poured into cold diethyl ether. The resulting precipitates were filtered and washed with a small amount of water, followed by redissolving in THF and precipitating from diethyl ether. The precipitates were washed with water and diethyl ether to obtain PolyPt/Ru as a pink solid (57 mg).

Sample preparation

Preparation of PolyPt/Ru nanoparticles

To prepare PolyPt/Ru nanoparticles, 1.8 mL distilled water was added dropwise into a 0.2 mL THF/DMF mixture (7/1, v/v) containing 2 mg PolyPt/Ru and stirred in the dark for 20 min. The stirring rate was 300 rpm. Afterwards, the nanoparticle dispersion was dialyzed against 5 L Milli-Q water for 48 h using a dialysis tube (MW cutoff, 3.5 kDa). Milli-Q water was replaced every 12 h.

Drug release profiles

PolyPt/Ru nanoparticles or $[Pt(NH_3)_2Cl_2(AAE)_2](TFA)_2$ were prepared in Milli-Q water with or without 5.0 mM GSH, respectively. The solution was placed into an end-sealed dialysis bag and immersed in aforementioned solution before incubating in a continuous shaker at 37 °C. 1 mL of the dialysate was withdrawn at specified time intervals and then fresh solution (1 mL) was added to the dialysate. The released drug content was calculated using UV-Vis absorption spectroscopy.

Preparation of DiD dye loaded PolyPt/Ru nanoparticles

To prepare DiD dye loaded PolyPt/Ru nanoparticles, 50 µL DiD solution (1 mg/mL in DMF) was added into 0.2 mL THF/DMF (7/1, v/v) containing 2 mg PolyPt/Ru. The solution was stirred for 20 min with stirring rate at 300 rpm. After that, 1.8 mL distilled water was added dropwise into the solution and kept stirring for another 30 min. The DiD dye loaded nanoparticles dispersion was dialyzed against 5 L Milli-Q water for 48 h using a dialysis tube (MW cutoff, 3.5 kDa). Milli-Q water was replaced every 12 h.

Cell experiments

Cell culture

Human lung cancer cell line A549 and its cisplatin-resistant cell line A549-DDP, human liver cancer cell line BEL-7404 and its cisplatin-resistant cell line BEL-7404-CP20 (7404-CP20) were generously gifted by Michael M. Gottesman's laboratory at National Cancer Institute, National Institutes of Health, USA. A549 and cisplatin-resistant A549-DDP cell lines were cultured in DMEM medium. BEL-7404 and cisplatin-resistant 7404-CP20 cell lines were cultured in RPMI-1640 medium. The resistance of A549-DDP and 7402-CP20 was maintained by cisplatin-containing medium (1 μg/mL). The cells were used in the assays after one week from the end of the treatment to avoid interferences. All cell lines were complemented with 10% fetal bovine serum (FBS, Invitrogen, USA) and 1% penicillin/streptomycin (Life Technologies, USA) and maintained in humidified atmosphere at 37 °C and 5% of CO_2. Treatment with trypsin (0.25%) (Life technologies, USA) for 5 minutes was employed to detach the cells for further assays.

Cell viability assay

All cell viability tests were evaluated using a standard Cell Counting Kit-8 (CCK-8) assay kit (Solarbio, China). Typically, cancer cells were incubated with DMEM/ RPMI-1640 medium in 96-well plates at a density of 5.0×10^3 cells per well overnight. The medium was then replaced by DMEM/ RPMI-1640 containing different compounds or PolyPt/Ru nanoparticles in the dark. To investigate the cell viability of $[Ru(biq)_2(H_2O)_2](PF_6)_2$ or PolyPt/Ru nanoparticles under irradiation, each sample was added to the cell medium and cultured for 6 h, followed by exposure to 671 nm red light

irradiation for 20 min. Then, cells were incubated for 24 h. CCK-8 working solution was added as 10 μL per well, followed by another incubation for 4 h. Cell viability was assessed by the measurement of the absorbance at the wavelength of 450 nm on the microplate reader (EnSpire, Perkin Elmer). Treatment procedures were replicated three times for each cell line.

Combination effect analysis

The combination index (CI) was calculated according to the median-effect analysis.[5, 6] CI was determined with the following equation: $CI = (D)_1/(D_{50})_1 + (D)_2/(D_{50})_2$, where $(D_{50})_1$ is the dose of agent 1 required to produce 50% effect alone, and $(D)_1$ is the dose of agent 1 required to produce the same 50% effect in combination with $(D)_2$. Similarly, $(D_{50})_2$ is the dose of agent 2 required to produce 50% effect alone, and $(D)_2$ is the dose required to produce the same effect in combination with $(D)_1$. This mathematical algorithm generates CI value <0.9 when the combinations are synergistic, 0.9–1.1 when they are additive, and >1.1 when they are antagonistic.

Cell imaging by confocal laser scanning microscopy (CLSM)

For the cellular uptake experiments, 1×10^5 cells per milliliter were seeded in 35 mm diameter μ-dishes and cultured overnight in supplemented medium. The medium was replaced by fresh medium containing 50 μg/mL DiD-loaded PolyPt/Ru nanoparticles. The cells were incubated with different time periods. Subsequently, the nuclei were stained with Hoechst 33342 (0.5 μg/mL, Sigma, USA). PolyPt/Ru nanoparticles were further removed by washing with PBS three times. Live cells images were taken using CLSM (LSM710, Carl Zeiss). DiD-loaded PolyPt/Ru nanoparticles were excited with

a 633 nm laser and detected in the range from 650 to 750 nm. The cell nuclei were excited with a 405 nm laser and detected in the range from 425 to 475 nm.

For the intracellular singlet oxygen ($^1O_2$) detection assay, the fluorescent probe DCFH-DA (Solarbio, China) was used according to the manufacture's instruction. Specifically, 1×10^5 cells per milliliter were seeded in 35 mm diameter μ-dishes and cultured overnight in supplemented medium. The cells were divided into five groups: (1) Control group; (2) + Light group; (3) +PolyPt/Ru + light group; (4) +PolyPt/Ru + probe group; (5) +PolyPt/Ru + light + probe group. Then medium or 50 μg/mL PolyPt/Ru nanoparticles were incubated with the cells for 6 h. Afterwards, serum-free DCFH-DA solution (15 μM) was incubated with cells in (4) and (5) groups for 20 min. Cells in group (2), (3), and (5) were then irradiated with 671 nm red light for 1 min at an intensity of 125 $mWcm^{-2}$. All the cell nuclei were stained with Hoechst 33342 (0.5 μg/mL, Sigma, USA). Live cells were further imaged using CLSM (LSM710, Carl Zeiss). DCFH-DA was excited with a 488 nm laser, detected in the range from 500 to 550 nm. The cell nuclei were excited with a 405 nm laser and detected in the range from 425 to 475 nm.

Cellular uptake efficiency by flow cytometer

1×10^4 cells per well were seeded onto 24-well culture plates and cultured overnight in supplemented medium. After that, the medium was replaced by fresh prepared medium containing 50 μg/mL DiD-loaded PolyPt/Ru nanoparticles. The cells were incubated for different time, followed by washing with PBS buffer three times to remove the surface-bound nanoparticles. After the cells were digested by trypsinase and washed by PBS, the uptake efficiency was calculated by dividing the number of fluorescent cells

by the number of total cells. The fluorescent intensity was recorded by a flow cytometer (BD Accuri C6).

Animal experiments

Animal use and tumor model establishment

BALB/c nude mice (female, 18-20 g, 4-6 weeks) were purchased from Vital River Laboratory Animal Center (Beijing, China). All mice were maintained under specific pathogen-free conditions and had free access to food and water throughout all the experiments.

The patient-derived xenograft (PDX) models were established as the previous report.[7] Typically, the PDX tumor sample was cut into approximately 2 × 2 × 2 mm^3/fragment. Each fragment was subcutaneously inoculated into the shoulders of the mice. Tumor volume was measured using a vernier caliper and calculated as $V=L*W^2/2$, where L and W were the length and width of the tumor, respectively. The established PDX model was called passage 1 (P1). When the tumor size of P1 reached approximately 750 mm^3, the tumor was isolated and sliced into small approximately 2 × 2 × 2 mm^3/fragment and re-inoculated into mice to obtain the subsequent passage called P2. The similar procedure was conducted to obtain the subsequent passage called P3. The tumor from P3 was performed in the further *in vivo* experiments.

Hemolysis analysis

The fresh whole blood was obtained from BALB/c nude mice using sodium citrate as an anti-coagulant with a blood/ anticoagulant ratio of 9:1. The whole blood was subsequently centrifuged at 1000 × g for 5 min and then the plasma and buffy coat layer were removed. The obtained red blood cells (RBCs) were collected and washed with saline for three times, followed by suspending in 15 mL saline. The RBCs suspension

was incubated with saline containing different concentrations of PolyPt/Ru nanoparticles with the ratio of 1:1 (v/v). The final concentration of PolyPt/Ru nanoparticles was ranging from 200 to 1000 μg/mL. The positive hemolysis control was induced by replacing saline with same volume of water and the negative hemolysis control was saline without any PolyPt/Ru nanoparticles. Each sample was repeated three times. All samples were incubated at 37 ℃ for 24 h. After incubation, the RBCs were centrifuged at 1000 × g for 5 min and the absorbance of supernatants at 540 nm was measured by microplate reader. The hemolysis percentage was calculated by measuring the optical density (OD) as the following formula:

Hemolysis (%) = [(OD of sample absorbance – OD of background absorbance)/ (OD of positive control –OD of negative control)] × 100%.

In vivo fluorescence imaging

The PDX tumor-bearing mice at a tumor size approximately 100 mm^3 were treated with saline as control group or DiD-loaded PolyPt/Ru nanoparticles through intravenous injection via tail vein. The dosage of PolyPt/Ru nanoparticles was 10 mg/kg. After 0, 4, 12, 24 h, the mice were anesthetized with isoflurane and imaged under the *in vivo* imaging system (IVIS Spectrum, PerkinElmer). The excitation wavelength was fixed at 633 nm.

In vivo anticancer efficacy evaluation

The anticancer efficacy was evaluated by monitoring the tumor volumes using PDX models. The tumor nodules were allowed to reach approximately 100 mm^3 before initial

treatment. All the mice were numbered using ear tags and the initial tumor volume and body weight were recorded. Subsequently, the mice were randomly divided into five groups: (1) a group of PDX tumor-bearing mice was injected with saline (control group); (2) a group of PDX tumor-bearing mice was irradiated with light only (light group); (3) a group of PDX tumor-bearing mice was injected with equivalent dosage of cisplatin (cisplatin group); (4) a group of PDX-bearing mice was injected with PolyPt/Ru nanoparticles (PolyPt/Ru group); (5) a group of PDX tumor-bearing mice was injected with PolyPt/Ru nanoparticles (PolyPt/Ru + light group). The number of mice in each group was 5. Injections were performed on the first and third day during the treatments. Mice in group (3), (4), (5) were treated with equivalent dosage of 2 mg/kg cisplatin. 671 nm light irradiation (125 $mWcm^{-2}$, 20 min) in group (5) was performed after 12 h i.v. injection of PolyPt/Ru nanoparticles. To exclude the effect by light irradiation, Mice in group (2) were set as a negative control. The body weight and tumor volume of each mouse were measured every day. At day 7, the mice from each group were sacrificed and tumor were isolated for weighing.

Histological analyses

At the end of tumor inhibition experiments, the mice from each group were sacrificed and tumor were collected. Main organs including heart, liver, lung, kidney and spleen were also collected and fixed in 4% formaldehyde solution followed by paraffin embedding. The treated tumors and organs were then cut into pieces with thickness of 2 μm, and stained with hematoxylin and eosin (H&E) to assess histological alterations by microscope. Embedding and H&E staining were done by Wuhan Servicebio Technology Co., Ltd.

TUNEL assay

The isolated tumors were fixed in 4% formaldehyde solution followed by paraffin embedding and TUNEL staining. Typically, the paraffin embedded tumors were cut into approximately 8.0 μm by a rotary microtome (YD-1508A) and stained with 0.25% toluidine blue O. The DNA fragmentation was labelled using a TUNEL apoptosis detection kit and then observed by CLSM. Embedding and TUNEL staining were done by Wuhan Servicebio Technology Co., Ltd.

Immunohistochemical analysis

The isolated tumors were fixed in 4% formaldehyde solution at room temperature for 15 min, followed by washing with PBS and incubating with 1% BSA in phosphate buffered saline tween-20 (PBST) for 30 min to block unspecific binding of antibodies. Then, the tumor sections were incubated with antibody γH2AX (1:800 diluted in 1% BSA in PBST) in a humidified chamber for 1 h at 37 °C, followed by incubation with a secondary antibody in 1% BSA for 1 h at 37 °C in the dark. Antibodies were purchased from Wuhan Servicebio Technology Co., Ltd. Samples were observed by CLSM.

Statistical analysis

One-way ANOVA with Tukey's multiple comparison analysis was used to determine the significance of differences between different groups. Data were calculated and appropriate statistical results were marked as $*p < 0.05$ and $***p < 0.001$.

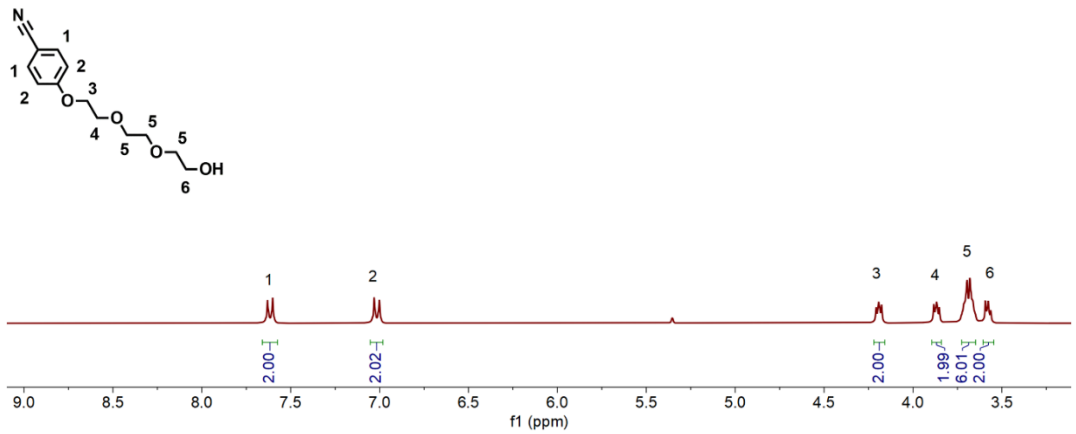

Figure S4. ^{1}H NMR spectrum of [2-[2-(2-hydroxyethoxy)ethoxy]ethoxy]benzonitrile (300 MHz, CD_2Cl_2).

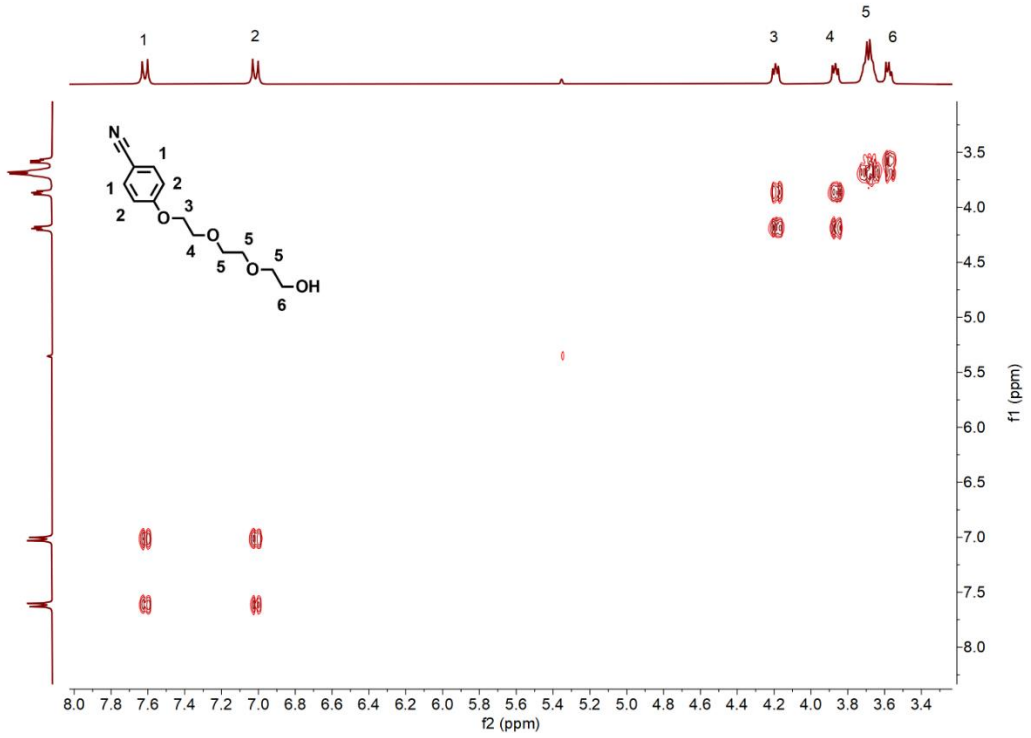

Figure S5. COSY spectrum of [2-[2-(2-hydroxyethoxy)ethoxy]ethoxy]benzonitrile (300 MHz, CD_2Cl_2).

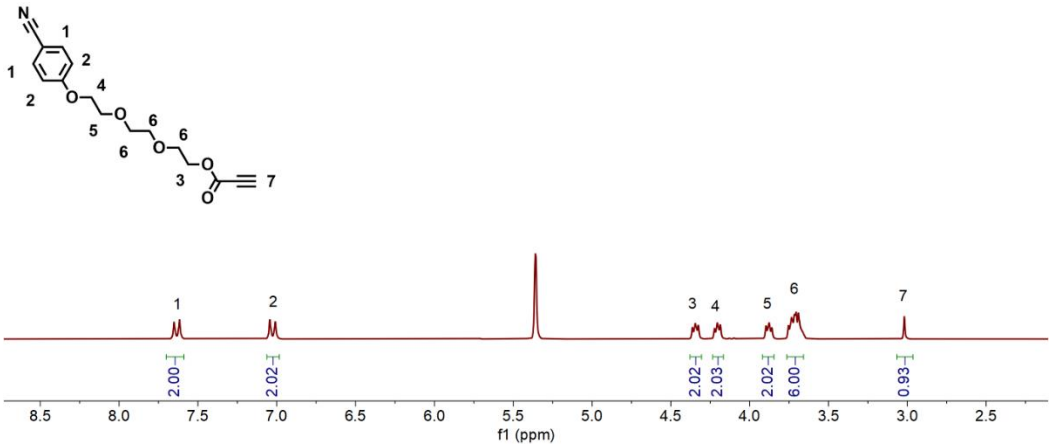

Figure S6. ^{1}H NMR spectrum of PCE (300 MHz, CD_2Cl_2).

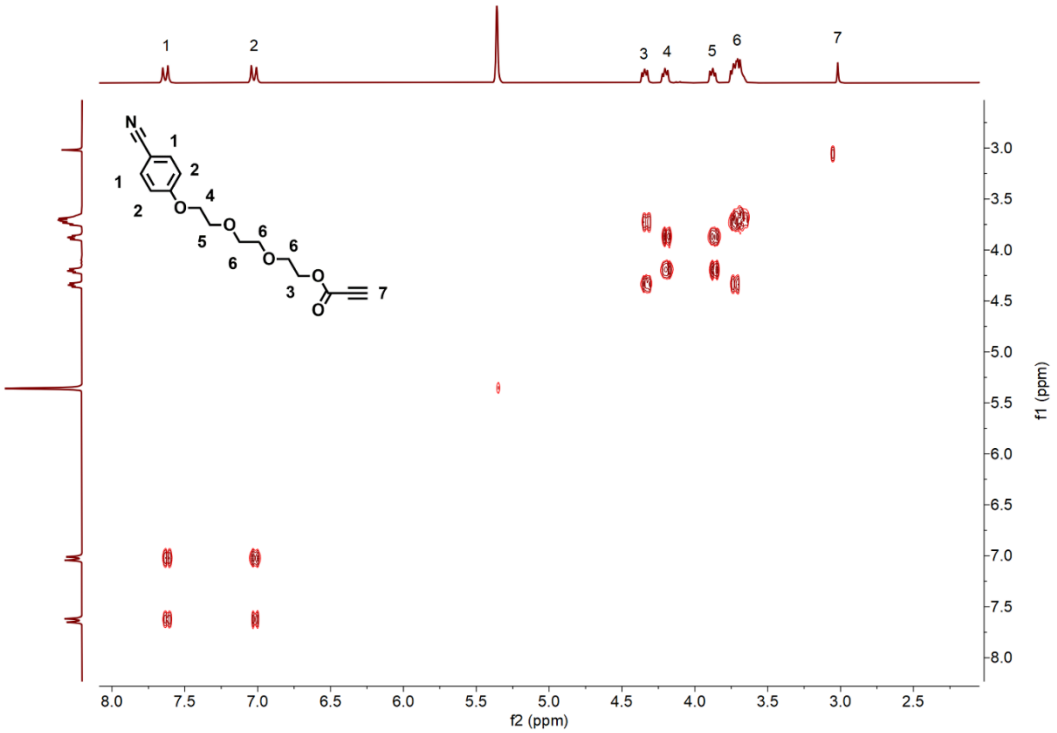

Figure S7. COSY spectrum of PCE (300 MHz, CD_2Cl_2).

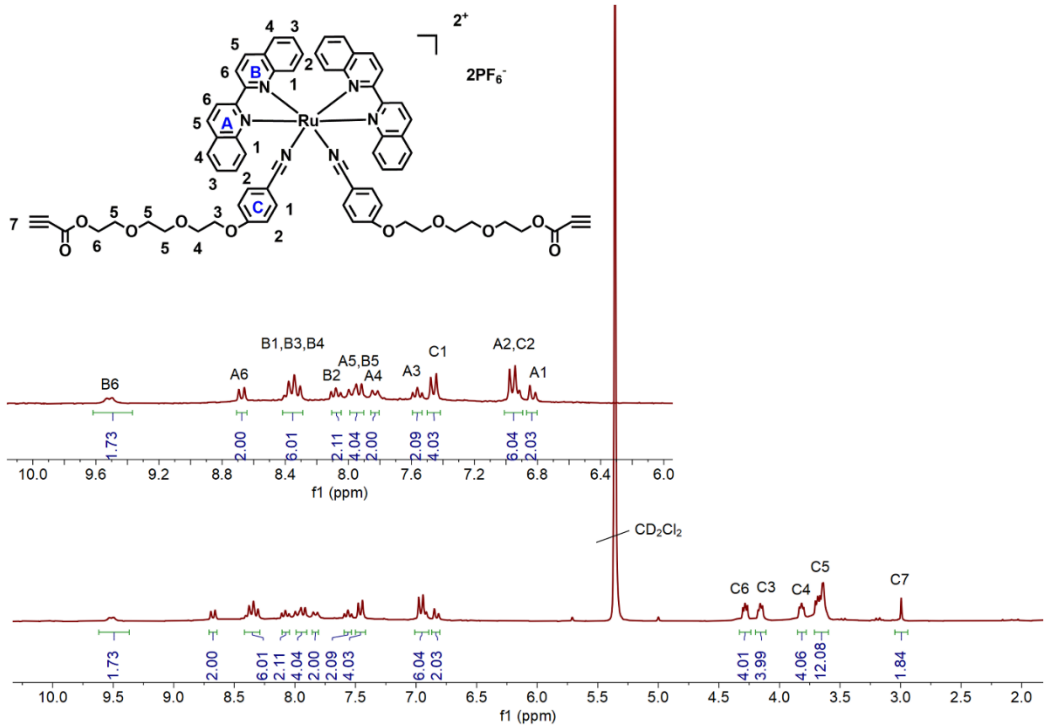

Figure S8. ^{1}H NMR spectrum of $[Ru(biq)_2(PCE)_2](PF_6)_2$ (300 MHz, CD_2Cl_2).

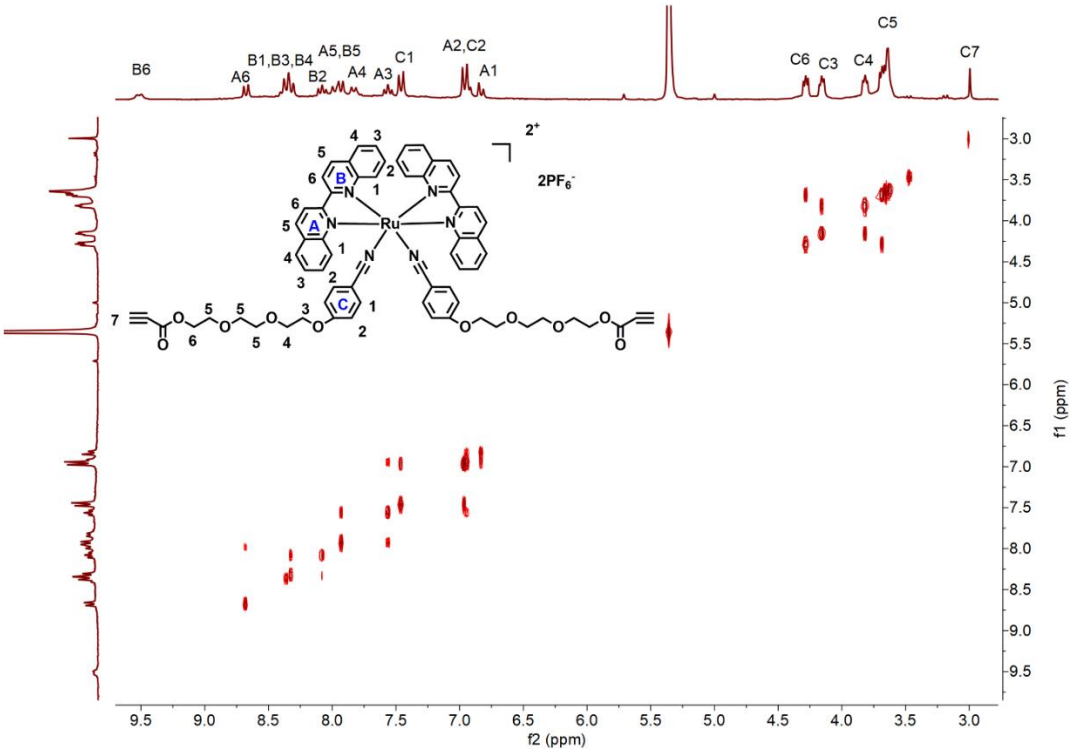

Figure S9. COSY spectrum of $[Ru(biq)_2(PCE)_2](PF_6)_2$ (300 MHz, CD_2Cl_2).

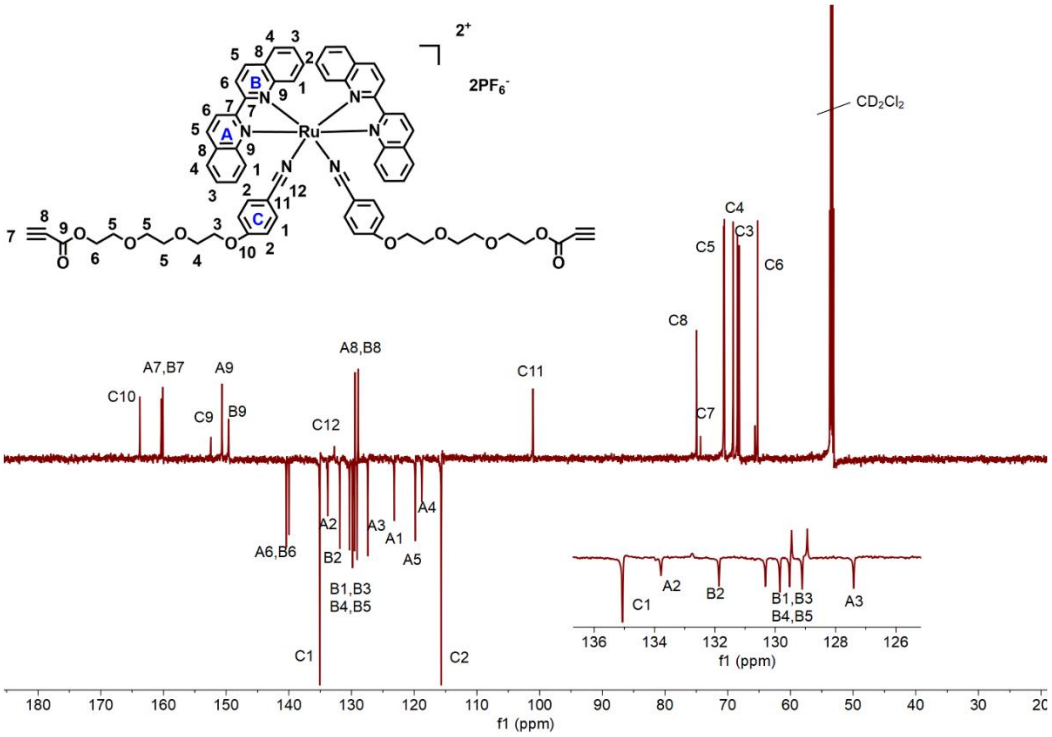

Figure S10. ^{13}C NMR spectrum of $[Ru(biq)_2(PCE)_2](PF_6)_2$ (300 MHz, CD_2Cl_2).

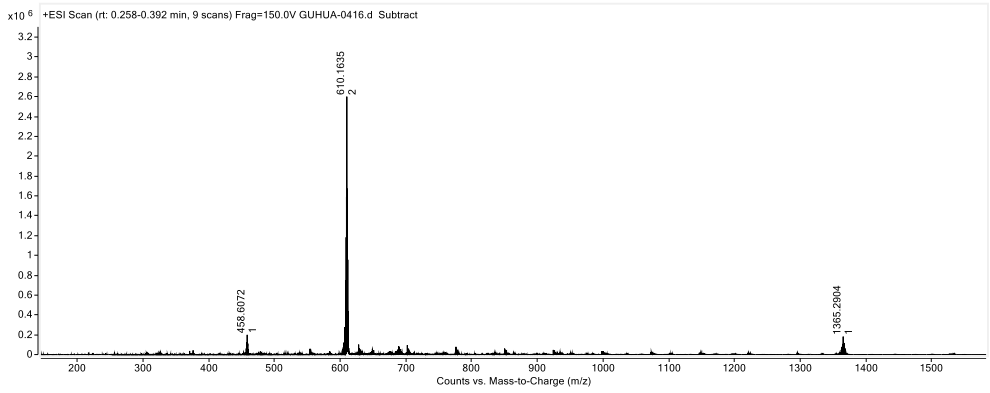

Figure S11. ESI-MS spectrum of $[Ru(biq)_2(PCE)_2](PF_6)_2$. $[M-2PF_6]^{2+}$: calcd. 610.1629; obsd. 610.1635. Δ = 0.9 ppm.

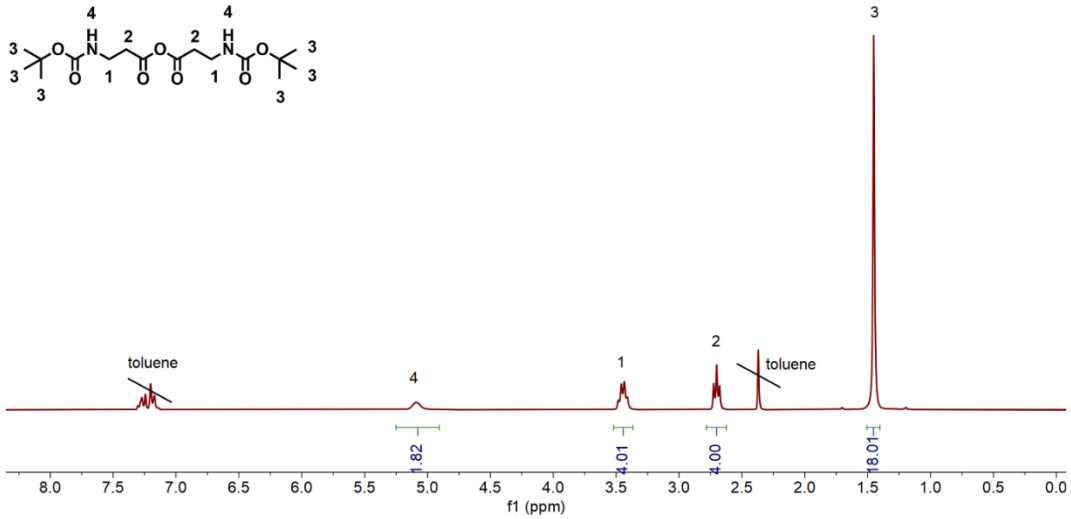

Figure S12. ^{1}H NMR spectrum of Boc-AAA (300 MHz, $CDCl_3$).

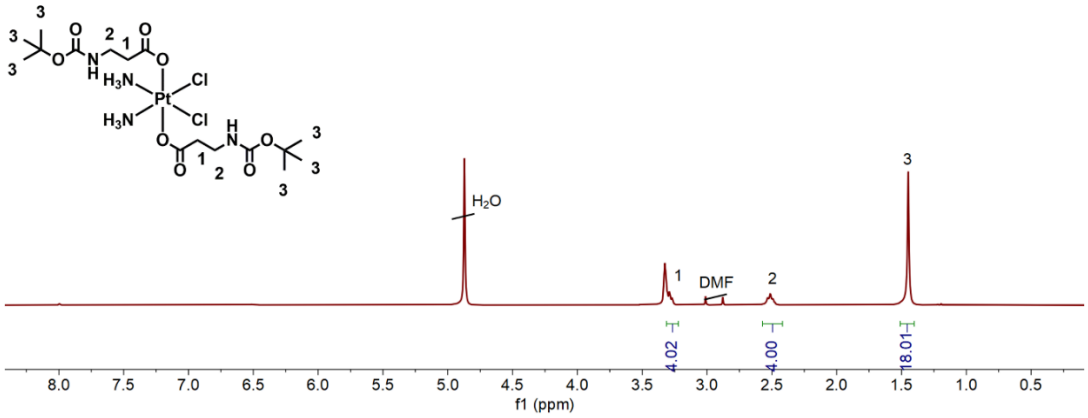

Figure S13. ^{1}H NMR spectrum of $[Pt(NH_3)_2Cl_2(AA\text{-}Boc)_2](TFA)_2$ (300 MHz, MeOH-d_6).

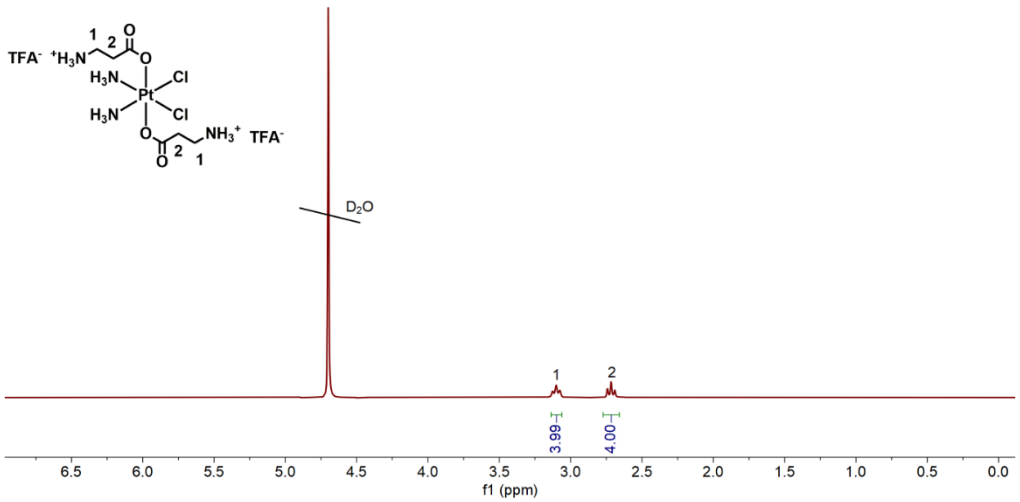

Figure S14. ^{1}H NMR spectrum of $[Pt(NH_3)_2Cl_2(AAE)_2](TFA)_2$. (250 MHz, D_2O).

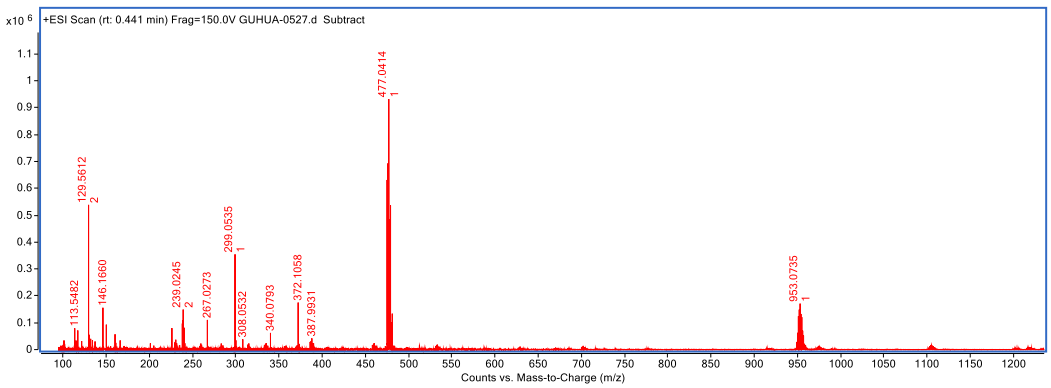

Figure S15. ESI-MS spectrum of $[Pt(NH_3)_2Cl_2(AAE)_2](TFA)_2$. $[M+H]^+$: calcd. 477.0498; obsd. 477.0414. Δ = 7 ppm.

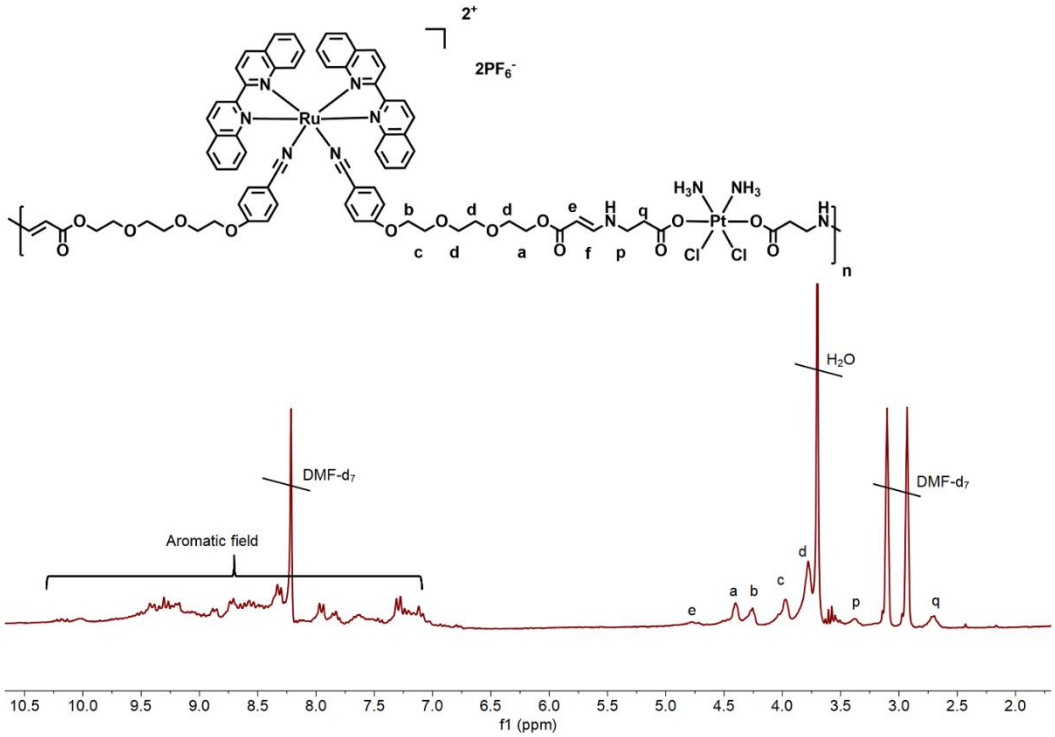

Figure S16. ^{1}H NMR spectrum of P(Pt/Ru) (300 MHz, DMF-d_7).

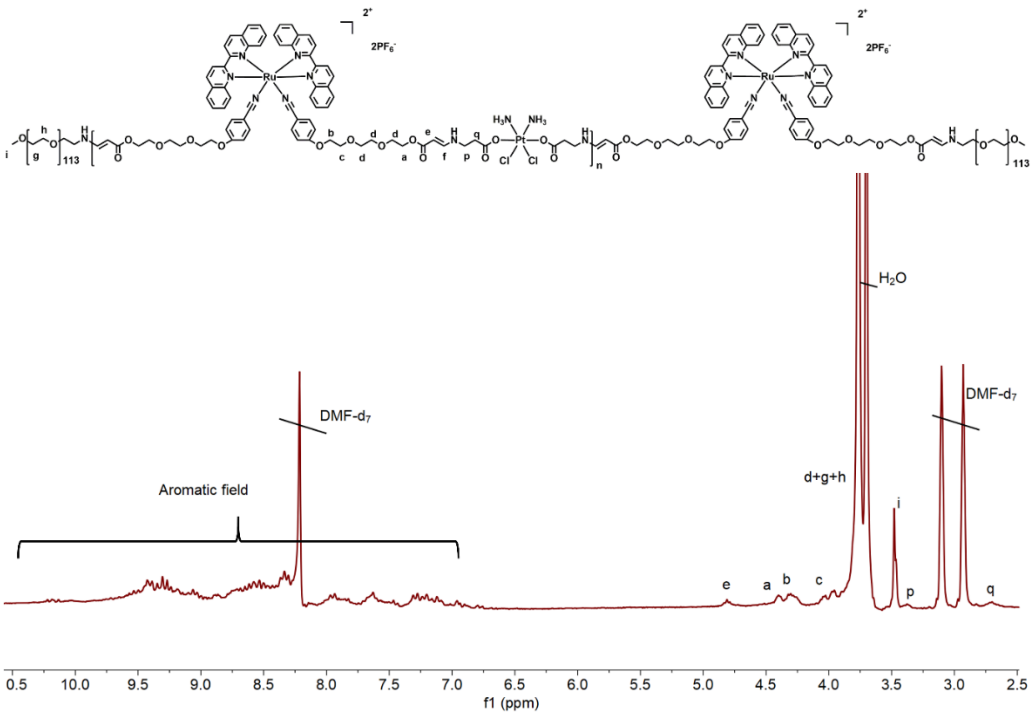

Figure S17. ^{1}H NMR spectrum of PolyPt/Ru (300 MHz, DMF-*d*$_7$). NMR provided details about the structure of PolyPt/Ru. The ethynyl proton of $[Ru(biq)_2(PCE)_2](PF_6)_2$ at 2.98 ppm could not be observed in the spectra of PolyPt/Ru. In contrast, a new peak at 4.75 ppm appeared, which was assigned to one of the HC=CH signal next to the nitrogen atom of PolyPt/Ru. The other proton signal of HC=CH group located in the aromatic region, which was overlapped with those of the biq ligand. Moreover, the peaks of aromatic area of PolyPt/Ru were broad and overlapped with adjacent signals, which are typical for polymers. The molecular weight of PolyPt/Ru was estimated according to the integral ratio of the peaks at 4.75 ppm and 3.41 ppm in the ^{1}H NMR spectrum. The molar mass of PolyPt/Ru measured by ^{1}H NMR spectrum was 17 kg/mol. The actual loading contents of Ru(II) and Pt(IV) repeat units were 32% and 10%, respectively.

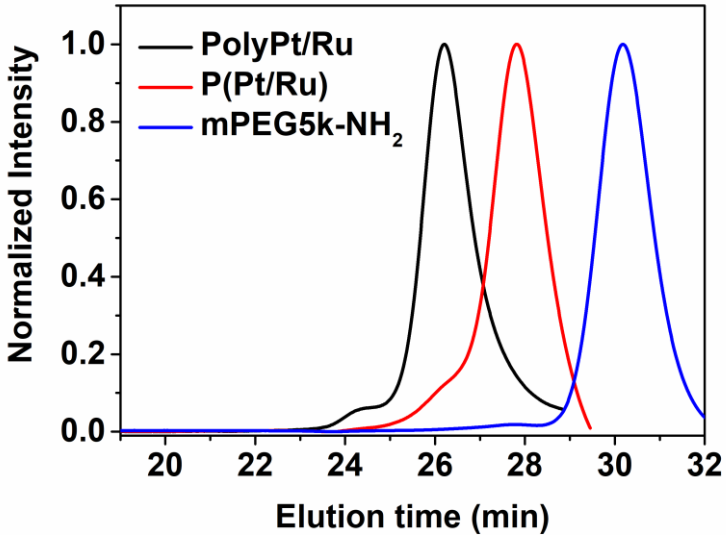

Figure S18. GPC traces of PolyPt/Ru, P(Pt/Ru), mPEG5k-NH_2.

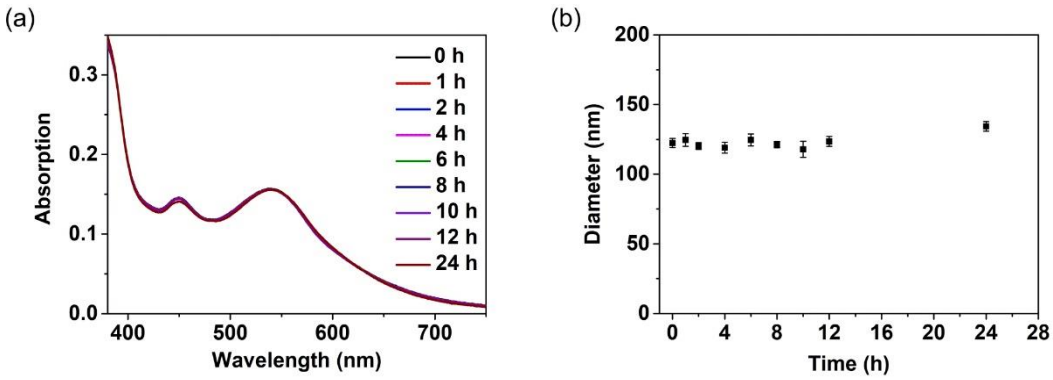

Figure S19. (a) Stability of PolyPt/Ru nanoparticles in PBS buffer studied by UV-vis absorption spectroscopy. (b) Stability of PolyPt/Ru nanoparticles in PBS buffer studied by DLS. Results showed that PolyPt/Ru nanoparticles were stable.

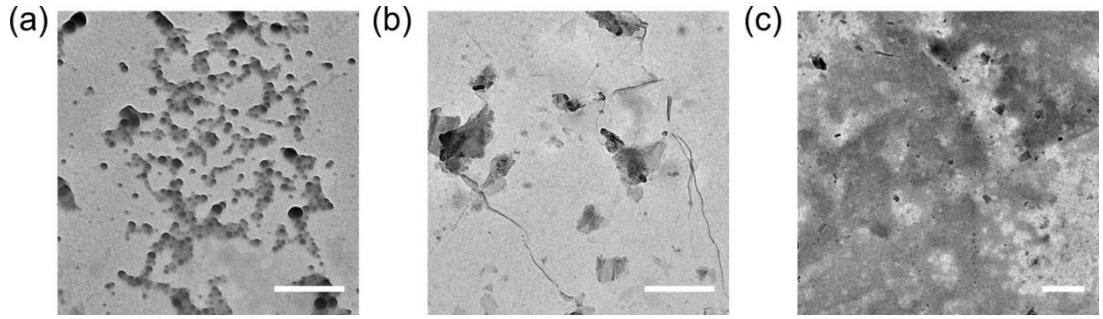

Figure S20. (a) TEM of PolyPt/Ru nanoparticles after 671 nm red light irradiation (125 mW cm^{-2}, 30 min); (b) TEM of PolyPt/Ru nanoparticles after 5.0 mM GSH treatment; (c) TEM of PolyPt/Ru nanoparticles after 671 nm red light irradiation (125 mW cm^{-2}, 30 min) with 5.0 mM GSH treatment. Scale bars: 500 nm.

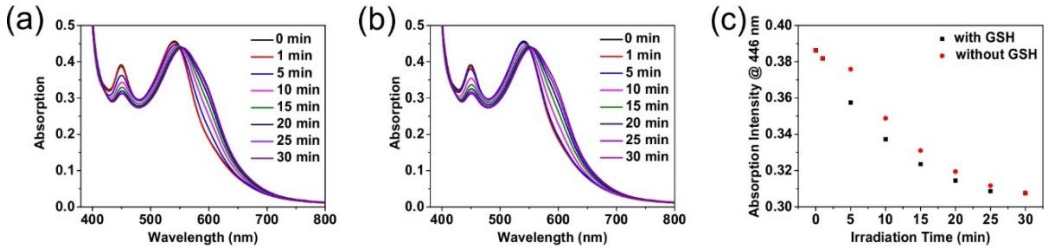

Figure S21. Change of UV-Vis absorption spectrum of PolyPt/Ru nanoparticles under red light irradiation (125 mW cm^{-2}, 30 min) (a) in the presence of 5.0 mM GSH and (b) in the absence of 5.0 mM GSH. (c) Relative absorption changes at 446 nm of PolyPt/Ru nanoparticles. PolyPt/Ru nanoparticles exhibited a broad ^{1}MLCT band ranging from 450 nm tailing to 800 nm. Upon 671 nm light irradiation for 30 min, the ^{1}MLCT band of PolyPt/Ru nanoparticles was both red-shifted in the presence or absence of GSH. By comparing the absorption intensity at 446 nm, light irradiation in the presence of GSH showed slightly faster photoreaction rate. This is because GSH induced reduction of Pt(IV) moieties and partial degradation of PolyPt/Ru nanoparticles. So, water molecules had a higher probability to enter PolyPt/Ru nanoparticles, causing faster photosubstitution of Ru(II) moieties.

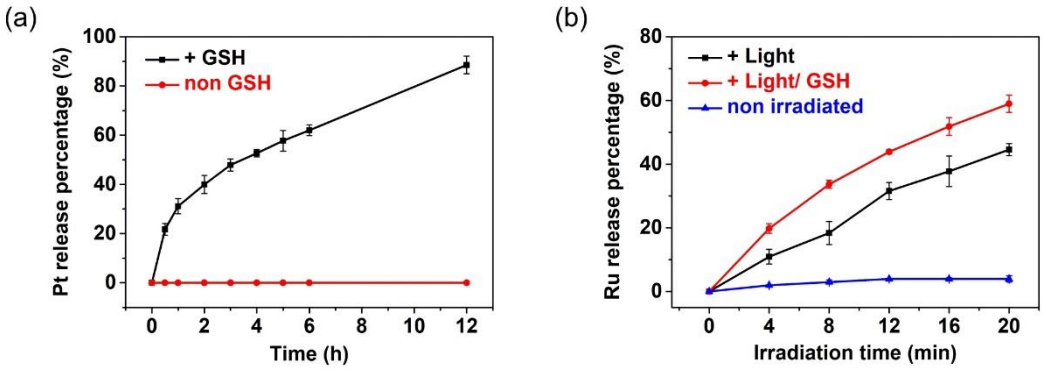

Figure S22. (a) The released percentage of cisplatin from $[Pt(NH_3)_2Cl_2(AAE)_2](TFA)_2$ under 5.0 mM GSH. (b) The released percentage of $[Ru(biq)_2(H_2O)_2](PF_6)_2$ from PolyPt/Ru nanoparticles under red light irradiation (25 mW cm^{-2}, 20 min) and red light irradiation (25 mW cm^{-2}, 20 min) with 5.0 mM GSH. Up to 45% of $[Ru(biq)_2(H_2O)_2](PF_6)_2$ was released under light irradiation. Furthermore, 60% of $[Ru(biq)_2(H_2O)_2](PF_6)_2$ was released under light irradiation in the presence of GSH, indicating that the degradation of Pt(IV) moieties promoted the release of the Ru(II) moieties in the PolyPt/Ru nanoparticles.

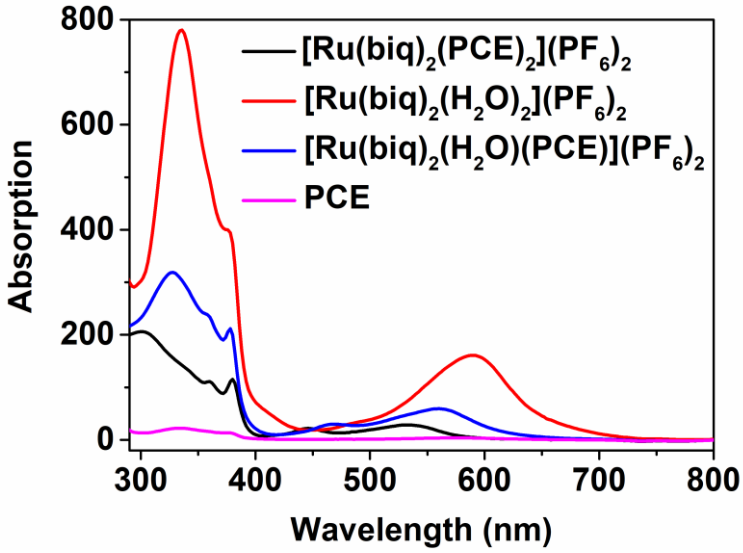

Figure S23. UV-vis absorption spectra of $[Ru(biq)_2(PCE)_2](PF_6)_2$ and the photoproducts in HPLC measurements in Figure 2 in the main manuscript. The spectra were measured by the UV-vis detector in the HPLC system.

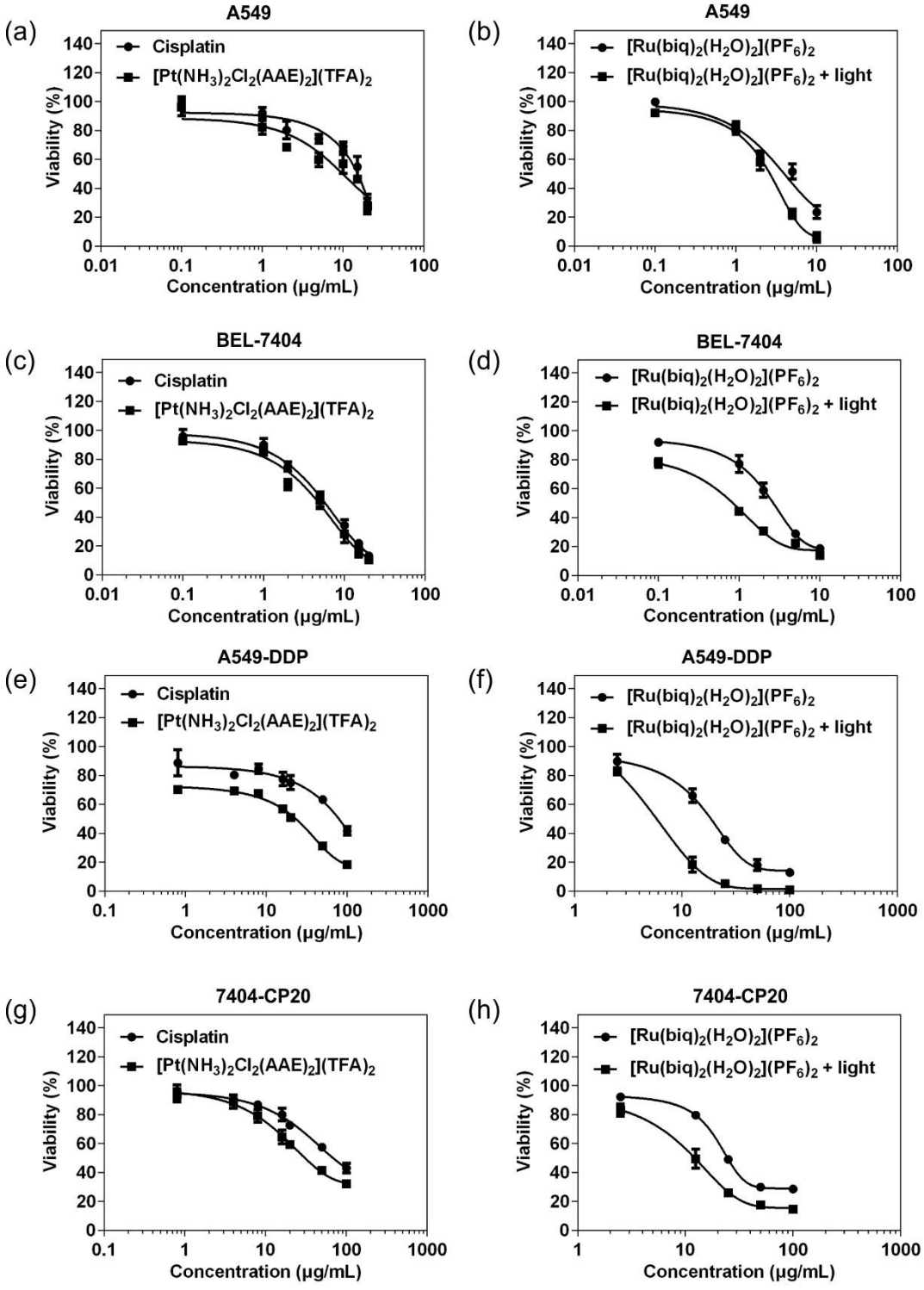

Figure S24. Viability of A549 (a), BEL-7404 (c), A549-DDP (e), 7402-CP20 (g) cells incubated with cisplatin or $[Pt(NH_3)_2Cl_2(AAE)_2](TFA)_2$ with different concentrations for 24 h. Viability of A549 (b), BEL-7404 (d), A549-DDP (f), 7402-CP20 (h) cells incubated with $[Ru(biq)_2(H_2O)_2](PF_6)_2$ in the dark or under 671 nm red light irradiation

with different concentrations for 24 h. Light irradiation (125 mW cm^{-2}, 20 min) was given after 6 h incubation and cell viability was assessed after further incubation of 24 h.

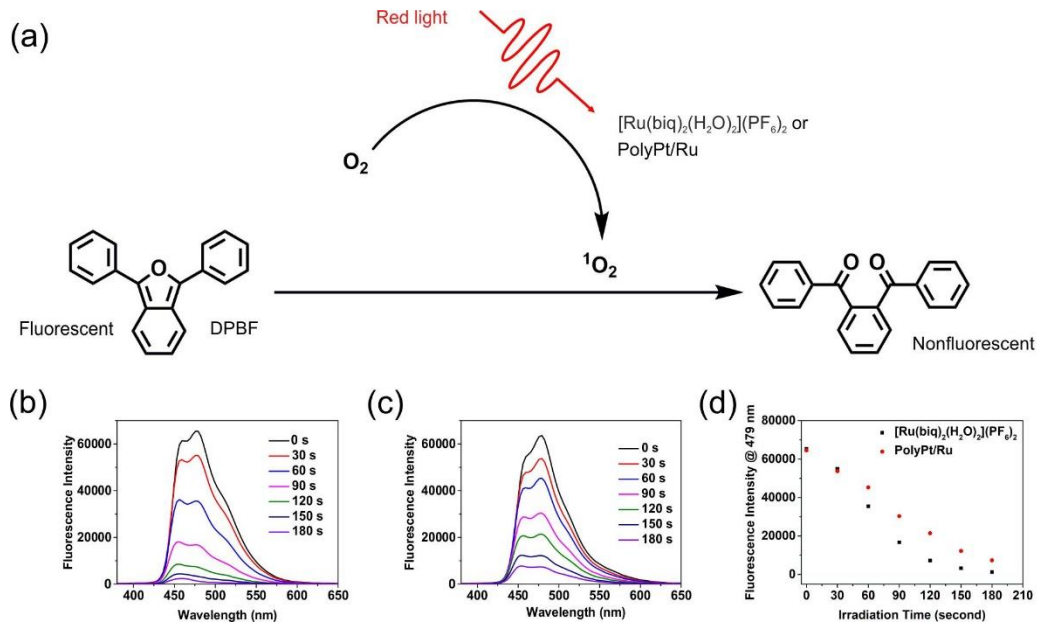

Figure S25. (a) Mechanism of using 1, 3- diphenylisobenzofuran (DPBF) to detect singlet oxygen ($^1O_2$) generated by $[Ru(biq)_2(H_2O)_2](PF_6)_2$ or PolyPt/Ru under red light irradiation. (b) Fluorescence spectrum of DPBF (150 μM) in the presence of $[Ru(biq)_2(H_2O)_2](PF_6)_2$ (200 μg/mL) under 671 nm light irradiation (50 mW/cm^2) in a water/methanol mixture. (c) Fluorescence spectrum of DPBF (150 μM) in the presence of PolyPt/Ru (200 μg/mL) under 671 nm light irradiation (50 mW/cm^2) in a water/methanol mixture. (d) Relative fluorescence intensity at 479 nm of DPBF (150 μM) in the presence of $[Ru(biq)_2(H_2O)_2](PF_6)_2$ or PolyPt/Ru under light irradiation.

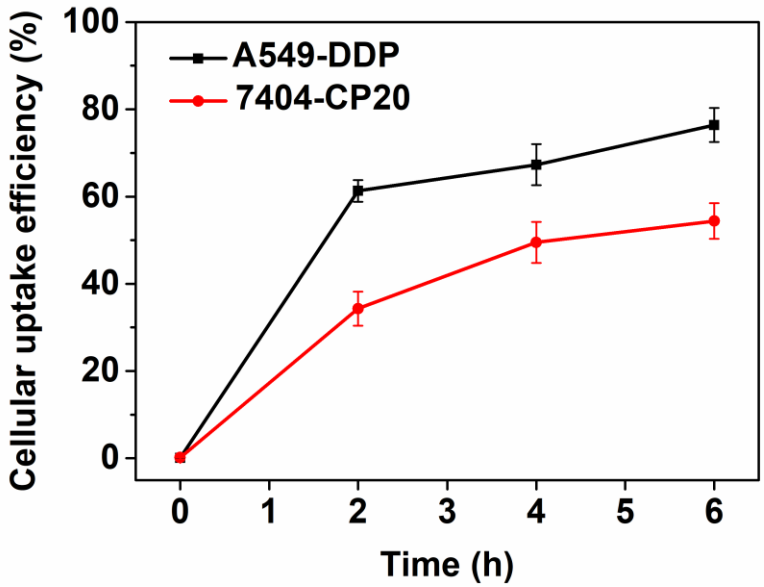

Figure S26. Cellular uptake of PolyPt/Ru nanoparticles by A549-DDP and 7404-CP20 cells determined by flow cytometry.

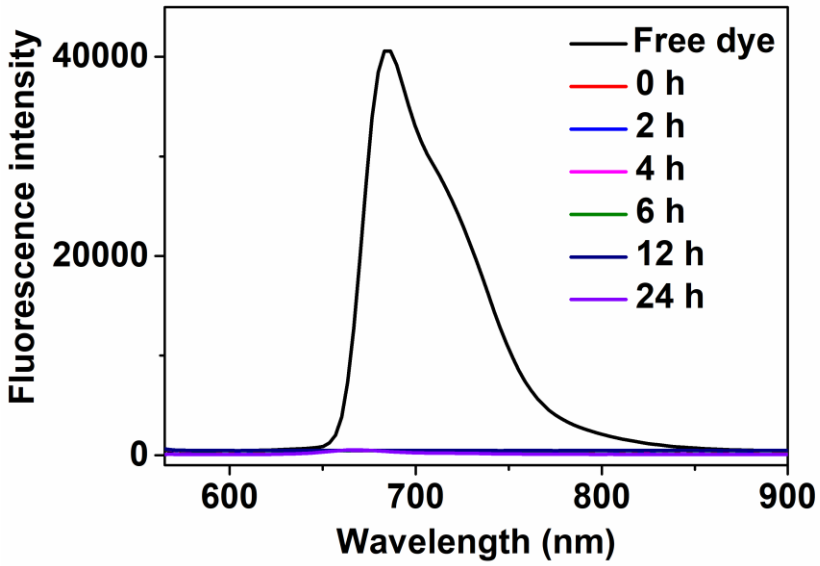

Figure S27. Fluorescence spectrum of the free dye (black line) and fluorescence spectra of dialysate after dialysis of the dye-loaded PolyPt/Ru nanoparticles in the cell culture medium after different time periods. No fluorescence was observed from the dialysate, indicating that there was no leakage of the dye.

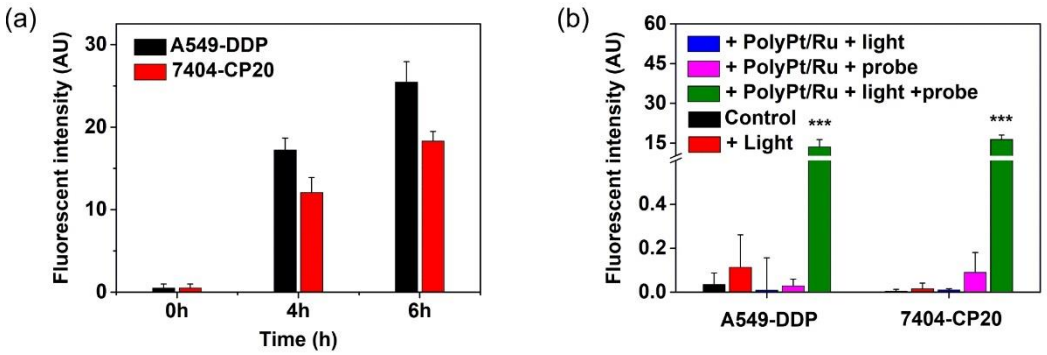

Figure S28. Fluorescence quantitative analyses of (a) cellular uptake and (b) $^1O_2$ generation in Figure 3. The fluorescence intensities were calculated using ImageJ software.

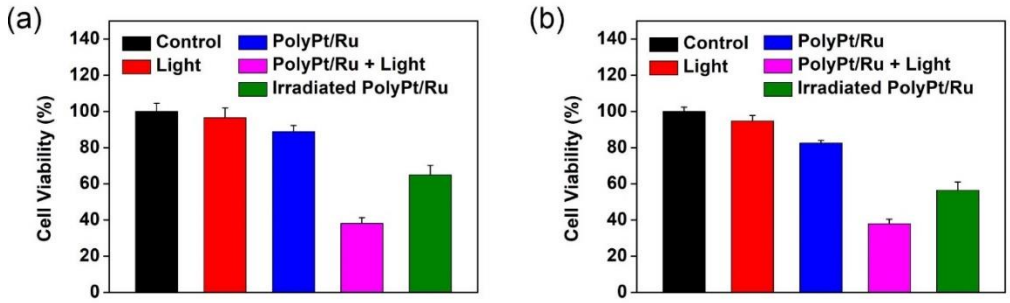

Figure S29. Viability of A549-DDP (a), and 7402-CP20 (b) cells treated under different conditions. These experiments differentiated the contribution of chemotherapy and photodynamic therapy (PDT). The control group exhibited the viability of cells without any treatment. The light group exhibited the viability of cells with 671 nm red light irradiation (125 mW cm^{-2}, 20 min) in the absence of PolyPt/Ru nanoparticles. The PolyPt/Ru nanoparticles group exhibited the viability of cells in the presence of PolyPt/Ru nanoparticles (100 μg/mL) in the dark, which showed the cytotoxicity caused by released cisplatin. The PolyPt/Ru nanoparticles + light group exhibited the viability of cells with 671 nm red light irradiation (125 mW cm^{-2}, 20 min) in the presence of PolyPt/Ru nanoparticles (100 μg/mL), which showed the cytotoxicity

caused by released cisplatin and released $[Ru(biq)_2(H_2O)_2](PF_6)_2$ in combination with generated $^1O_2$.

For the irradiated PolyPt/Ru nanoparticles group, PolyPt/Ru nanoparticles (100 μg/mL) were irradiated (125 mW cm^{-2}, 20 min) in the absence of cells. Light irradiation degraded nanoparticles, released $[Ru(biq)_2(H_2O)_2](PF_6)_2$ and generated $^1O_2$. $^1O_2$ has a short life time and disappeared when light is switched off. Then, PolyPt/Ru nanoparticles after irradiation was incubated with cells for viability test. In this case, this group only showed the effect of chemotherapy without any effect of $^1O_2$.

According to these results, the cytotoxicity caused by released cisplatin to A549-DDP was 12%, caused by released $[Ru(biq)_2(H_2O)_2](PF_6)_2$ to A549-DDP was 23% and caused by PDT to A549-DDP was 27%. Similarly, the cytotoxicity of released cisplatin to 7402-CP20 was 18%, the cytotoxicity of released $[Ru(biq)_2(H_2O)_2](PF_6)_2$ to 7402-CP20 was 26% and the PDT effect was 21%.

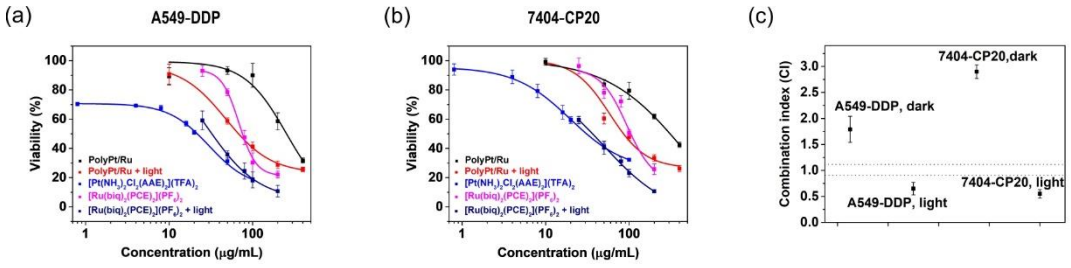

Figure S30. In vitro cytotoxicity of PolyPt/Ru nanoparticles, PolyPt/Ru nanoparticles with red light irradiation (671 nm, 125 mW cm^{-2}, 20 min), $[Pt(NH_3)_2Cl_2(AAE)_2](TFA)_2$, $[Ru(biq)_2(PCE)_2](PF_6)_2$ and $[Ru(biq)_2(PCE)_2](PF_6)_2$ with red light irradiation (671 nm, 125 mW cm^{-2}, 20 min) against (a) cisplatin-resistant A549-DDP and (b) cisplatin-resistant 7404-CP20 cancer cells after 24 h incubation. (c) Combination index (CI) against both A549-DDP and 7404-CP20 cells under different conditions.

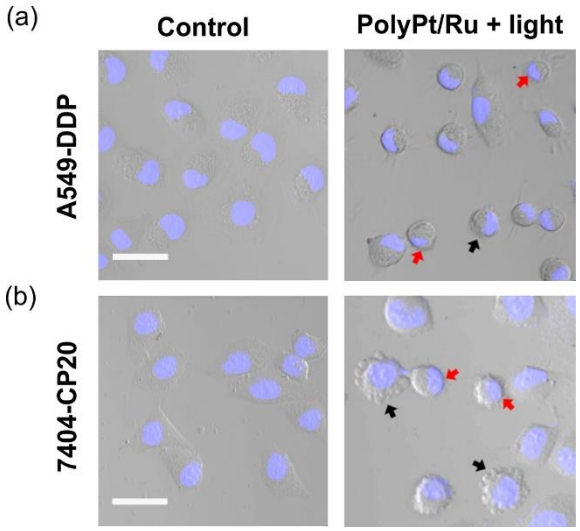

Figure S31. CLSM images of live/dead cells after incubation with PolyPt/Ru nanoparticles, and irradiating with red light. We compared the cell morphology before and after the treatment with PolyPt/Ru + light. In the control groups, A549-DDP and 7404-CP20 cells were uniformly adherent and spindle-shaped. After the cells were incubated with PolyPt/Ru and irradiated with red light, the cells showed inferior adherence, shrunk and changed to round shapes. In addition, nucleus condensation (red arrows) and apoptotic bodies (black arrows) were observed as biomarkers of cell apoptosis. Therefore, these changes indicate that red light irradiation in the presence of PolyPt/Ru caused cytotoxicity in both A549-DDP and 7404-CP20 cells. Scale bars: 50 μm.

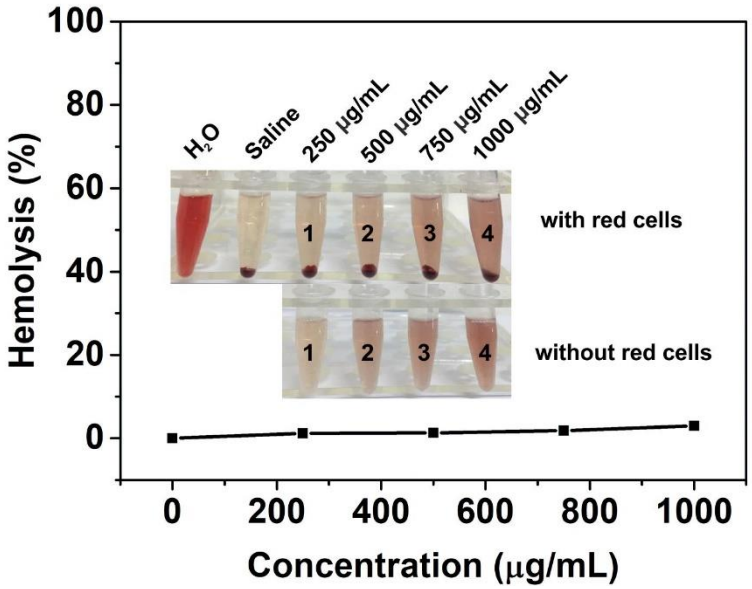

Figure S32. Blood hemolysis treated with PolyPt/Ru nanoparticles at various concentrations from 250 μg/mL to 1000 μg/mL. Water was set as a positive control and saline was set as a negative control. Even after incubation for 24 h, these nanoparticles exhibited non-hemolytic with hemolysis lower than the permissible level of 5%. PolyPt/Ru nanoparticles were compatible with red blood cells.

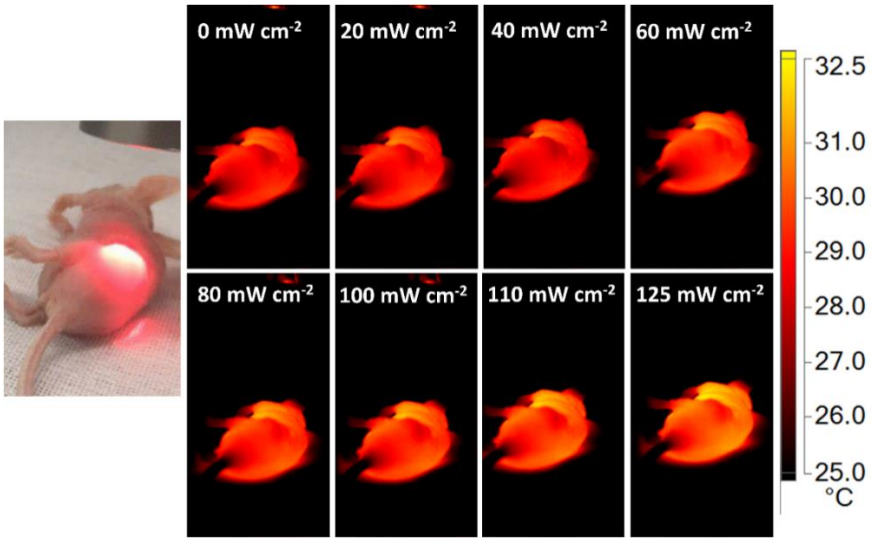

Figure S33. Thermal IR imaging of a tumor-bearing mouse exposed to 671 nm red light irradiation at various dosages. Light irradiation did not cause overheating problem.

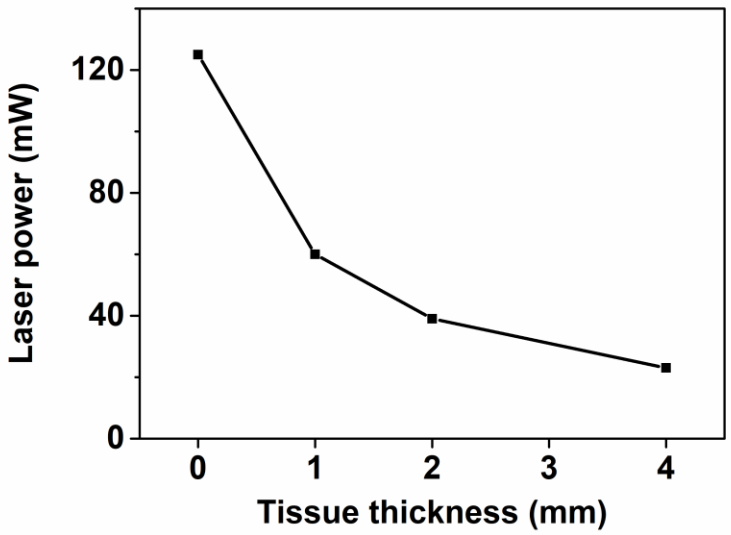

Figure S34. Laser power before and after passing through 1-, 2- and 4-mm-thick tissues. The light intensity after passing through 4-mm-thick tissue was ~20 % of the original intensity (without tissue). Red light with the intensity of 25 mW cm^{-2} was sufficient to efficiently induce drug release. PolyPt/Ru nanoparticles can be activated at such a light intensity.

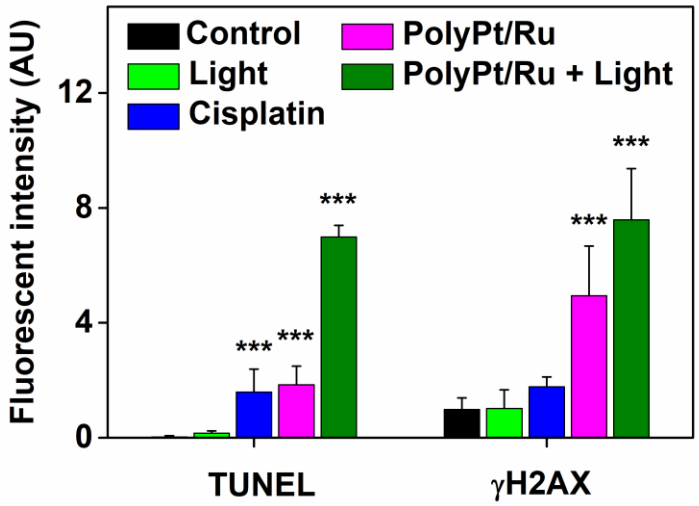

Figure S35. Fluorescence quantitative analyses of TUNEL and γH2AX staining in Figure 4e. The fluorescence intensities were quantified using ImageJ software.

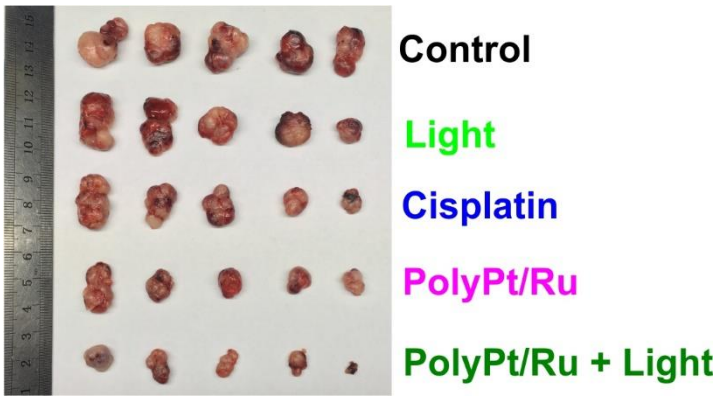

Figure S36. Photo of PDX tumors isolated from the mice on day 7.

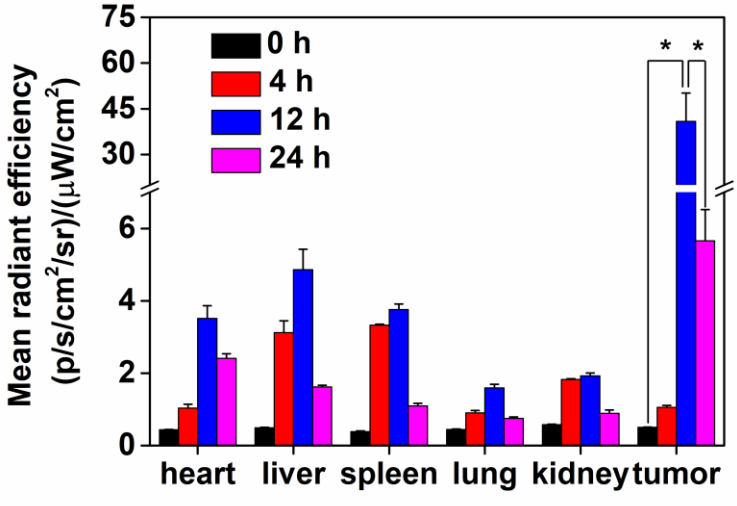

Figure S37. Mean radiant efficiency of different organs and the tumors from mice after injection of dye-loaded PolyPt/Ru nanoparticles for different time periods.

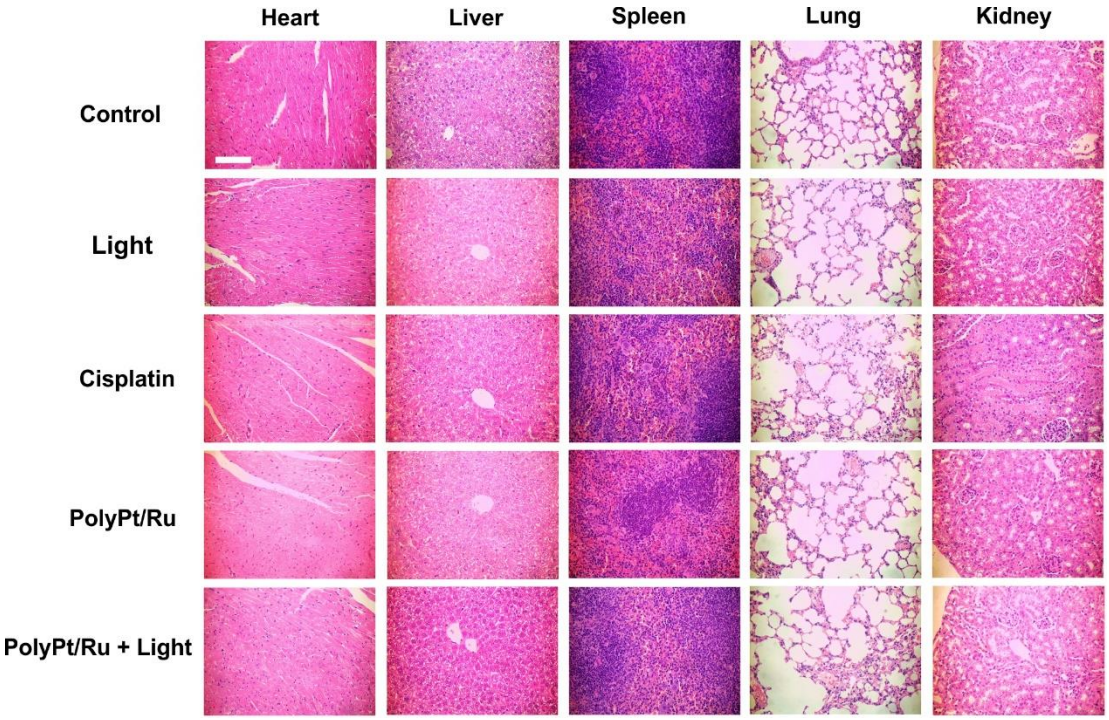

Figure S38. Histopathological analysis by H&E staining of tissue sections isolated from PDX tumor-bearing mice. Scale bar: 100 μm.

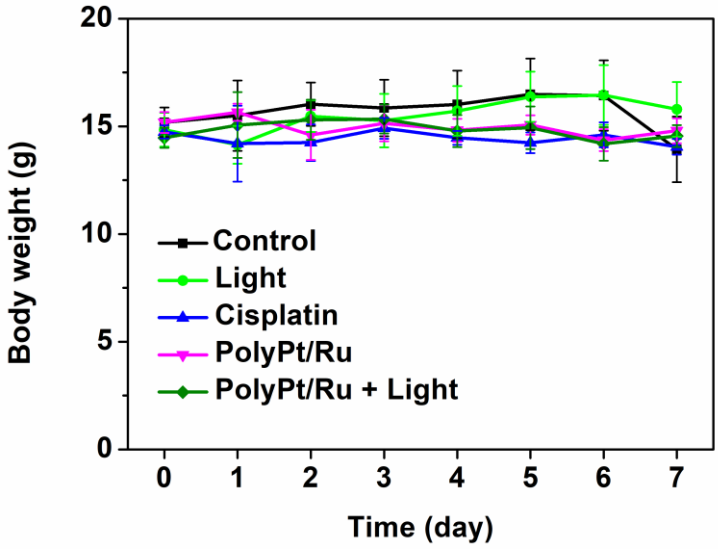

Figure S39. Body weight changes of mice during treatments (n = 5).

Reference

[1] W. Sun, S. Li, B. Häupler, J. Liu, S. Jin, W. Steffen, U. S. Schubert, H.-J. Butt, X.-J. Liang, S. Wu, *Adv. Mater.* **2017**, *29*, 1603702.

[2] X. Chen, R. Hu, C. Qi, X. Fu, J. Wang, B. He, D. Huang, A. Qin, B. Z. Tang, *Macromolecules* **2019**, *52*, 4526.

[3] B. He, H. Su, T. Bai, Y. Wu, S. Li, M. Gao, R. Hu, Z. Zhao, A. Qin, J. Ling, B. Z. Tang, *J. Am. Chem. Soc.* **2017**, *139*, 5437.

[4] O. S. Fenton, J. L. Andresen, M. Paolini, R. Langer, *Angew. Chem., Int. Ed.* **2018**, *130*, 16258.

[5] Z. Ren, S. Sun, R. Sun, G. Cui, L. Hong, B. Rao, A. Li, Z. Yu, Q. Kan, Z. Mao, *Adv. Mater.* **2020**, *32*, 1906024.

[6] R. Zhang, J. Yang, M. Sima, Y. Zhou, J. Kopecek, *Proc. Natl. Acad. Sci. USA* **2014**, *111*, 12181.

[7] M. He, L. Yu, Y. Yang, B. Zou, W. Ma, M. Yu, J. Lu, G. Xiong, Z. Yu, A. Li, *Chin. Chem. Lett.* **2020**, DOI: 10.1016/j.cclet.2020.05.034.

Chapter 4 Summary and Outlook

4.1 Summary

We successfully developed photoresponsive nanocarriers Ru-PEG, based on light-cleavable Ru complexes, and applied them in anticancer therapy. Ru-PEG was demonstrated to have tunable properties by proper design. The adjustable Ru-PEG improved the delivery efficiency of toxic Ru towards cancer cells, to exert their maximum anticancer performance *in vitro* and *in vivo*. The transformable nanocarriers are expected to keep their morphology and related functions in the original stage, and to further transform for achieving improved function to subsequently enhance delivery effectiveness in the following stage. The transformable Ru-PEG nanocarriers provides guidance and concept for developing smart nanocarriers with tunable properties/functionality, representing a promising strategy to enhance the anticancer treatment efficacy.

We also successfully prepared a dual-responsive bimetallic nanocarrier PolyPt/Ru to overcome the drug resistance of tumor. Due to the configuration of the polymer structure and the synergistic effects of the bimetallic moieties, PolyPt/Ru was demonstrated to reverse cisplatin-resistant tumors. We strongly believe that this novel polymer and the approach of combining a Pt complex as chemotherapeutic drug and a Ru complex as photoactivatable prodrugs has great potential for further development. The multi-metallic polymers with multi-responsiveness is a new strategy to treat drug-resistant cancers. Given the abundance of bioactive metal complexes, the design concepts presented here serve as a basis for the development of multi-metallic polymers for biomedical applications.

4.2 Outlook

There are still several open questions and challenges regarding to the Ru-based nanocarriers. First, the activated wavelength of Ru complexes need to be red-shifted. The suitable wavelength for biomedical applications is at the near-infrared (NIR) region. Although Ru complexes can be activated using NIR light via two-photon process or upconverting nanoparticle (UCNP)-assisted photochemistry. Both of them are based on inefficient non-linear optical processes. Direct red-shifting the absorption wavelength of Ru complexes by proper structural design is highly desirable. The use of fluorinated aromatic rings or cyclometalated ligands can be taken into consideration.

Second, the complete anticancer mechanisms of action of Ru complexes need to be further investigated. The intracellular biomolecules have special function, especially DNA and proteins. How Ru complexes interact with these biomolecules and then cause cell death are need to be explored. This helps us understand the structure-activity relationship of Ru complexes, and further select the suitable Ru for selective and effective anticancer therapy.

Third, the long-term biocompatibility of Ru-based nanocarriers need to be improved. Current systems are typically based on synthetic polymers. The building blocks of the polymers and photoproducts from the polymers may cause toxicity. The use of biocompatible natural nanocarriers, such as peptides, or proteins is good alternatives.

Forth, considering the complexity of tumor, more multiple functional nanocarriers should be designed. For example, the combination of Ru complexes with other therapeutic modalities may provide opportunities to combat the complexity of tumor. The combination of Ru-based nanocarriers with bio-imaging agents can achieve the imaging-guiding cancer therapy.

Publications

1. **Xiaolong Zeng**[#], Yufei Wang[#], Jianxiong Han, Wen Sun, Hans-Jürgen Butt, Xing-Jie Liang[*], Si Wu[*]. Fighting against drug-resistant tumors using a dual-responsive Pt(IV)/Ru(II) bimetallic polymer. *Advanced Materials, 2020, 2004766.*

2. **Xiaolong Zeng**, Xuechang Zhou[*], Si Wu[*]. Red and near-infrared light-cleavable polymers. *Macromolecular Rapid Communications, 2018, 39(14): 1800034.*

3. **Xiaolong Zeng**[#], Yufei Wang[#], Yun-Shuai Huang, Jianxiong Han, Wen Sun, Hans-Jürgen Butt, Xing-Jie Liang[*], Si Wu[*]. Red-light-induced simultaneous dePEGylation, morphology transition, and zeta potential increase using amphiphilic metallodrug assemblies: improved tumor penetration and cellular internalization for efficient anticancer phototherapy. *In preparation.*

4. Wen Sun[#], Raweewan Thiramanas[#], Leonardo D. Slep, **Xiaolong Zeng**, Volker Mailänder[*], Si Wu[*]. Photoactivation of anticancer Ru complexes in deep tissue: how deep can we go? *Chemistry–A European Journal, 2017, 23(45): 10832-10837.*

5. Wen Sun, **Xiaolong Zeng**, Si Wu[*]. Photoresponsive ruthenium-containing polymers: potential polymeric metallodrugs for anticancer phototherapy. *Dalton Transactions, 2018, 47(2): 283-286.*

([#] contributed equally)

Acknowledgment

First of all, I would like to thank my supervisor Prof. Dr. Hans-Jürgen Butt for offering me the opportunity as a Ph.D. student in his group. He is really nice, helpful and patient to us. I sincerely appreciate his unwavering support and kind assistance during my PhD period. His encouragement inspire me a lot not only in scientific research but also in my daily life.

Then, I would like to express thank to my project leader Prof. Dr. Si Wu for his constructive guidance. He is always helping me to solve problems. Without his suggestions and discussions, I cannot complete such a challenging research area. He gave me numerous critical suggestions for improving my research to a better level than that I cannot reach by myself.

Additionally, I would also like to thank Prof. Dr. Xing-Jie Liang in the National Center for Nanoscience and Technology, who offered me the chance for biological experiments in his group. With his kind help and fruitful discussions, I benefit a lot on the scientific research and biological field.

In the meantime, I would also like to show my appreciation to Yufei Wang, without her assistance on the biological experiments, I cannot finish these projects. I also want to thank the people I met at National Center for Nanoscience and Technology, Dr. Fangzhou Li, Dr. Ningqiang Gong, Dr. Shuyi Li, Dr. Junge Chen, Dr. Mei Lu, Lu Liu, Yuxuan Zhang, Guangchao Qing, Jingjing Wang, Yongchao Wang and Jie Zhong. I'll always miss the good time we had together.

I would also like to express my sincere gratitude my colleague and friend, Prof. Dr. Wen Sun, for his help on the compound synthesis, and his encouragement and suggestions for my project. I'm grateful to his warm caring for all the time.

Besides, I want to thank Dr. Manfred Wagner for the helpful NMR measurements and discussions, Gunnar Kircher for his help on organic synthesis and discussions, Best Andreas for his help on laser setup, and Beate Müller for HPLC measurement and discussions. I can finish my project with their kindly assistance.

I would also like thank the members of our sub-group, Dr. Philipp Weis, Dr. Chaoming Xie, Annika Kretzschmann, Yannick Nyquist, Jianxiong Han, Jiahui Liu and Yazhi Liu. They have given me a lot of enjoyment over the years. I also want to thank many people I met at Max Planck Institute for Polymer Research, Dr. Xuelin Yao, Dr. Aiting Gao, for their kindly help and discussions.

Finally, I would also like to thank my girlfriend, Dr. Mengyi Li, for her support and giving me courage to pass through the tough moments in my study and life.

Last but not the least, my most sincere thanks go to my parents. They have been supporting and motivating me to be a better man. When I feel depressed, they were always by my side.